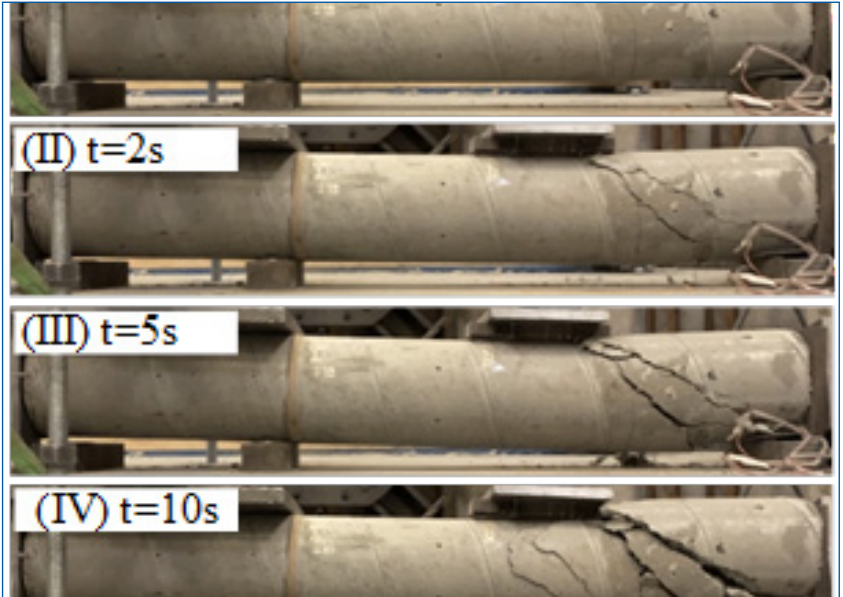


# MOUNTAIN-PLAINS CONSORTIUM

MPC 24-542 | A.D. Sorenson, J. Jiang, and M.Z. Esteghamati

NUMERICAL EVALUATION  
OF PRECAST COLUMNS  
WITH GROUTED SPLICE  
SLEEVE CONNECTORS  
UNDER SEQUENTIAL  
IMPACT AND SEISMIC  
LOADS



A University Transportation Center sponsored by the U.S. Department of Transportation serving the Mountain-Plains Region. Consortium members:

Colorado State University  
North Dakota State University  
South Dakota State University

University of Colorado Denver  
University of Denver  
University of Utah

Utah State University  
University of Wyoming

**Technical Report Documentation Page**

1. Report No. MPC-696		2. Government Accession No.		3. Recipient's Catalog No.	
4. Title and Subtitle  Numerical Evaluation of Precast Columns with Grouted Splice Sleeve Connectors under Sequential Impact and Seismic Loads				5. Report Date August 2024	
				6. Performing Organization Code	
7. Author(s) Andrew D. Sorensen Jinghui Jiang Mohsen Zaker Esteghamati				8. Performing Organization Report No.  MPC 24-542	
9. Performing Organization Name and Address  Utah State University 4110 Old Main Hill Logan, UT 84322-4110				10. Work Unit No. (TRAIS)	
				11. Contract or Grant No.	
12. Sponsoring Agency Name and Address  Mountain-Plains Consortium North Dakota State University PO Box 6050, Fargo, ND 58108				13. Type of Report and Period Covered  Final Report	
				14. Sponsoring Agency Code	
15. Supplementary Notes Supported by a grant from the US DOT, University Transportation Centers Program					
16. Abstract  <p>With the development of accelerated bridge construction (ABC), the seismic performance of typical ABC column-footing connections has been evaluated in high earthquake-prone states like Utah, California, Nevada, and Idaho. But to date, the current literature has yet to fully examine the impact behavior of coupler/rebar connections and the component under vehicle impact using numerical and finite element analysis. There is also a lack of studies on the residual seismic capacity of post-impact columns with GSS connectors. This study involves two major steps. First, the finite element models are validated using experimental data, ensuring accurate representation of the coupler/rebar interface, energy transfer, and material strength degradation. Second, the validated finite element (FE) model undergoes vehicle impact tests to simulate real-world conditions. Following this, the residual seismic capacity of the half-scale column is assessed to understand the impact on structural integrity and seismic resilience of precast columns with GSS connectors.</p> <p>In the validation part, the FE models of test specimens with single couplers effectively capture deformation behaviors, stress distribution, and bond-slip mechanisms, ensuring efficient load transfer. They demonstrated accuracy by predicting peak impact events with minimal error margins (0.7% to 1.65%), confirming their capability to simulate dynamic behaviors. The models accurately predict crack development, failure modes, and non-visible damage within couplers. This approach validates the FE modeling method for further dynamic studies, contributing to more resilient precast concrete structures. Additionally, the FE models of half-scale columns with six couplers showed good agreement with experimental results, capturing initial elastic behavior and bond-slip law. Errors in displacement ductility capacity ranged from 3.7% to 9.8%, and errors in effective yield force ranged from 2.1% to 7.6%, demonstrating high accuracy. The models effectively captured cracking, crushing, and plastic hinge development, validating their use for further studies on seismic performance in precast concrete columns.</p> <p>After validation, the calibrated 3D FE model of a half-scale column was used to assess residual seismic capacity following an impact through sequential impact and quasi-static cyclic loading protocols. The three types of columns displayed distinct crack patterns and failure modes. Precast columns with grouted splice sleeves (GSSs) at the footing-column joint have smaller average displacements than cast-in-place (CIP) columns, demonstrating better impact resistance under high-velocity impacts. Comparing skeleton curves, the columns with the coupler in the column (GSS-C) exhibit the highest residual seismic capacity, followed by the columns with the coupler in the footing (GSS-F), and then CIP columns. CIP columns show extensive spalling and cracking, reducing their bearing capacity and seismic resilience. GSS-C columns maintained structural integrity better due to added reinforcement at the base. GSS-F columns perform better than CIP but are less effective than GSS-C. CIP columns can withstand impacts from vehicles under 0.9 tons at up to 22 mph, while GSS-C and GSS-F columns meet higher impact requirements. This analysis provides critical insights for assessing residual seismic capacity and guiding reinforcement measures to ensure structural integrity and safety.</p> <p>This study provides valuable insights into the behavior of coupler/rebar connections under impact loading, and the residual seismic capacity of post-impact columns, enhancing the understanding and safety of ABC bridges.</p>					
17. Key Word Grouted splice sleeve connectors; Precast pier			18. Distribution Statement Public distribution		
19. Security Classif. (of this report) Unclassified		20. Security Classif. (of this page) Unclassified		21. No. of Pages 103	22. Price n/a

# **Numerical Evaluation of Precast Columns with Grouted Splice Sleeve Connectors under Sequential Impact and Seismic Loads**

Andrew D. Sorensen  
Jinghui Jiang  
Mohsen Zaker Esteghamati

Utah State University  
Logan, Utah

August 2024

## **Acknowledgments**

The authors would like to acknowledge the Mountain-Plains Consortium (MPC)-University Transportation Center sponsored by the U.S. Department of Transportation for providing the research funding to support this study. Additionally, the authors would like to thank Splice Sleeve North America, Inc. for their contribution of the couplers and grout studied in this project. In addition, the authors would also like to acknowledge our research group members: Ashesh Pokhrel, Abdullah (Ony) Al Sarfin, and Zach Benson, who provided valuable assistance in experiments during this project.

## **Disclaimer**

The contents of this report reflect the views of the authors, who are responsible for the facts and the accuracy of the information presented. This document is disseminated under the sponsorship of the Department of Transportation, University Transportation Centers Program, in the interest of information exchange. The U.S. Government assumes no liability for the contents or use thereof.

North Dakota State University does not discriminate in its programs and activities on the basis of age, color, gender expression/identity, genetic information, marital status, national origin, participation in lawful off-campus activity, physical or mental disability, pregnancy, public assistance status, race, religion, sex, sexual orientation, spousal relationship to current employee, or veteran status, as applicable. Direct inquiries to Vice Provost, Title IX/ADA Coordinator, Old Main 100, (701) 231-7708, [ndsueoaa@ndsu.edu](mailto:ndsueoaa@ndsu.edu).



## ABSTRACT

With the development of accelerated bridge construction (ABC), the seismic performance of typical ABC column-footing connections has been evaluated in high earthquake-prone states, like Utah, California, Nevada, and Idaho. But to date, the current literature has yet to fully examine the impact behavior of coupler/rebar connections and the component under-vehicle impact using numerical and finite element analysis. There is also a lack of studies on the residual seismic capacity of post-impact columns with GSS connectors. This study involves two major steps. First, the finite element models are validated using experimental data, ensuring accurate representation of the coupler/rebar interface, energy transfer, and material strength degradation. Second, the validated finite element (FE) model undergoes vehicle impact tests to simulate real-world conditions. Following this, the residual seismic capacity of the half-scale column is assessed to understand the impact on structural integrity and seismic resilience of precast columns with GSS connectors.

In the validation part, the FE models of test specimens with single couplers effectively capture deformation behaviors, stress distribution, and bond-slip mechanisms, ensuring efficient load transfer. They demonstrated accuracy by predicting peak impact events with minimal error margins (0.7% to 1.65%), confirming their capability to simulate dynamic behaviors. The models accurately predict crack development, failure modes, and non-visible damage within couplers. This approach validates the FE modeling method for further dynamic studies, contributing to more resilient precast concrete structures. Additionally, the FE models of half-scale columns with six couplers showed good agreement with experimental results, capturing initial elastic behavior and bond-slip law. Errors in displacement ductility capacity ranged from 3.7% to 9.8%, and errors in effective yield force ranged from 2.1% to 7.6%, demonstrating high accuracy. The models effectively captured cracking, crushing, and plastic hinge development, validating their use for further studies on seismic performance in precast concrete columns.

After validation, the calibrated 3D FE model of a half-scale column was used to assess residual seismic capacity following an impact through sequential impact and quasi-static cyclic loading protocols. The three types of columns displayed distinct crack patterns and failure modes. Precast columns with grouted splice sleeves (GSSs) at the footing-column joint have smaller average displacements than cast-in-place (CIP) columns, demonstrating better impact resistance under high-velocity impacts. Comparing skeleton curves, the columns with the coupler in the column (GSS-C) exhibited the highest residual seismic capacity, followed by the columns with the coupler in the footing (GSS-F), and then CIP columns. CIP columns showed extensive spalling and cracking, reducing their bearing capacity and seismic resilience. GSS-C columns maintained structural integrity better due to added reinforcement at the base. GSS-F columns performed better than CIP but were less effective than GSS-C. CIP columns can withstand impacts from vehicles under 0.9 tons at up to 22 mph, while GSS-C and GSS-F columns meet higher impact requirements. This analysis provides critical insights for assessing residual seismic capacity and guiding reinforcement measures to ensure structural integrity and safety.

This study provides valuable insights into the behavior of coupler/rebar connections under impact loading, and the residual seismic capacity of post-impact columns, enhancing the understanding and safety of ABC bridges.

# TABLE OF CONTENTS

<b>1. INTRODUCTION.....</b>	<b>1</b>
1.1 Background.....	1
1.2 Problem Statement and Scope.....	2
1.3 Research Objectives.....	2
1.4 Study Organization .....	3
<b>2. LITERATURE REVIEW.....</b>	<b>4</b>
2.1 Pull-out Models.....	4
2.1.1 Grout Model.....	4
2.1.2 Bond-slip Model .....	7
2.1.3 Gaps in Current Pull-out Models .....	10
2.2 Push-over Models .....	10
2.2.1 Fiber Section (2D) Modelling.....	10
2.2.2 Solid Element (3D) Modelling.....	14
2.2.3 Gaps in Current Push-over Models.....	17
2.3 Impact Models .....	18
2.3.1 Vehicle Impact.....	18
2.3.2 Structure Models.....	20
2.3.3 Gaps in Current Impact Models.....	23
2.4 Summary.....	24
<b>3. FE MODELS OF TEST SPECIMENS .....</b>	<b>25</b>
3.1 Geometry Information.....	25
3.2 Contact and Boundary Conditions .....	26
3.3 Loading Procedures .....	27
3.4 Bond-slip Law.....	28
3.5 Material Properties.....	32
3.5.1 Material Model for Concrete and Grout .....	32
3.5.2 Material Model Rebar.....	36
3.5.3 Material Model for Accessory Steels.....	37
3.6 Mesh Sensitivity Study .....	37
3.7 Verification of Simulated Results .....	38
3.7.1 Strain Response During the Static Test .....	38
3.7.2 Dynamic Response During the Impact Test .....	40

3.7.3	Failure Processes During the Impact Test .....	41
3.8	Summary .....	44
<b>4.</b>	<b>FE MODELS OF HALF-SCALE COLUMN UNDER SEISMIC LOAD .....</b>	<b>45</b>
4.1	Geometry Information of Half-scale Columns .....	45
4.2	Modeling Techniques of Half-scale Columns.....	48
4.2.1	General Description of FE Models .....	48
4.2.2	Contact and Boundary Conditions .....	53
4.2.3	Loading Procedures .....	54
4.3	Verification of Simulated Results .....	55
4.3.1	Strain Response During Initial Stage.....	56
4.3.2	Seismic Response During Pushover Stage .....	57
4.4	Summary .....	67
<b>5.</b>	<b>FINITE ELEMENT ANALYSIS OF HALF-SCALE COLUMN UNDER SEQUENTIAL IMPACT AND SEISMIC LOADS .....</b>	<b>68</b>
5.1	General Description of FE Models .....	68
5.2	Loading Procedures .....	70
5.3	Dynamic Response During Impact .....	71
5.4	Residual Seismic Capacity Assessment of Post-impact Stage.....	80
5.5	Summary .....	85
<b>6.</b>	<b>CONCLUSIONS .....</b>	<b>87</b>

**LIST OF TABLES**

Table 2.1 Numerical studies on FE models of pull-out tests..... 7  
Table 2.2 Numerical studies on FE models of push-over tests..... 17  
Table 2.3 Categorization of impact vehicle..... 19  
Table 2.4 Categorization of impact velocity ..... 19  
Table 2.5 Numerical studies on FE models of impact tests..... 23  
Table 3.1 Contact setting key parameters in LS-DYNA ..... 27  
Table 3.2 Bond-slip setting parameters in LS-DYNA ..... 29  
Table 4.1 Material parameters in FE models..... 52  
Table 4.2 Contact setting key parameters in LS-DYNA ..... 54  
Table 4.3 Comparisons of key characteristics from skeleton curves..... 60  
Table 5.1 List of collision cases ..... 69  
Table 5.2 Comparisons of displacement ductility capacity from skeleton curves..... 84

## LIST OF FIGURES

Figure 2.1	Grout section views of various studies.....	5
Figure 2.2	Coulomb friction curve in ABAQUS [9] .....	6
Figure 2.3	Bond stress-versus-slip law.....	8
Figure 2.4	OpenSees model details [25].....	11
Figure 2.5	Stress-strain model for couplers [25] .....	11
Figure 2.6	Analytical model of precast column with GSSs [4].....	12
Figure 2.7	Proposed element's models [4] .....	12
Figure 2.8	Schematic of bond-slip rotation [3].....	13
Figure 2.9	FE models or result in previous studies .....	16
Figure 2.10	Schematic diagram of grout sleeve .....	20
Figure 2.11	FE models in previous studies.....	22
Figure 3.1	Geometry information of FE model.....	26
Figure 3.2	Boundary conditions .....	26
Figure 3.3	Loading stage description .....	28
Figure 3.4	Bond stress-slip laws for monotonic loading proposed by Murcia-Delso et al. [49]. .....	29
Figure 3.5	Input cards for bond-slip between rebar and concrete (force vs. slip) (units: mm-kg-ms-GPa) .....	30
Figure 3.6	Input cards for bond-slip between rebar and grout (force vs. slip) (units: mm-kg-ms-GPa) .....	31
Figure 3.7	Input cards for neglecting slip model between rebar and concrete .....	31
Figure 3.8	Comparison of the impact response with or without considering bond-slip of concrete-rebar.....	32
Figure 3.9	Input cards for *MAT_CSCM_CONCRETE (units: mm-kg-ms-GPa).....	34
Figure 3.10	Default and update parameters for *MAT_CSCM (units: mm-kg-ms-GPa).....	35
Figure 3.11	Calibration study of CSCM Material .....	36
Figure 3.12	Input cards for *MAT_PLASTIC_KINEMATIC (units: mm-kg-ms-GPa).....	36
Figure 3.13	Input cards for *MAT_RIGID (units: mm-kg-ms-GPa).....	37
Figure 3.14	Mesh sensitivity analysis.....	37
Figure 3.15	Compressive strain- time history (solid lines: test data; short dash lines: FE results) .....	39
Figure 3.16	Strain- time history (solid lines: test data; short dash lines: FE results) .....	39
Figure 3.17	Error of maximum strain between the experiments and FE models .....	40
Figure 3.18	Comparison of impact force-time .....	41
Figure 3.19	Comparison of failure processes .....	43
Figure 3.20	Section views at the end of impacting (Left: Grout and rebars; Right: Grout damage).....	44
Figure 4.1	General joint design details of column-footing (unit: inch).....	46
Figure 4.2	Geometry information of columns (unit: inch) .....	48
Figure 4.3	Description of FE models (unit: inch).....	51
Figure 4.4	Boundary conditions .....	53
Figure 4.5	Loading stage description .....	55
Figure 4.6	Strain-time history (solid lines: FE results in Section 3.7.1; dash lines: FE results from half-scale columns).....	56
Figure 4.7	Hysteresis response .....	58

Figure 4.8	Average skeleton curves .....	59
Figure 4.9	Damage developments .....	63
Figure 4.10	Comparison of CIP's damage states .....	64
Figure 4.11	Comparison of GSS-C's damage states .....	65
Figure 4.12	Comparison of GSS-F's damage states .....	66
Figure 5.1	Description of FE models (unit: inch).....	69
Figure 5.2	Loading stage description .....	71
Figure 5.3	Failure modes of CIP .....	74
Figure 5.4	Failure modes of GSS-C .....	76
Figure 5.5	Failure modes of GSS-F .....	78
Figure 5.6	Displacement responses of columns .....	80
Figure 5.7	Damage development progressions of columns.....	82
Figure 5.8	Skeleton curves .....	83
Figure 5.9	Relationship of impact velocity and mass with code requirements .....	84

## EXECUTIVE SUMMARY

The two main objectives of this study are: 1) to develop and validate two finite element models — one for small-scale specimens with single couplers and another for half-scale columns. The small-scale model is validated against experimental results under lateral static and dynamic conditions, while the half-scale model is compared with experimental results under seismic loads. This involves calibrating material properties, mesh size sensitivity, and bond-slip laws to ensure accurate validation. 2) Assess the impact performance and residual seismic capacity of the calibrated half-scale columns following an impact event, using sequential impact and quasi-static cyclic loading protocols. This provides insight into the structural integrity and resilience of precast concrete columns with grouted splice sleeves (GSSs) under extreme loading conditions.

To achieve the first objective, 3D models matching the dimensions of small-scale experimental specimens were created. These models were calibrated for material properties, mesh size sensitivity, and bond-slip laws to ensure accuracy. The validated models were compared with experimental results under static and dynamic conditions, demonstrating their feasibility in predicting strain responses during static tests and simulating dynamic behavior and damage states under impact loading. Additionally, 3D finite element (FE) models of half-scale columns are developed and validated against experimental data from Pantelides et al. [2], using strain-time history curves, hysteresis curves, average skeleton curves, and crack development analysis. The validation showed strong agreement between the FE analysis and experimental results in both initial and pushover stages, confirming the models' accuracy and reliability in capturing the seismic behavior of precast columns.

The second objective of this study explored the residual seismic capacity of precast columns following an impact accident. Using a calibrated 3D FE model, the column was subjected to a sequential loading protocol: first, an impact load simulated sudden damage, followed by a quasi-static cyclic loading protocol to evaluate seismic residual capacity. Post-impact damage distributions were compared among three column categories, and displacement curves at various heights were analyzed to investigate structural responses under different impact velocities. During the quasi-static cyclic loading phase, damage patterns at drift ratios of 1%, 2%, and failure were observed, providing insights into damage progression. Skeleton curves derived from FE results explored the impact on seismic capacity reduction, and displacement ductility capacity was calculated. Finally, the relationship between impact velocity and vehicle mass with respect to code requirements was plotted to determine the residual seismic capacity of the columns after an impact accident. These figures guided the assessment and necessary reinforcement measures to ensure structural integrity and safety in future seismic events.

This analysis provides valuable insights into the behavior of coupler/rebar connections under impact loading and the residual seismic capacity of post-impact columns, enhancing the understanding and safety of ABC bridges. By determining the failure modes of grouted coupler connections in ABC structures, the study offers critical references for assessing the residual seismic capacity of columns after impact accidents and guides necessary reinforcement measures to ensure structural integrity in future seismic events. This project directly aligns with the USDOT strategic goal of safety, equipping designers with better information for designing resilient structures. As a result, bridges constructed using ABC techniques will be more capable of withstanding unexpected impacts, thereby enhancing their safety and reliability for public use.

# 1. INTRODUCTION

## 1.1 Background

Grouted coupler connections are a common connection type used in Accelerated Bridge Construction (ABC). ABC is a bridge construction method that incorporates innovative techniques, methodologies, and materials to efficiently reduce construction time, traffic disruption, and enhance dynamic performance. According to the Florida International University ABC Project Database, Utah currently has eight bridges in service constructed using ABC techniques [1]. The seismic performance of typical ABC column-footing connections has been evaluated in high earthquake-prone states like Utah, California, Nevada, and Idaho [2][3][4]. However, beyond the dynamic loads caused by earthquakes, it is also critical to investigate the deformation and failure behavior of these connections under other dynamic loadings, such as blasts and vehicular impacts. These types of dynamic loads can impose different stresses and strains on the connections, which may affect their structural integrity and safety. Understanding the behavior of grouted coupler connections under these conditions is essential for ensuring the robustness and resilience of bridges constructed using ABC methods.

A current research project at Utah State University is studying the behavior of the Utah Department of Transportation's (UDOT) current ABC grouted coupler connections, as detailed in the UDOT Structures Design & Detailing Manual, under vehicular impact loading. Preliminary results from this study have shown significant variances in failure modes of these connections, influenced by differences in vehicle weight, and impact velocity. Conducting extensive experimental work on all possible combinations is prohibitively expensive. Therefore, validated finite element models based on experimental results can be developed to efficiently evaluate these variations in input characteristics, such as loading conditions, at a significantly lower cost. This analysis helps determine whether the coupler connection performs better when placed in the pier or the footing under impact loading and assess whether the post-impact columns meet current code seismic requirements. This research aims to provide insights into the impact behavior of grouted coupler connections, ensuring the robustness and resilience of bridges using ABC methods against vehicular impacts and sequential impact and seismic loads.

Additionally, the current literature has yet to fully examine the coupler/rebar connections and the component impact behavior using numerical and finite element analysis. There is also a lack of studies on the residual seismic capacity of post-impact columns with grouted splice sleeve (GSS) connectors. This topic is particularly challenging because the connection involves four different materials: Portland cement concrete, reinforcing steel, cast iron coupler, and low shrinkage grout. Meanwhile, ensuring the integrity of the grout within the post-impact coupler is difficult, as grout failure inside the coupler is often undetectable. This uncertainty makes it challenging to ensure the connection efficiency of the footing-column even after lightweight vehicle impact. As a result, the entire structure may be at risk of collapse when faced with future seismic events. Understanding and addressing these issues is critical to improving the resilience and safety of structures using grouted splice sleeves.

This study develops a sophisticated finite element (FE) model that accurately represents the coupler/rebar interface, energy transfer from the impacted column location through the coupler into the foundation, and material strength degradation. The model is validated using existing experimental data collected from precast concrete column single coupler testing at the USU SMASH Lab and the half-scale precast column testing with six GSSs reported by Pantelides et al. [2]. By incorporating these data, the model ensures a high degree of accuracy in simulating real-world conditions. The study carried out vehicle impact simulations on the calibrated FE model, followed by an assessment of the residual seismic capacity of a half-scale column, to determine the impact effect on the reduction of seismic capacity of columns. This analysis provides valuable insights into the behavior of coupler/rebar connections under impact loading,



and the residual seismic capacity of post-impact columns, enhancing the understanding and safety of ABC bridges.

## 1.2 Problem Statement and Scope

Bridge systems are often exposed to multiple extreme events, such as vehicle collisions and seismic activity. For example, a precast pier connected by GSSs might not show visible damage after a collision, but microcracks could form within the sleeve, reducing the coupler's connection capacity. This compromised integrity could diminish the bridge's ability to withstand future seismic hazards, especially in high-seismic zones, increasing vulnerability to subsequent extreme events and posing significant risks to structural safety. Hence, it is necessary to understand the failure mechanisms of GSSs and the energy transfer within the coupler system under different vehicle impact scenarios. Assessing the residual seismic capacity of a calibrated 3D FE model of a half-scale column following an impact event involves analyzing damage progression, skeleton curves, and reduced displacement ductility capacity. This analysis forms the foundational knowledge for ensuring effective bonding of the coupler system and protecting the safety of precast piers against sequential hazards. However, to date, no study directly addresses this critical issue.

This research addressed significant gaps in the literature by providing numerical data and analysis of the impact behaviors of precast columns with GSS connectors. It investigated the reduced seismic capacity of columns due to impact events, comparing them with undamaged, or "healthy," columns. Additionally, this study offers insights into the methodologies for evaluating precast columns with GSS connectors under impact and analyzing the residual seismic strength of post-impact GSS connectors.

The specific research questions of this research are:

- 1) How can a finite element model for a single coupler connection be developed and validated using experimental data to accurately represent the four materials and determine an accurate load distribution model for static and dynamic loads?
- 2) How can the FE models be validated against experimental results, specifically in terms of strain-time history curves, hysteresis curves, and crack development?
- 3) How do lightweight vehicle impacts affect damage distributions and displacement curves in a calibrated FE model of a half-scale column across different column categories and impact velocities?
- 4) How can the residual seismic capacity of a half-scale column be evaluated after an impact using a calibrated FE model, focusing on damage progression and reduced displacement ductility under sequential impact and seismic loading?

## 1.3 Research Objectives

To answer the questions in the previous section, the objectives of this study were to:

- 1) Develop and validate a finite element model for a single coupler connection using experimental data, accurately representing the four materials, to determine an accurate load distribution model for static load and impact resistance for dynamic load.
- 2) Create and validate FE models of half-scale columns under seismic loads, ensuring accurate simulation of experimental results.
- 3) Apply lightweight vehicle impacts on a calibrated FE model of a half-scale column, compare damage distributions among three column categories, and analyze displacement curves at various heights to investigate the structural impact response under different impact velocities.

- 4) Evaluate the residual seismic capacity of a calibrated FE model of a half-scale column after impact, analyzing damage progression and reduced displacement ductility under sequential impact and seismic loading.

Finally, the relationship between impact velocity and vehicle mass with respect to code requirements was plotted to determine residual seismic capacity of the columns after an impact accident. These figures guided the assessment and necessary reinforcement measures to ensure structural integrity and safety in future seismic events.

This project directly relates to the USDOT strategic goal of safety. By determining the failure modes of grouted coupler connections in ABC structures, designers will have better information when designing these types of connections. This will make the structures more resilient to seismic load after impact loading events, thus enhancing their safety and reliability. Understanding these dynamics ensures bridges constructed using ABC techniques can withstand unexpected impacts and remain safe for public use.

## **1.4 Study Organization**

This report is divided into six chapters. Chapter 1 provides the general background, problem statement, scope, and objectives of the research study. Chapter 2 reviews existing information on the finite element modeling of grouted coupler connections. Chapter 3 details the development of finite element models for singular coupler connections, focusing on the four materials involved: Portland cement concrete, reinforcing steel, cast iron coupler, and low shrinkage grout. Validation from previously conducted experimental tests is included. Chapter 4 develops FE models of three half-scale columns under seismic loads, simulating experiments by Pantelides et al. [2]. Validation is achieved using strain-time history curves, hysteresis curves, average skeleton curves, and analysis of crack development and damage states. Chapter 5 assesses the residual seismic capacity of a calibrated 3D FE model of a half-scale column following an impact, using a sequential loading protocol. The study analyzed damage progression, skeleton curves, and displacement ductility capacity. Chapter 6 presents the conclusions of the study. A bibliography of cited works is included at the end.

## 2. LITERATURE REVIEW

Based on the findings from the previous literature review, current experimental research on grout splice sleeve (GSS) connectors primarily employ three testing methods: pull-out tests for measuring static tensile strength, push-over tests for assessing seismic performance, and pendulum or drop hammer impact tests for evaluating resistance to dynamic impacts. This section aims to gather the numerical studies of these testing methods, including pull-out tests, push-over tests, and impact tests. The objective was to identify gaps in the current research and enhance the fundamental understanding of modeling GSS connectors. Ultimately, this review assessed the unresolved challenges in both static and dynamic modeling domains.

### 2.1 Pull-out Models

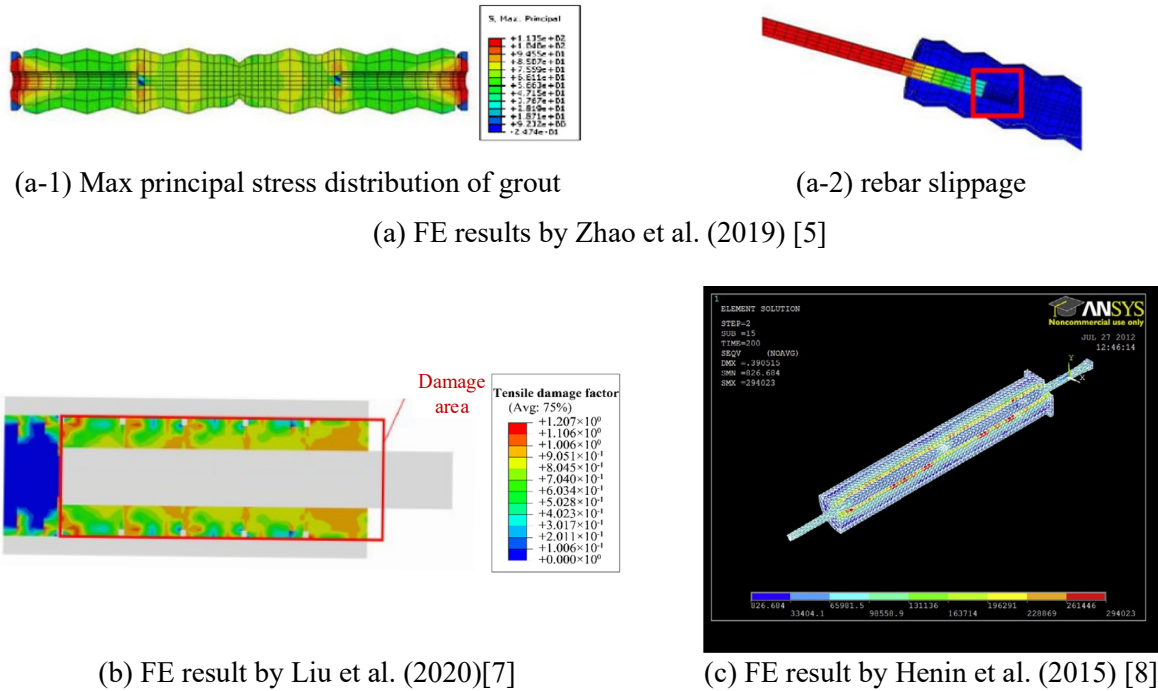
Finite Element (FE) models for pull-out tests on GSS connections are relatively straightforward, requiring consideration of only three components: the coupler, rebar, and grout. These models are essential for exploring the material behavior of grout in coupler and the bond-slip relationship between the grout and rebar. Such investigations are crucial for accurately representing the mechanical interaction of the FE simulations.

#### 2.1.1 Grout Model

Zhao et al. simulated grout using a concrete material model, where the stress-strain relationship was modeled with a multi-linear isotropic hardening material. The stress-strain ( $\sigma$ - $\varepsilon$ ) curve for grout is described by Eq. 2.1 [5].

$$\sigma = \frac{E_g \varepsilon}{1 + \left(\frac{\varepsilon}{\varepsilon_0}\right)^2} \quad \text{Eq. 2.1}$$
$$\varepsilon_0 = \frac{2f_g}{E_g}$$

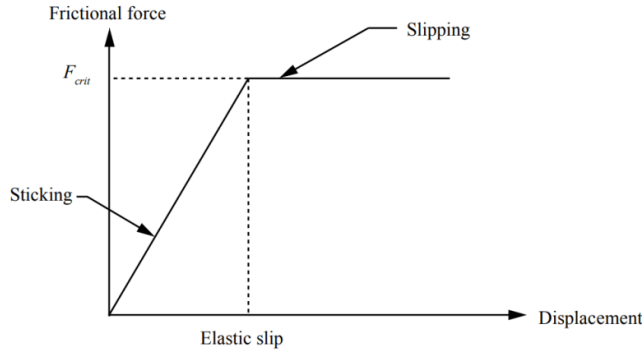
where,  $\varepsilon_0$  is the strain corresponding to the ultimate compressive strength of the grout  $f_g$ . Grout failure criterion follows the five-parameter failure criteria proposed by William-Warnke [6]. Maximum principal stress distribution of the grout is shown in Figure 2.1 (a-1). It indicates that the grout failure initiates at the sleeve ends.



**Figure 2.1** Grout section views of various studies

Zhao et al. utilized brick elements in ABAQUS to model the coupler, grout, and rebar, applying surface-to-surface contact interactions to simulate slippage between the spliced rebar and grout under tensile loads, while the connection between the sleeve and grout was represented as a tie interaction. Rebar slip failure was evident in the numerical results, as shown in Figure 2.1 (a-2).

Liu et al. employed the Concrete Damage Plasticity (CDP) model to simulate the behavior of grout, capturing its stress-strain response characterized by initial linear elasticity, followed by hardening, and softening after reaching the ultimate stress [7]. The tensile damage distribution of the grout, illustrated in Figure 2.1 (b), indicated that damage primarily occurred at the sleeve ends. Liu et al. modeled the coupler, grout, and rebar using brick elements in ABAQUS, with a tie constraint between the sleeve and the grout. For the interaction between the rebar and grout, they implemented a surface-to-surface contact based on Coulomb friction in the tangential direction. The typical Coulomb friction curve, shown in Figure 2.2, illustrates the relationship between the tangential force (frictional force) and the relative motion (slip rate) of the two contact surfaces. Their results showed no significant slipping failure, and the numerical model provides an accurate prediction of the load-displacement response during axial tension, closely matching experimental observations.



**Figure 2.2** Coulomb friction curve in ABAQUS [9]

Henin et al. modeled the grout using the cracking and crushing of brittle materials, while the steel sleeve and bars were modeled using ductile materials; with all being SOLID elements in ANSYS. The interfaces between them were modeled by contact elements with coefficients of friction. The stress distribution in the coupler is shown in Figure 2.1(c) [8].

Kuang et al. developed a mortar constitutive model for grout in GSS, which includes both the ascending and descending stages of the stress-strain relationship. The stress-strain ( $\sigma$ - $\varepsilon$ ) curve for grout is described by Eq. 2.2 [10]:

$$\sigma = \frac{\varepsilon \varepsilon_0 f_c}{0.85 \varepsilon^2 - 0.7 \varepsilon \varepsilon_0 + 0.85 \varepsilon_0^2} \quad \text{Eq. 2.2}$$

$$\sigma = \left( 1.1 - 0.1 \frac{\varepsilon}{\varepsilon_0} \right) f_c$$

where,  $f_c$  represents the peak stress of grout, and  $\varepsilon_0$  is the corresponding strain. They found this relationship fits well with the experimental test curve, making it a reliable model for describing the compressive behavior of grout material.

Zheng et al. utilized the ANSYS program to model the grout, steel bars, and sleeves, all employing SOLID elements. The grout was simulated to capture the cracking and crushing behavior typical of brittle materials, while the steel bars and sleeves were modeled to represent ductile materials. Interfaces between the spliced bars and grout were modeled using TARGE170 elements, and the contact between the sleeve and grout was simulated using CONTA174 elements [11].

Kahama et al. modeled the GSS system using brick elements in ABAQUS. The Concrete Damage Plasticity (CDP) model was applied to the grout to capture its nonlinear behavior. Perfect bonding (tied contact) was assumed between the grout and the sleeve. Additionally, a Coulomb friction contact was defined between the grout and the rebars [12].

The critical information about grout modeling and contact types between grout and rebar from various studies is summarized in Table 2.1. It indicates that in widely used finite element software, available concrete models can be effectively utilized for simulating grout. Surface-to-surface contact interactions are commonly employed to simulate slippage between rebar and grout.

**Table 2.1** Numerical studies on FE models of pull-out tests

Reference	Software	Grout model	Grout element	Rebar element	Contact between Grout and Rebar
Zhao et al. (2019) [5]	ABAQUS	Multi-linear isotropic hardening material	SOLID	SOLID	Surface-to-surface contact
Liu et al. (2020) [7]	ABAQUS	Concrete Damage Plasticity (CDP) model	SOLID	SOLID	Surface-to-surface contact
Henin et al. (2015) [8]	ANSYS	Brittle materials with cracking and crushing	SOLID	SOLID	Contact elements with coefficients of friction
Kuang et al. (2018) [5]	ABAQUS	Mortar constitutive model	SOLID	SOLID	-
Zheng et al. (2023) [6]	ANSYS	Brittle materials with cracking and crushing	SOLID	SOLID	TARGE170 elements
Kahama et al. (2018) [12]	ABAQUS	Concrete Damage Plasticity (CDP) model	SOLID	SOLID	Surface-to-surface contact

However, review of these studies results in two main concerns: (1) Full-scale structural simulations using solid elements for all rebars can be highly resource-intensive and time-consuming. Therefore, beam elements are often used as a more efficient alternative. (2) The Coulomb friction law does not accurately capture the real bond-slip behavior. This law oversimplifies the interaction by assuming a linear relationship between displacement and bond force during the initial elastic slippage stage and maintaining a constant bond force after reaching the maximum force, regardless of further displacement. In reality, the bond-slip relationship between rebar and concrete typically shows an initial rise in bond force with displacement, reaching a peak, and subsequently declining as displacement continues to increase. Further research is necessary to understand and accurately model the bond-slip relationship between the rebar and its surrounding materials.

## 2.1.2 Bond-slip Model

### 2.1.2.1 Quasi-static Bond Behavior

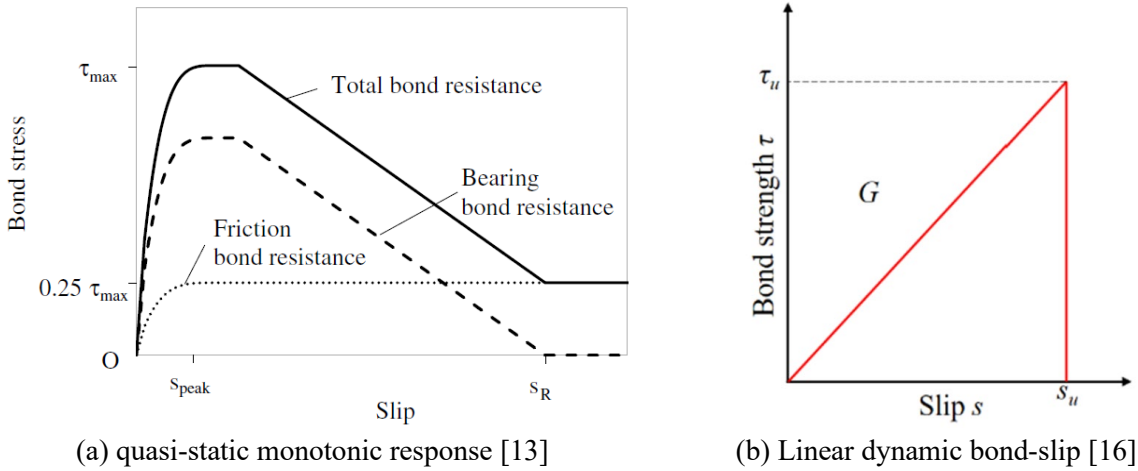
Murcia-Delso et al. proposed a novel interface model to simulate the bond-slip behavior of reinforcing bars in well-confined concrete, which is validated in ABAQUS using pull-out tests [13]. The bond stress ( $\tau$ ) is described using a set of five polynomial functions related to slip ( $s$ ), shown as Eq. 2.3~ 2.4 [13], [14], [15].

$$\tau(s) = \begin{cases} 4.0 \frac{\tau_{max}}{s_{peak}} s & s < 0.1s_{peak} \\ \tau_{max} \left[ 1 - 0.6 \left( \frac{s - s_{peak}}{0.9s_{peak}} \right)^4 \right] & 0.1s_{peak} \leq s < s_{peak} \\ \tau_{max} & s_{peak} \leq s < 1.1s_{peak} \\ \tau_{max} \left[ 1 - 0.75 \frac{s - 1.1s_{peak}}{s_R - 1.1s_{peak}} \right] & 1.1s_{peak} \leq s < s_R \\ 0.25\tau_{max} & s \geq s_R \end{cases} \quad \text{Eq. 2.3}$$

The peak value ( $\tau_{max}$ ) can be obtained by the compressive strength of concrete ( $f'_c$ ) and the according slip ( $s_{peak}$ ) can be calculated by bar diameter ( $d_b$ ):

$$\begin{aligned} \tau_{max} &= 1.163 f'_c{}^{3/4} \text{ (in MPa)} \\ s_{peak} &= 0.07 d_b \text{ (in mm)} \\ s_R &= 0.4 \sim 0.6 d_b \end{aligned} \quad \text{Eq. 2.4}$$

where  $s_R$  is the clear spacing between the ribs on the rebars. Figure 2.3 (a) displays the total bond resistance divided into two components: bearing resistance and friction resistance, which are defined by Eq. 2.3~2.4.



**Figure 2.3** Bond stress-versus-slip law

The total bond resistance curve (solid line) initially increased with slip, reaching a peak bond strength  $\tau_{max}$  at a slip value labeled  $s_{peak}$ . Then, the total bond resistance decreased with the further slip, illustrating a softening behavior. Eventually, the curve stabilized at a residual bond resistance level  $0.25 \tau_{max}$  as slip continues to increase.

### 2.1.2.2 Dynamic Bond Behavior

Understanding the bond-slip interaction between reinforcing bars and concrete is essential for evaluating the performance of reinforced concrete structures, particularly when exposed to dynamic loads, like blast and impact. Research has consistently shown that bond strength increases with a higher loading rate [17], [18], [19], [20], [21], which is vital for accurate numerical modeling and analysis of RC structures under these severe conditions.

Liu et al. further investigated the strain rate effect on the bond-slip relationship through a series of dynamic pullout tests with strain rates ranging from 1.67E-4/s to 100/s. They proposed a simplified rate-dependent bond-slip relation, which is validated in field blast tests using LS-DYNA [16]. In Figure 2.3 (b), the relationship of slip ( $s$ ) and bond strength ( $\tau$ ) generally present a brittle behavior. The bond strength increases linearly with slip until it reaches the ultimate bond strength ( $\tau_u$ ), slope of the curve is bond shear modulus ( $G$ ). Once the slip surpasses the ultimate bond strength is  $s_u$ , the bond strength drops sharply, implying a brittle failure, shown as the below equations:

$$\tau = \begin{cases} s \times G, & s \leq s_u \\ 0, & s > s_u \end{cases} \quad \text{Eq. 2.5-1}$$

The dynamic increase factor ( $DIF$ ) of shear modulus ( $DIF^G$ ) and ultimate bond strength ( $DIF^\tau$ ) expressed by strain rate  $\dot{\epsilon}$  as follows:

$$\begin{aligned} \frac{G_d}{G_s} &= 0.0041\dot{\epsilon} + 1.0033 \left( R^2 = 0.9593 \right), \text{ for } 2/s, \dot{\epsilon}, 100/s \\ \frac{\tau_{ud}}{\tau_{us}} &= 0.0038\dot{\epsilon} + 1.175 \left( R^2 = 0.8462 \right), \text{ for } 2/s, \dot{\epsilon}, 100/s \\ s_{\max} &= \frac{\tau_{ud}}{G_d}, \text{ for } 2/s, \dot{\epsilon}, 100/s \end{aligned} \quad \text{Eq. 2.5-2}$$

where,  $G_d$  and  $G_s$  are dynamic and static bond shear modulus, respectively, which are in N/mm<sup>3</sup>.  $\tau_{ud}$  and  $\tau_{us}$  are dynamic and static ultimate bond strength, respectively, which are in MPa. The static ultimate bond strength is depended on compressive strength of concrete obtained from the quasi-static pullout tests, shown as:

$$\begin{aligned} \tau_{us} &= 0.175f_c + 14.457 \\ G_s &= \frac{\tau_{us}}{s_{us}} \end{aligned} \quad \text{Eq. 2.5-3}$$

Liu et al. further validated the dynamic bond-slip relationship through drop weight impact tests [22]. Their findings indicated the dynamic bond strength had a minimal effect on predicting the peak impact force and maximum displacement response. However,  $DIF$  significantly influenced the impact force profile and dynamic behavior in the later stages of loading, particularly the residual deformation. To accurately predict the residual responses of RC structure,  $DIF$  of bond strength should be considered in the numerical modeling methods.



### 2.1.3 Gaps in Current Pull-out Models

Overall, the existing numerical studies on single GSS connections under tensile loads exhibit two significant gaps: (1) The use of solid elements for modeling rebar in full-scale structures is impractical due to excessive computational demands and increased modeling complexity. (2) The current surface-to-surface contact models utilizing Coulomb friction law fail to accurately represent the actual bond-slip behavior between grout and rebar. Additionally, they do not adequately incorporate the dynamic increase factor (*DIF*) necessary for simulating rapid pull-out scenarios.

## 2.2 Push-over Models

In previous studies, two main modeling methods have been distinguished for simulating precast structures embedded with GSSs: 2D fiber sections modeling and 3D solid elements modeling. Understanding the differences and applications of both methods is crucial for selecting the appropriate approach based on the specific requirements of seismic analysis, simulating accuracy, and computational efficiency.

### 2.2.1 Fiber Section (2D) Modelling

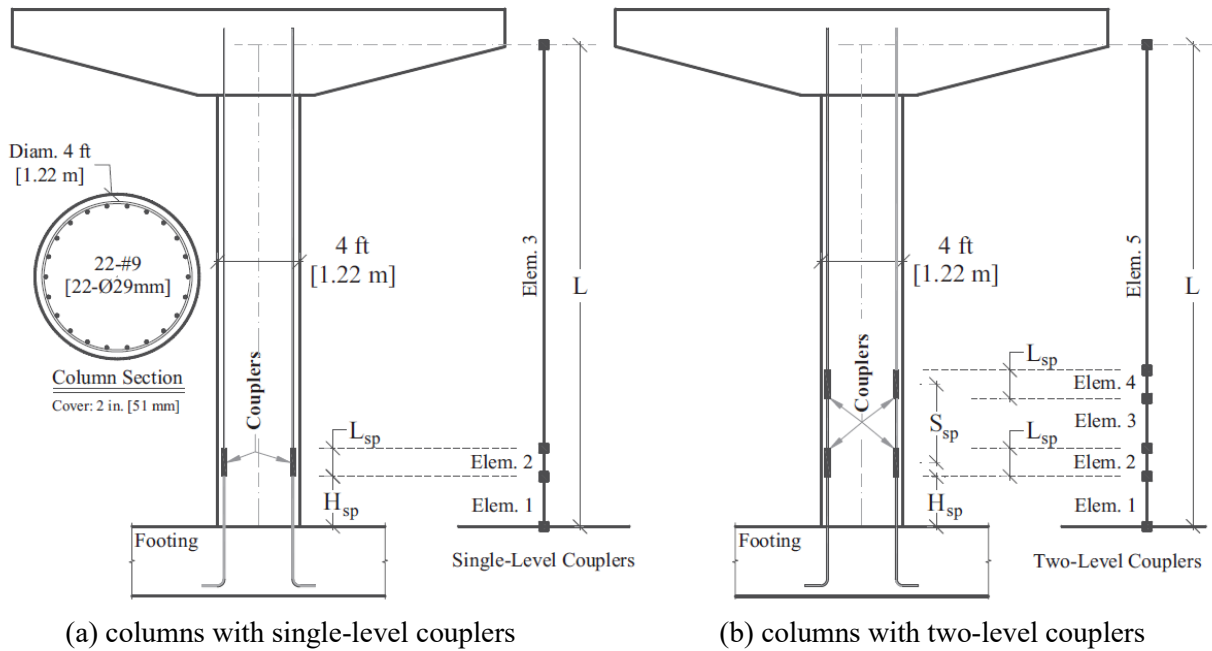
Tazarv et al. developed OpenSees models to simulate reinforced concrete (RC) columns with couplers by utilizing fiber elements to accurately represent various structural components such as the pedestal, coupler region, and remaining column sections [23], [24], [25]. These fiber elements enable the detailed modeling of nonlinear material behavior, as each fiber can possess its unique stress-strain relationship. Figure 2.4 is the configurations for columns with both single-level and two-level couplers.

In their modeling approach, a portion of the coupler length ( $\beta L_{sp}$ ) is assumed to be rigid, which reduces the strain levels of the coupler region ( $\varepsilon_{sp}$ ) compared with a non-spliced bar ( $\varepsilon_s$ ). The reduction factor is expressed in Eq. 2.6 [25].

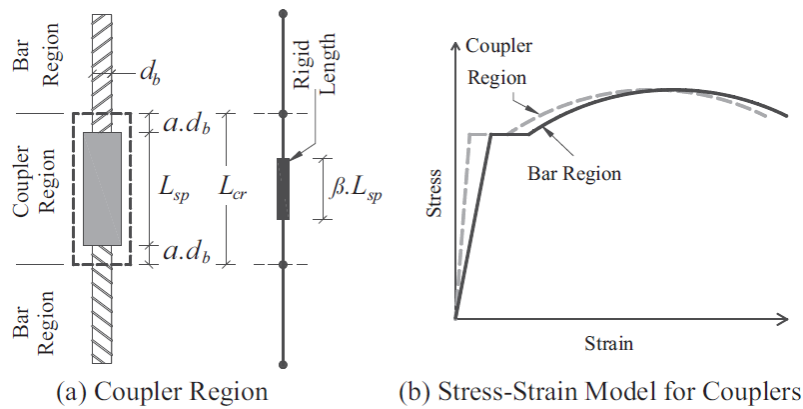
$$\frac{\varepsilon_{sp}}{\varepsilon_s} = \frac{L_{cr} - \beta L_{sp}}{L_{cr}} \quad \text{Eq. 2.6}$$

where,  $\beta$  is the coupler rigid length factor, and  $L_{sp}$  is the actual coupler length.

Based on this assumption, they propose a coupler stress-strain relationship, as illustrated in Figure 2.5. The coupler region length ( $L_{cr}$ ) should be less than 15 times the bar diameter ( $d_b$ ) to meet the seismic design requirement. This relationship has been verified and found to accurately account for the effects of couplers in the analysis and design of mechanically spliced elements.



**Figure 2.4** OpenSees model details [25]



**Figure 2.5** Stress-strain model for couplers [25]

Haber utilized OpenSees to develop a model consisting of seven elements to simulate the behavior of RC columns with couplers, as shown in Figure 2.6 [4]. The coupler region was modeled using a distributed plasticity frame element with two distinct fiber sections. The first fiber section was applied to element 2 (E2), covering sections s2 to s4. This section incorporated effective material properties of the grouted sleeve, utilizing a simplified constitutive relationship that represented the equivalent stress-strain behavior of the grout sleeve, as depicted in Figure 2.7 (a). In this fiber section, the sleeve was designed to carry both tension and compression forces. The second fiber section for E2 was applied at nodes n1 and n3, using the true material properties of the cast-iron sleeve, as illustrated in Figure 2.7 (b). To account for bond-slip effects, the rotations at the base of the column and the top of the GSS were modeled using rotational springs. Specifically, the rotation at the base of the column caused by bond-slip was determined through moment-curvature analysis, as illustrated in Figure 2.7 (c). The models developed by Haber showed good agreement with experimental results.

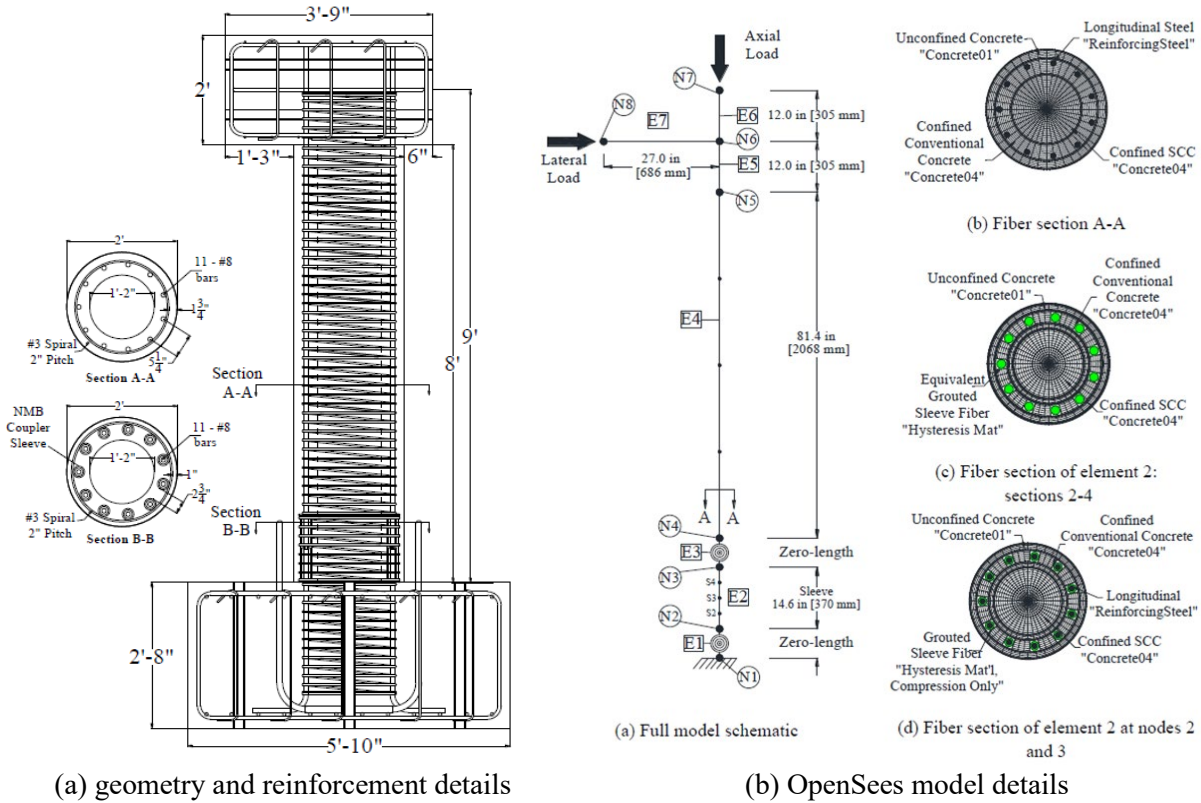


Figure 2.6 Analytical model of precast column with GSSs [4]

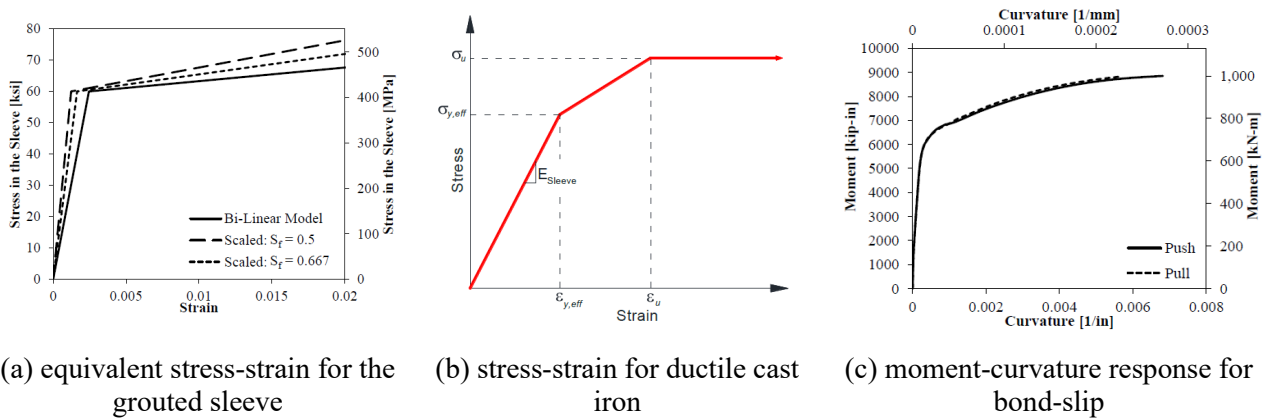


Figure 2.7 Proposed element's models [4]

Ebrahimpour et al. analyzed three Idaho bridges using the modeling method based on Haber's approach. The detailed bond-slip procedure and the corresponding OpenSees input files were comprehensively documented in their report [3]. Their analysis indicated all three bridge columns performed well under the seismic conditions. As illustrated in Figure 2.8, the bond-slip relationship was defined in terms of the moment and rotation. The rotation due to slip ( $\theta_{slip}$ ) can be expressed as:

$$\theta_{\text{slip}} = \tan^{-1} \left( \frac{\delta_{\text{slip}}}{c-d} \right)$$

$$c = 2.65 + \frac{|\varepsilon_c|}{(\varepsilon_t - \varepsilon_c)} (18.37) \text{ in.}$$

Eq. 2.7-1

where,  $d$  is the column diameter.  $\varepsilon_t$  and  $\varepsilon_c$  are the steel tensile and compressive strains, respectively. The slip ( $\delta_{\text{slip}}$ ) can be calculated using:

$$\delta_{\text{slip}} = \begin{cases} \frac{\varepsilon_s L_1}{2} & \text{if } \varepsilon_s \leq \varepsilon_y \\ \frac{\varepsilon_y L_{1y}}{2} + \frac{(\varepsilon_s + \varepsilon_y) L_2}{2} & \text{if } \varepsilon_s > \varepsilon_y \end{cases}$$

$$L_1 = \frac{f_s d_b}{4u}$$

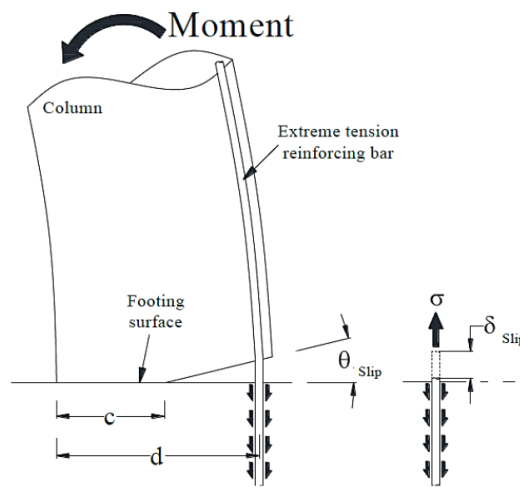
$$L_2 = \frac{(f_s - f_y) d_b}{4u}$$

$$u = \frac{9.5 \sqrt{f'_c}}{d_b} \leq 800 \text{ psi}$$

Eq. 2.7-2

where,  $\varepsilon_s$  and  $\varepsilon_y$  are tensile and yield strains of the extreme location's steel, respectively.  $f_s$  is the stress in the extreme tension steel,  $f_y$  is the steel yield strength,  $d_b$  is the diameter of the bar, and  $f'_c$  is the core concrete compressive strength.

These equations and the schematic of bond-slip rotation (Figure 2.8) provide a clear understanding of the bond-slip mechanics.



**Figure 2.8** Schematic of bond-slip rotation [3]

Overall, the fiber section (2D) can effectively model the behavior of GSS connections and the bond-slip mechanics and can further simulate the nonlinear and hysteretic responses of RC columns with GSSs under seismic loads. The benefits of 2D modeling include computational efficiency compared to full 3D solid modeling, making it especially advantageous for analyzing large structures. However, fiber sections are simplified representations and may not fully capture the complex 3D stress states. It is crucial to understand how the GSS system has been modeled in RC columns using solid elements.

### 2.2.2 Solid Element (3D) Modelling

Qiao et al. conducted four tests on grouted sleeve column base joint specimens under low cyclic loading with constant axial compression and developed FE models using ABAQUS [26]. These models were compared with experimental results, focusing on failure modes (no bond failure) and bearing capacity, showing good agreement with the experimental data. The concrete, grouting material, and grouted sleeve were modeled using solid elements (C3D8R), while the rebar was modeled with three-dimensional truss elements (T3D2), shown as Figure 2.9 (a). In the models, bond-slip effects between concrete and rebar were neglected. For the grouted sleeve system, the sleeve and its internal grouting material were connected using a *binding* (tie) constraint. Additionally, grouting material within the sleeve and rebar were connected using the *embedded* constraint, which means the motion of the rebar nodes was constrained by the concrete nodes, without considering any bond-slip between them.

Ding et al. developed FE models of precast columns with GSSs using ABAQUS and validated the load-deformation response and failure modes under cyclic loading against experimental results, observing good agreement [27]. In their models, concrete was represented using solid elements (C3D8R), while reinforcement bars were modeled with truss elements (T3D2), shown as Figure 2.9 (b). The grouted sleeve was simplified as a cylindrical steel shell (S4R) surrounding the reinforcement, with a bilinear stress-strain model incorporating strain hardening. Both the grouted sleeves and reinforcements were embedded within the concrete elements using *embedded* constraints. Bond-slip effects between the grout and steel bars and between the grout and GSS, were not considered in the models.

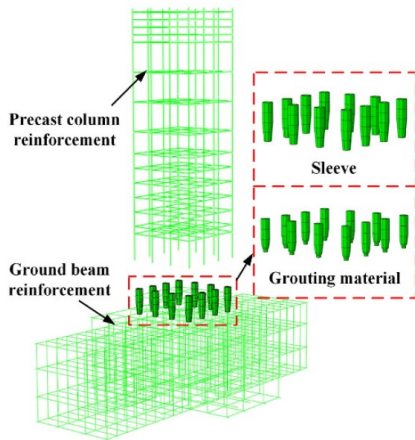
Wu et al. (2020) conducted both experimental and numerical studies to investigate the seismic behavior of precast short-leg shear walls connected with grouting sleeves under low-cyclic reversed loading. FE models were developed using ABAQUS and validated against experimental results, showing good correlation. The stress distributions of the rebar and grouted sleeve, as illustrated in Figure 2.9 (c) [28]. In the FE models, concrete, grouting material, and grouting sleeves were modeled using solid elements (C3D8R), while the reinforcing bars were represented by three-dimensional truss elements (T3D2). The contact interfaces between the grouting sleeve and the internal grouting material, and between the grouting sleeve and the external concrete, were assumed to be perfectly bonded. Consequently, no bond-slip effects between the grouted material, grouted sleeve, and steel were considered in the simulations.

Xia et al. employed a combination of quasi-static cyclic experiments and numerical simulations to investigate the seismic performance of columns with GSSs under various levels of steel corrosion. In their study, FE models were developed using ABAQUS [29]. The concrete, grouting material, longitudinal steel bars, and sleeves were modeled using solid elements (C3D8R), while the stirrups and steel bar cages at the base were represented using truss elements (T3D2), shown as Figure 2.9 (d). To simulate the bond-slip behavior between the steel bars and the surrounding concrete and grouting material, a surface-to-surface contact with the Coulomb friction model was applied.

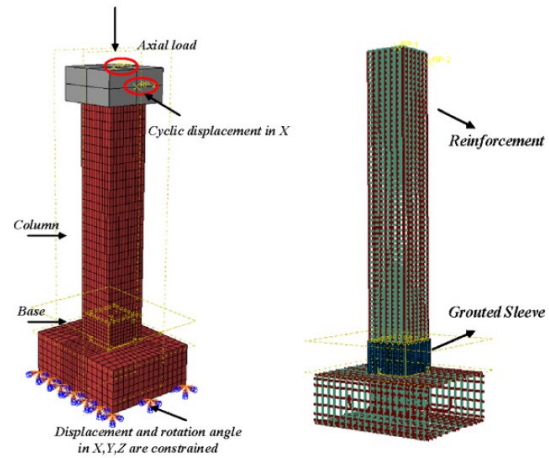
Lu et al. established FE models of beam-column joints with double-grouted sleeves using ABAQUS, achieving theoretical predictions that aligned well with the numerical results [30]. The FE models incorporated precast concrete, grout, grouting mortar, sleeves, and loading plates using solid elements (C3D8R). For modeling the reinforcement and transition rebar, truss elements (T3D2) were utilized,

shown as Figure 2.9 (e). In their modeling approach, the reinforcing bars, transition bars, sleeves, and grout were embedded with the assumption of a perfect bond, as no significant bond slip was observed.

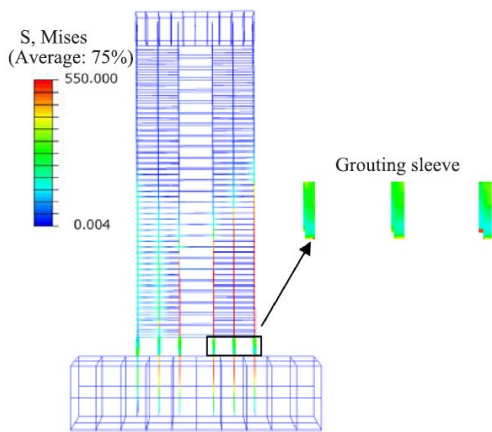
Xu et al. investigated the seismic performance of RC columns with GSS connections using FE analysis with the software ATENA [31]. In their study, the columns, steel sleeves, steel plates, and grouting layers were modeled using solid elements, while the reinforcing bars were represented with truss elements, shown as Figure 2.9 (f). A fixed contact was established between the steel sleeves and the grouting material to simulate the interaction. To accurately capture the bond-slip behavior, a nonlinear bond-slip relationship was implemented for the bond strength. The validity of this bond strength model was confirmed through a simulation of the pull-out behavior of the steel bar within the grouted sleeve.



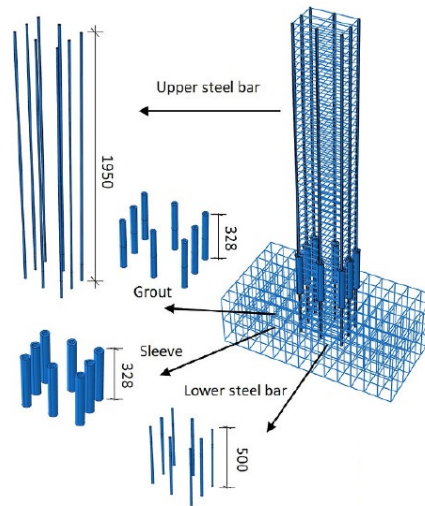
(a) Qiao et al. (2022) [26]



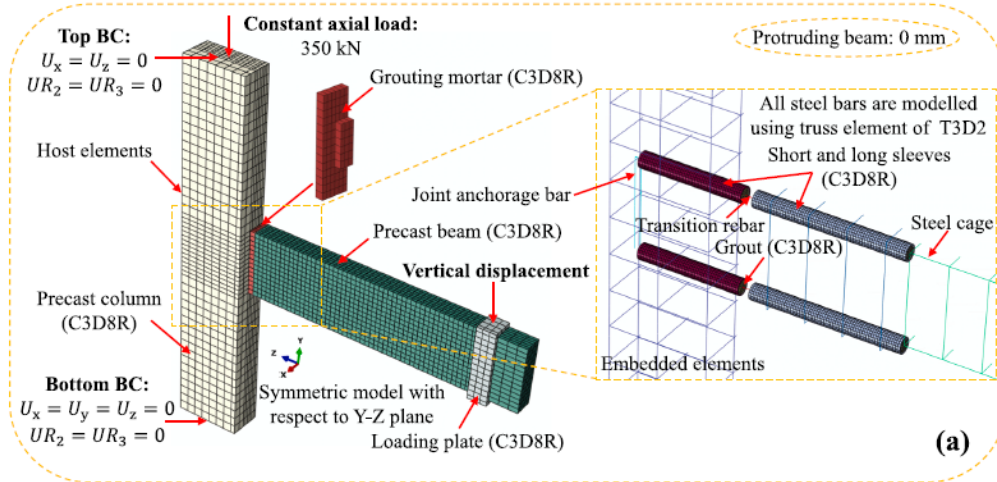
(b) Ding et al. (2022) [27]



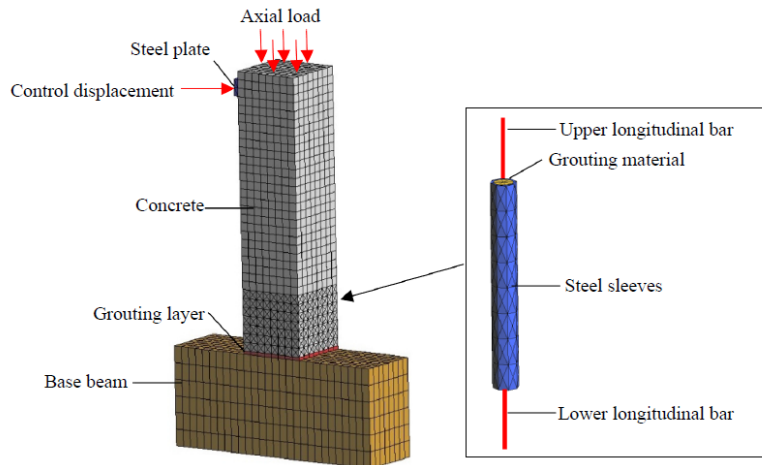
(c) Wu et al. (2020) [28]



(d) Xia et al. (2023) [29]



(e) Lu et al. (2023) [30]



(f) Xu et al. (2022) [31]

**Figure 2.9** FE models or result in previous studies

Generally, the use of solid elements (3D) provides a detailed representation of localized effects, such as stress concentrations and material nonlinearity, offering a more thorough depiction of stress states. This method can effectively capture the nonlinear responses of GSS connections under seismic loads, resulting in a more comprehensive and accurate simulation of both RC columns and the GSS system. However, this increased accuracy comes at the cost of higher computational demands. Notably, most prior research has often neglected the bond-slip relationship between rebar and the surrounding materials, leaving the risk of potential bond failure in the couplers unaddressed.

The critical information about GSS and RC column models and bond-slip models from various studies is summarized in Table 2.2. Typically, 2D models excel at capturing bond-slip relationships, while 3D models often neglect these interactions, focusing instead on detailed local concrete stress concentrations. This research study aims to develop a 3D model that includes a comprehensive bond-slip law.

**Table 2.2** Numerical studies on FE models of push-over tests

References	Software	GSS models	Column models	Bond-slip models
Tazarv et al. (2016) [25]	OpenSees	Fiber elements	Fiber elements	Moment-curvature response
Haber (2013) [4]	OpenSees	Elements with two distinct fiber sections	Fiber elements	Moment-curvature response
Ebrahimpour et al. (2016) [3]	OpenSees	Elements with two distinct fiber sections	Fiber elements	Moment- rotation response
Qiao et al. (2022) [26]	ABAQUS	Sleeve: solid Grout: solid Rebar: truss	Concrete: solid elements with Concrete Damage Plasticity (CDP) model	Sleeve- Grout: <i>binding</i> (tie) Grout-Rebar: <i>embedded</i> without bond-slip
Ding et al. (2022) [27]	ABAQUS	Grout and Sleeve: shell Rebar: truss	Concrete: solid elements with CDP model	No bond-slip is considered
Wu et al. (2020) [28]	ABAQUS	Sleeve: solid Grout: solid Rebar: truss	Concrete: solid elements with CDP model	No bond-slip is considered
Xia et al. (2023) [29]	ABAQUS	Sleeve: solid Grout: solid Rebar: solid	Concrete: solid elements with CDP model	Surface-to-surface contact with Coulomb friction model
Lu et al. (2023) [30]	ABAQUS	Sleeve: solid Grout: solid Rebar: truss	Concrete: solid elements with CDP model	No bond-slip is considered
Xu et al. (2022) [31]	ATENA	Sleeve: solid Grout: solid Rebar: truss	Concrete: solid elements with the fracture–plastic model	Nonlinear Bond-slip relationship

### 2.2.3 Gaps in Current Push-over Models

Generally, both 2D and 3D modeling approaches have demonstrated effectiveness in accurately capturing the nonlinear and hysteretic responses of reinforced concrete (RC) columns with grout splice sleeves (GSS) under seismic loads. Specifically, 2D fiber section models offer computational efficiency, while 3D solid element models provide the ability to capture complex stress states within elements. However, there are two notable gaps in these studies: (1) In 2D models, the bond-slip behavior between grout and rebar was incorporated into a rotational element at the base of the column, reflecting the moment-curvature response. This approach failed to provide detailed stress states and explanations of the failure mechanisms within the GSS region under hazardous conditions. (2) In 3D models, the rebar was embedded in the grout without considering grout failure or the bond-slip behavior between the grout and rebar. It left the potential risk of bond failure in the couplers unaddressed.



## 2.3 Impact Models



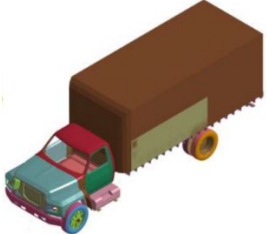

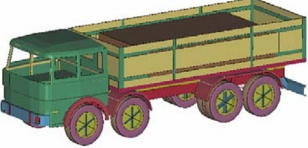
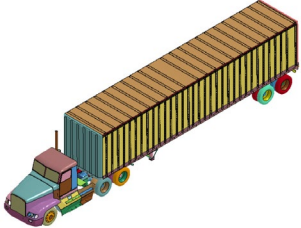
Impact models generally consist of two main components: the structural element and the impactor, which can be a vehicle or an impact hammer. Due to the wide variety of vehicle models in current use, it is crucial to establish clear categorizations for both the types of impact vehicles and the corresponding ranges of impact velocities. Additionally, there is a notable scarcity of research focused on the impact behavior of concrete structures with GSS connections. The critical information from current impact studies on GSS and connection interface models and bond-slip models are summarized in this section and serves as a valuable reference for modeling purposes.

### 2.3.1 Vehicle Impact

In the United States, highway bridge pier columns design is governed by the AASHTO Load and Resistance Factor Design (LRFD) Bridge Design Specifications. According to the AASHTO LRFD, reinforced concrete (RC) pier columns should be designed to withstand an equivalent static force (ESF) of 600 kips (2,670 kN) positioned five feet (1.52 meters) above the ground [32]. This loading condition is based on full-scale tests where 910-mm diameter rigid columns are subjected to impacts from a 36.3-ton tractor-trailer with speed of 80.5 km/h [33], [34].

Most studies on vehicle impacts utilize LS-DYNA software, which can perform nonlinear impact simulations, offers a wide range of material models and provides pre-developed vehicle FE models. The publicly available FE models include a 0.893-ton Toyota Yaris, a 1.997-ton Dodge Ram, an 8-ton Ford F800 truck, a 16-ton HGV truck, a 30-ton IVECO truck, and a 38-ton tractor-trailer[35], [36], [37]. Vehicles are categorized as light, medium, and heavy based on their total weight [38], [39], shown as in Table 2.3. Velocity is another critical factor influencing the severity of the impact, which is classified as low, intermediate and high [38], [39], as shown in Table 2.4.

**Table 2.3** Categorization of impact vehicle

Weight level	Types of vehicles	FE models	Total mass (ton)	Engine mass (ton)	Cargo mass (ton)
<b>Light</b> (passenger cars <2.722 ton)	Toyota Yaris		0.9	0.068	-
	Dodge Ram		2	0.22	-
<b>Medium</b> 2.722 ton < (commercial vehicle) < 11.793 ton	Ford F800 Single Unit Truck		8	0.64	4.88
<b>Heavy</b> (trucks) > 11.793 ton	HGV truck		16	1.27	8.53
	IVECO truck		30	1.09	21.95
	Tractor-trailer		38	1.27	24.60

**Table 2.4** Categorization of impact velocity

Level	Velocity of vehicle
<b>Low</b>	$\leq 15$ m/s (35 miles/h)
<b>Intermediate</b>	$> 15$ m/s (35 miles/h) and $< 27$ m/s (60 miles/h)
<b>High</b>	$\geq 27$ m/s (60 miles/h)

### 2.3.2 Structure Models

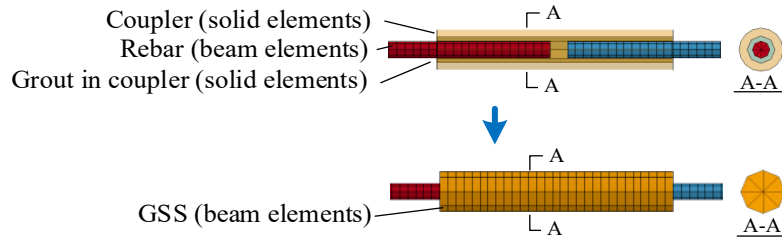
Li et al. performed numerical investigations to analyze the impact behavior of precast beams with GSS connections using the LS-DYNA software [40]. The numerical models are calibrated against experimental results in terms of impact force, reaction force, midspan displacement, and failure modes. In their models, solid elements represented the concrete, while beam elements modeled the rebar and GSS system, as depicted in Figure 2.11 (a). The grout interfaces between the precast component and the cast-in-place part were also modeled using solid elements with a concrete material model (MAT\_72R3), employing a lower concrete strength of 36.7 MPa compared to the precast concrete.

Li et al. proposed a simplified modeling approach for the GSS system. Unlike the models discussed in Section 2.2.2, this method simplified the sleeve to a beam element with an equivalent cross-sectional area, elastic modulus, and yield stress of the GSS system, as shown in Figure 2.10. The equivalent elastic modulus ( $E_c$ ) and equivalent yield stress ( $\sigma_c$ ) can be determined by Eq. 2.8.

$$E_c = \frac{E_s A_s + E_g A_g + E_r A_r}{A} \quad \text{Eq. 2.8}$$

$$\sigma_c = \frac{\sigma_s A_s + \sigma_g A_g + \sigma_r A_r}{A}$$

where,  $A_s$ ,  $A_g$  and  $A_r$  are the sectional areas of the coupler, grout in coupler and rebar, respectively;  $E_s$ ,  $E_g$  and  $E_r$  are the elastic modulus of the coupler, grout in coupler and rebar, respectively;  $\sigma_s$ ,  $\sigma_g$  and  $\sigma_r$  are the yield stress of the coupler, grout in coupler and rebar, respectively.  $A$  represents the total area of the grout sleeves.



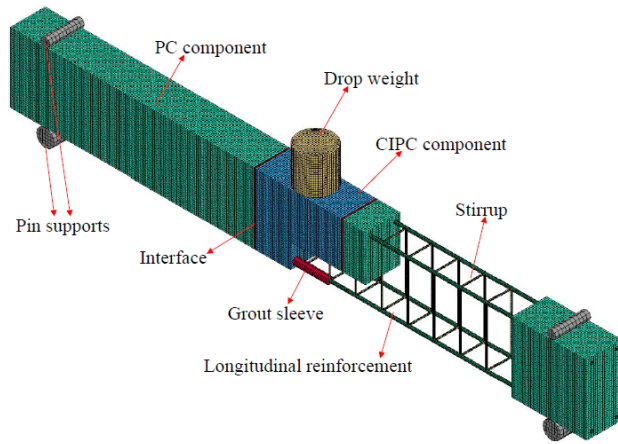
**Figure 2.10** Schematic diagram of grout sleeve

The keyword \*CONSTRAINED\_BEAM\_IN\_SOLID was used to embed the rebar and grout sleeve beam elements into the concrete solid elements. This coupling method constrained the nodes of the beam elements to the solid elements in both normal and tangential directions. No bond-slip behavior was considered in their study.

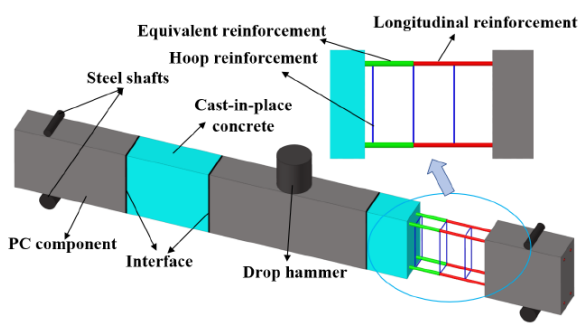
Zhou et al. investigated the dynamic behavior of precast beams connected by GSSs under impact loads using numerical simulations with the LS-DYNA program [41]. Their numerical model was evaluated and calibrated against experimental data, focusing on damage, impact forces, and displacement. In their study, solid elements (Solid 164) were employed to simulate the concrete and the drop hammer, while beam elements (Beam 161) were used to model the reinforcement and grout sleeve, as shown in Figure 2.11 (b). Following the equivalent method proposed by Li et al. (2019) [40], the GSS was simplified using beam elements with equivalent cross-sectional properties. The grout interface was represented by a thin layer of solid elements, maintaining the same concrete strength as that of the precast concrete. This study assumed no bond-slip behavior between the reinforcement, grout sleeve, and concrete.

Su et al. conducted an in-depth investigation into the shear mechanism and strength of a GSS connections using ultra-high-performance concrete (UHPC) through both experimental and numerical methods [42]. FE models were developed using LS-DYNA and validated by comparing failure modes and load-displacement curves with experimental results. In their FE models, solid elements (Solid 164) were utilized to represent the UHPC, while beam elements (Beam 161) were used to model the reinforcement and grouted sleeve. The grouted sleeve was simplified following the equivalent method proposed by Li et al. (2019) [40], as shown in Figure 2.11 (c). To accurately capture the interface behavior, including bonding, failure, and post-failure slip, the keyword `AUTOMATIC_SURFACE_TO_SURFACE_TIEBREAK` (`ASTS_TIEBREAK`) was employed. The study did not consider bond-slip behavior between the grout sleeve and the rebar.

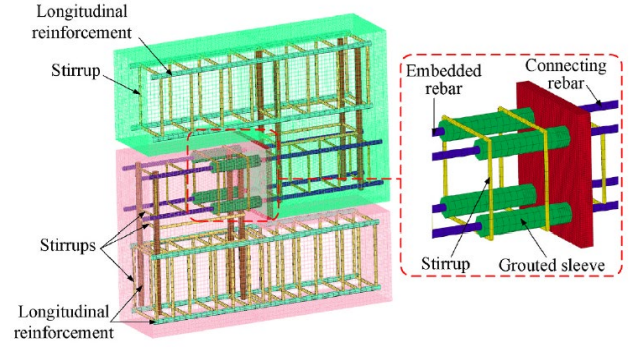
Sun et al. performed a truck-bridge collision analysis on a prototype highway bridge utilizing GSS connections by LS-DYNA [43]. In the FE models, concrete was represented using solid elements (Solid 164), while the reinforcement and grouted sleeve were modeled with beam elements (Beam 161). The grouted sleeve was simplified using the equivalent method suggested by Li et al. (2019), as depicted in Figure 2.11 (d). `ASTS_TIEBREAK` keyword was employed to represent interface behavior. Perfect bond assumptions were made for the connections between the reinforcing steel and column concrete, and between the grout sleeve and rebar.



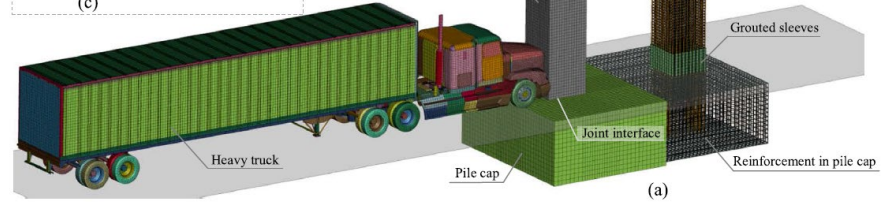
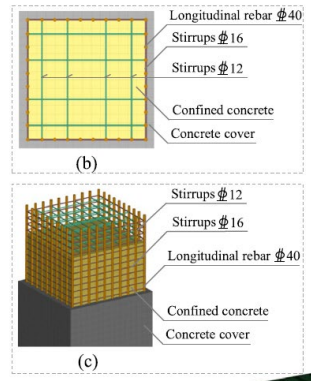
(a) Li et al. (2019) [40]



(b) Zhou et al. (2022) [41]



(c) Su et al. (2023) [42]



(d) Sun et al. (2022) [43]

**Figure 2.11** FE models in previous studies

The critical information about GSS and connection interface models and bond-slip models from various studies is summarized in Table 2.5. In existing studies, all components of GSS systems (i.e., the coupler, rebar, and grout) were often simplified using beam elements with equivalent properties. These models generally neglected the bond-slip behavior between the grout and the rebar and did not incorporate dynamic increase factors (*DIF*) of bond-slip law for enhanced accuracy in dynamic loading scenarios.

**Table 2.5** Numerical studies on FE models of impact tests

References	Software	GSS models	Connection interface models	Bond-slip models
Li et al. (2019) [40]	LS-DYNA	Beam elements with equivalent parameters	Solid elements with concrete material model (lower concrete strength than PC)	No bond-slip was considered
Zhou et al. (2022) [41]	LS-DYNA	Beam elements with equivalent parameters	Solid elements with concrete material model (same concrete strength as PC)	No bond-slip was considered
Su et al. (2023) [42]	LS-DYNA	Beam elements with equivalent parameters	Contact (ASTS_TIEBREAK) with interface behavior	Include in connection interface models
Sun et al. (2022) [43]	LS-DYNA	Beam elements with equivalent parameters	Contact (ASTS_TIEBREAK) with interface behavior	Include in connection interface models

### 2.3.3 Gaps in Current Impact Models

Research on structures with GSS connectors under impact loads is limited, revealing two significant gaps: (1) Current models often neglect the bond-slip interaction between grout and rebar, potentially underestimating the formation of microcracks in the grout and the likelihood of bond failure. Additionally, these models are inadequate in providing data to detect non-visible damage within the coupler system (i.e., coupler, rebar, and grout) under such conditions. (2) These models fail to integrate dynamic increase factors (*DIF*) into the bond-slip relationship, neglecting the increased bond strength that occurs at higher loading rates.

## 2.4 Summary

This chapter presents a comprehensive review of relevant research, focusing on numerical studies involving pull-out tests, push-over tests, and impact tests.

It provides a detailed summary of grout behavior in couplers and the bond-slip relationship between grout and rebar. The review identifies existing numerical studies on single GSS connections under tensile loads are impractical due to the excessive computational demands and complexity of using solid elements. Additionally, current surface-to-surface contact models employing Coulomb friction law fail to accurately represent bond-slip behavior and do not incorporate the dynamic increase factor (*DIF*) necessary for simulating rapid pull-out scenarios.

To determine the most suitable approach for seismic analysis in terms of simulation accuracy and computational efficiency, this chapter compares 2D fiber section modeling and 3D solid element modeling. While 2D models offer computational efficiency, they fail to provide detailed stress states and explanations of failure mechanisms within the GSS region under hazardous conditions. Conversely, 3D models, although more detailed, often overlook grout failure and the bond-slip behavior between grout and rebar, leaving the potential risk of bond failure in the couplers unaddressed.

The chapter concludes by clarifying the categorizations for impact vehicle types and ranges of impact velocities. It also summarizes the modeling methods for GSS connections, including interface and bond-slip models. Notably, no existing studies consider the bond-slip interaction between grout and rebar, potentially underestimating the formation of microcracks and the likelihood of bond failure. Furthermore, the simplified modeling approaches for GSS systems are inadequate in detecting non-visible damage within the coupler system (i.e., coupler, rebar, and grout) under impact conditions, and they fail to integrate *DIF* into the bond-slip relationship, neglecting the increased bond strength at higher loading rates.

This research aims to address significant gaps identified in the existing literature by developing an advanced FE model. The proposed model utilized beam elements for the rebar to enhance computational efficiency, while employing solid elements for the grout, sleeve, concrete, and interface grout to capture detailed stress distributions and predict microcracks within the coupler. Furthermore, by incorporating both static and dynamic bond stress-slip laws, including the *DIF*, the model accurately predicted the likelihood of bond failure under various loading conditions. Additionally, the new modeling method enhanced the detection of non-visible damage within the coupler system. This advancement offers a deeper understanding of failure mechanisms in the coupler region, establishing a critical foundation for ensuring effective grout bonding and enhancing the overall safety of bridge systems under diverse loading conditions. Furthermore, the model provided essential data from impact simulations on precast columns with GSS connectors, facilitating the evaluation of bond strength reduction in post-impact GSSs. This comprehensive approach addresses key gaps in the literature and contributes to the development of more resilient and reliable bridge structures.

### 3. FE MODELS OF TEST SPECIMENS

To achieve time-efficient and accurate simulations, this section details the FE modeling approach. 3D models with the same dimensions as the experimental specimens were established. To ensure the FE model was well-validated, three key aspects were adjusted: material properties, mesh size sensitivity, and the bond-slip law of rebar and surrounding materials. The predictions from the validated models were then compared with experimental results under both static and dynamic scenarios. The developed FE modeling method was validated as feasible for predicting the strain response of columns with grouted sleeve splices in the elastic phase during static tests. Additionally, it effectively simulated the dynamic behavior of specimens under impact loading and the damage states after failure.

#### 3.1 Geometry Information

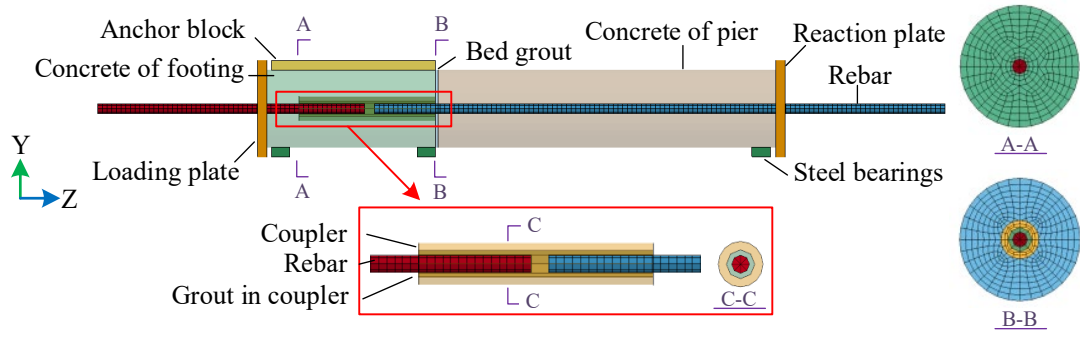
Using the software LS-DYNA, three-dimensional models were established to validate the mechanical behavior of the precast concrete columns with GSSs under static and dynamic scenarios, as shown in Table 3.1 (a) and (b). The cylindrical precast pier and footing have a diameter of eight inches, each of them embedded by a single longitudinal rebar with a diameter of one inch. These two parts connected by grout filled in a coupler. For modeling simplicity, the diameter of the coupler was chosen based on the average diameter of its narrow and wide ends, which is 2.52-inch outer diameter, 1.6-inch inner diameter, and 14.57-inch length. The pier part had an overall height of 36 inches, while the footing part had a height of 18 inches, joined by a 1/4-inch-thick bed grout.

As with the physical test specimens, two categories of pier-to-footing are built, a precast footing with connector embedded in the top of the footing (GSS-F), and a column base with connector (GSS-C), shown as Figure 3.1 (c) and (d). Models were designed with 18-inch rebars left on both sides. GSS-F had embedded a dowel bar (blue) of seven inches in the footing, while GSS-C had a seven-inch dowel (red) inserted into the pier.

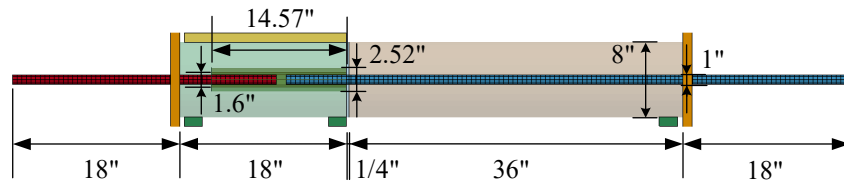
The loading system in the model was simplified, consisting of a loading plate and a reaction plate. The constraint system included three steel bearings and an anchor block located similarly to the test setup. For simplicity, all steels in the loading system and the constraint system were labeled as “accessory steels” in the following. The dimensions of each component matched the size used in the test.

The concrete, grout, GSS and accessory steel models were all established by SOLID\_164 elements. The reinforcements were modeled by BEAM\_161 elements. The reinforcements and concrete were allowed to have slip based on bond-slip law.

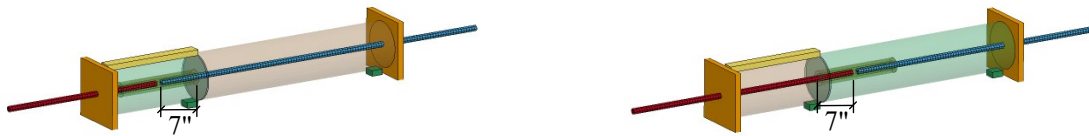




(a) Details of FE models



(b) Dimensions of FE models (unit: inch)



(c) GSS-F

(d) GSS-C

Figure 3.1 Geometry information of FE model

### 3.2 Contact and Boundary Conditions

For corresponding to the boundary condition of the specimen, all nodes of the bearings' bottoms, the right side of the reaction plate and top of the anchor blocks were fully constrained within three translational degrees of freedom by using the keyword \*BOUNDARY\_SPC\_SET. For the left-side nodes of the loading plate, their translational degrees of freedom in two directions (X and Y directions) were restrained other than free in the loading direction (Z direction), shown as Figure 3.2.

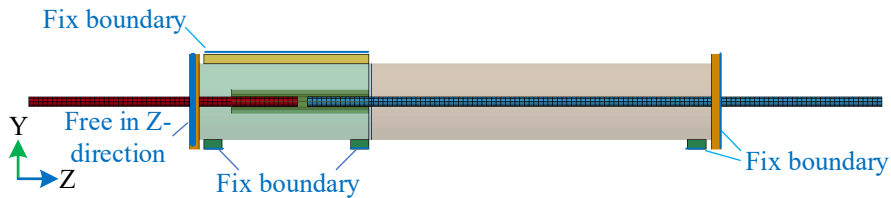


Figure 3.2 Boundary conditions

Due to the complex components in the model, it is crucial to clarify the contact situation in the software. To describe the contact between the specimens and the accessory steels, the \*CONTACT\_AUTOMATIC\_SURFACE\_TO\_SURFACE model was adopted, in which the static friction coefficient is 0.2 and the dynamic static friction is 0.15 [44]. However, due to the smooth outer surface of grouted sleeves, the bond behavior between sleeves and surrounding concrete was frictionless [45], which was adopted by using the method \*CONTACT\_AUTOMATIC\_SURFACE\_TO\_SURFACE with default parameters [46]. The interface contact between the bed grout and the precast concrete was determined by hard contact and penalty friction for normal and tangential constitutive behavior, respectively [47]. The joint contact was achieved by coulomb friction model \*CONTACT\_AUTOMATIC\_SURFACE\_TO\_SURFACE with friction coefficient 0.75 [48]. During our test, the GSS showed a strong connection performance, where it was observed there was no slip between the coupler and inner grout. Thus, a tied bond is adopted between the coupler and internal grouting material by using \*CONTACT\_TIED\_SURFACE\_TO\_SURFACE.

**Table 3.1** Contact setting key parameters in LS-DYNA

*CONTACT keywords	Slave	Master	FS	FD
AUTOMATIC_SURFACE _TO_SURFACE	Concrete	Loading plate	0.2	0.15
	Concrete	Reaction plate	0.2	0.15
	Concrete	Steel bearings	0.2	0.15
	Concrete	Anchor block	0.2	0.15
	Coupler	Concrete	-	-
	Bed grout	Concrete	0.75	0.75
TIED_SURFACE _TO_SURFACE	Grout in coupler	Coupler	-	-

Notes: In this table, FS is presented as static coefficient of friction, and FD is presented as dynamic coefficient of friction.

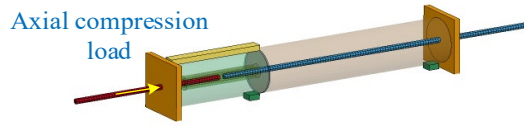
### 3.3 Loading Procedures

In LS-DYNA, the RESTART analysis mode was employed to effectively manage the sequence of loading after the system has been initialized for gravity and precompression. This approach facilitated the application of either static lateral loads or dynamic impact loads structured into two distinct scenarios.

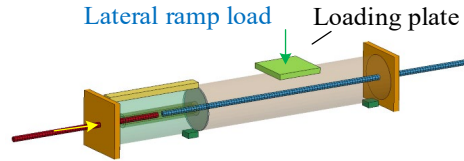
**Static scenario:** (1) Stress Initialization Stage: To replicate the initial stress state of the structure, self-weight was applied using the \*LOAD\_BODY\_Y with an acceleration curve. Prestressing loads were introduced at the same rate as observed in our experiments using \*LOAD\_RIGID\_BODY. Upon achieving static equilibrium, the state of the structure was saved for subsequent analysis. (2) Lateral Loading: Following stress initialization, a loading plate was introduced to apply lateral ramp loading via the \*LOAD\_RIGID\_BODY keyword.

**Dynamic Scenario:** (1) Stress Initialization Stage: Similar to the static scenario, the structure underwent a stress initialization stage. (2) Impact Loading: A loading plate was implemented for displacement control using \*BOUNDARY\_PRESCRIBED\_MOTION\_RIGID. Two specific impact velocities were tested in the simulations: 0.5 in./second for tests F1 and C1, and 2 in./second for tests F2 and C2.

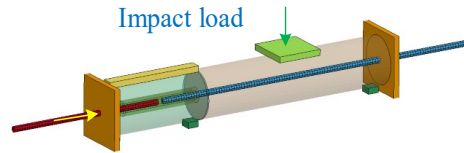
(1)  
Stress  
initialization  
stage



(2)  
Static  
loading stage



(3-a) Impact  
loading stage  
(velocity=0.5  
in./s)



(3-b) Impact  
loading stage  
(velocity=2  
in./s)

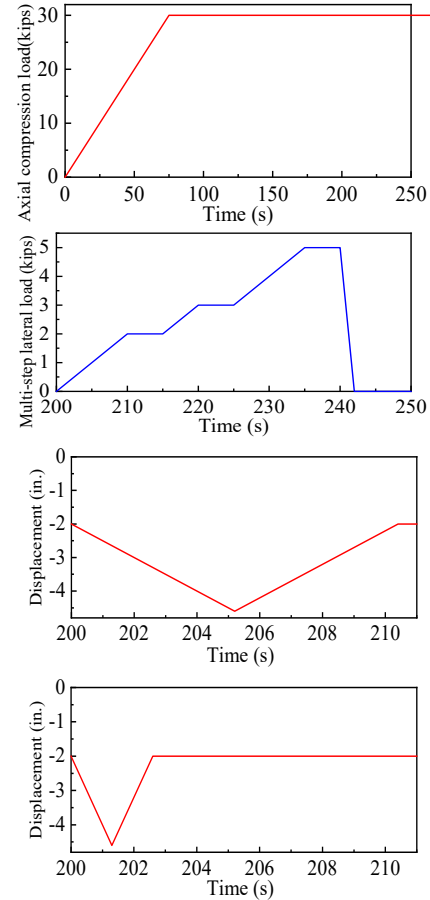


Figure 3.3 Loading stage description

### 3.4 Bond-slip Law

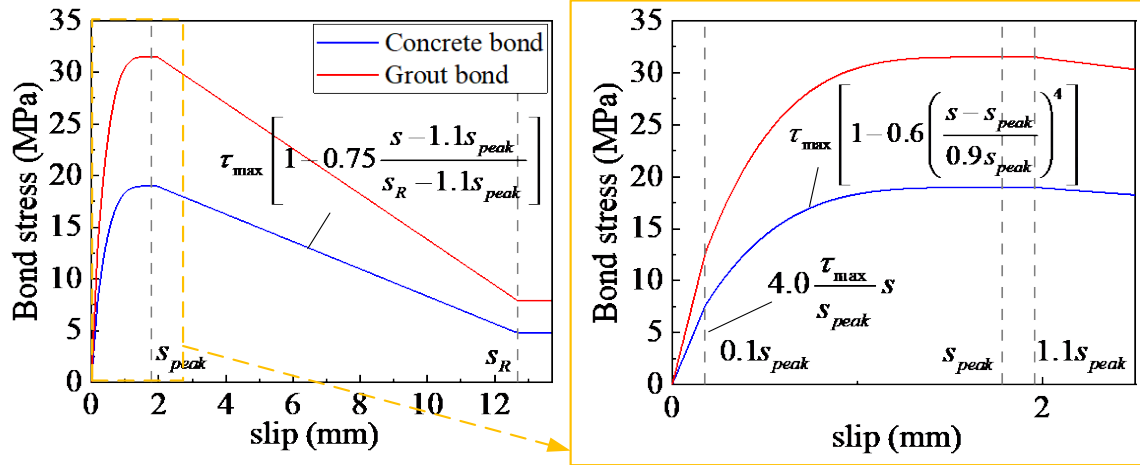
During the physical experiment, bond-slip failure was noted in the GSS-C specimens. To effectively predict the failure of the GSS system under impact loading, it was essential to simulate the bond-slip behavior of reinforcing bars accurately. To describe the bond-slip behavior, the bond-slip model proposed by Murcia-Delso et al. [13], [14], [15] was used, represented by Equations 2.3 and 2.4. This model was further adjusted by incorporating the dynamic increase factor for ultimate bond strength ( $DIF^*$ ) [16], as defined in Equation 2.5-2.

In LS-DYNA, bond force-slip law of reinforcement embedded in concrete or grout was established by using \*CONSTRAINED\_BEAM\_IN\_SOLID with a user defined function. This feature was released by setting the force-slip curve by flag AXFOR to a negative integer which refers to the \*DEFINE\_FUNCTION ID. In this case, CDIR had to be set to 1 to release the constraints along the beam axial direction. Given the varying compressive strengths of the bonding materials used, two distinct bond stress-slip laws were implemented in the model. The parameters associated with these laws are detailed in Table 3.2, and their respective curves are illustrated in Figure 3.4.

It is important to note when incorporating the bond stress-slip law under the keyword AXFOR, the stress values must be multiplied by the contact area to convert them into bond forces. It is also important to note the degradation of the bond-slip law is disregarded in scenarios involving cyclic loading.

**Table 3.2** Bond-slip setting parameters in LS-DYNA

Materials	$d_b$	$f'_c$	$\tau_{max}$	$s_{peak}$	$s_R$
Concrete	1 in. / 25.4 mm	6.0 ksi / 41.37 MPa	18.97 MPa	1.778 mm	12.7 mm
Grout	1 in. / 25.4 mm	11.8 ksi / 81.36 MPa	31.51 MPa	1.778 mm	12.7 mm



**Figure 3.4** Bond stress-slip laws for monotonic loading proposed by Murcia-Delso et al. [49]

According to the example in the LS-DYNA user's manual [50], the debonding force function includes three arguments: 'slip', 'leng' (both are internally calculated parameters), and '\*stiff' (an output argument). 'slip' refers to the relative axial displacement between the coupling node and the concrete or grout material, indicating its application to displacement in the negative axial direction. 'leng' represents the tributary length of the coupling node. Notably, stress is measured in GPa; therefore, forces should be converted to MPa by dividing by 1000. Additionally, the *DIF* is calculated based on the loading rate and incorporated into the function for  $\tau_{max}$ . Figure 3.5 and Figure 3.6 present the input cards for the bond-slip relationships of rebar-concrete and rebar-grout, respectively.

```

*CONSTRAINED_BEAM_IN_SOLID_ID
$#  coupid                                title
    1rebar_concrete
$#  slave  master  sstyp  mstyp          ncoup  cdir
    7      6      0      0              2      1
$#  start  end      0      axfor      pssf      0      xint
    0.0    0.0      0      -12        0.1      0      0

*DEFINE_FUNCTION
$#  fid
    12
$#
float force(float slip,float leng, float *stiff)
{
  float force,shear,pi,d,area,pf,fc,tmax,speak,sr;
  fc=41.37; tmax=1.175*1.163*pow(fc,3/4);
  d=25.4; speak=0.07*d; sr=0.5*d;
  pi = 3.1415926;pf=1.0;
  area = pi*d*leng;
  if (slip <0.1*speak)
  {shear = 4*tmax/speak*slip;}
  else if (slip>=0.1*speak && slip<speak)
  { shear = tmax*(1-0.6* pow((slip-speak)/(0.9*speak),4));}
  else if (slip>=speak && slip<1.1*speak)
  { shear = tmax;}
  else if (slip>=1.1*speak && slip<sr)
  { shear = tmax*(1-0.75*((slip-1.1*speak)/(sr-1.1*speak)));}
  else if (slip>=sr)
  { shear = 0.25*tmax;}
  force = shear*area/1000;
  *stiff = pf*area;
  return force;
}

```

**Figure 3.5** Input cards for bond-slip between rebar and concrete (force vs. slip) (units: mm-kg-ms-GPa)

```

*CONSTRAINED_BEAM_IN_SOLID_ID
$#  coupid                                     title
    2rebar_grout
$#  slave  master  sstyp  mstyp              ncoup  cdir
    7      3      0      1              0      0      2      1
$#  start  end      0      axfor          pssf      0      xint
    0.0    0.0      0      -13          0.1      0      0

*DEFINE_FUNCTION
$#  fid
    13
$#
float force(float slip,float leng, float *stiff)
{
    float force,shear,pi,d,area,pf,fc,tmax,speak,sr;
    fc=81.36; tmax=1.175*1.163*pow(fc,3/4);
    d=25.4; speak=0.07*d; sr=0.5*d;
    pi = 3.1415926;pf=1.0;
    area = pi*d*leng;
    if (slip <0.1*speak)
    {shear = 4*tmax/speak*slip;}
    else if (slip>=0.1*speak && slip<speak)
        { shear = tmax*(1-0.6* pow((slip-speak)/(0.9*speak),4));}
    else if (slip>=speak && slip<1.1*speak)
        { shear = tmax;}
    else if (slip>=1.1*speak && slip<sr)
        { shear = tmax*(1-0.75*((slip-1.1*speak)/(sr-1.1*speak)));}
    else if (slip>=sr)
        { shear = 0.25*tmax;}
    force = shear*area/1000;
    *stiff = pf*area;
    return force;
}

```

**Figure 3.6** Input cards for bond-slip between rebar and grout (force vs. slip) (units: mm-kg-ms-GPa)

Both types of bond-slip can be computationally time-consuming, and no bond failure between concrete and rebar was observed in the previous tests. Therefore, it was crucial to explore the impact of neglecting the bond-slip of rebar-concrete on the impact response prediction of the specimens. Specimen GSS-C, subjected to an impact velocity of 2 in./s, was chosen as the study case.

Two models with different concrete bond conditions were established and compared. Both models included bond-slip between rebar and grout, as shown in Figure 3.6. Specifically, one model incorporated the concrete bond-slip law, while the other excluded it. To achieve non-slip bond conditions in \*CONSTRAINED\_BEAM\_IN\_SOLID, the CDIR parameter was set to 0 to constrain the coupling node on rebars in all directions. Figure 3.7 displays the input cards for the model that ignores the bond-slip behavior between rebar and concrete.

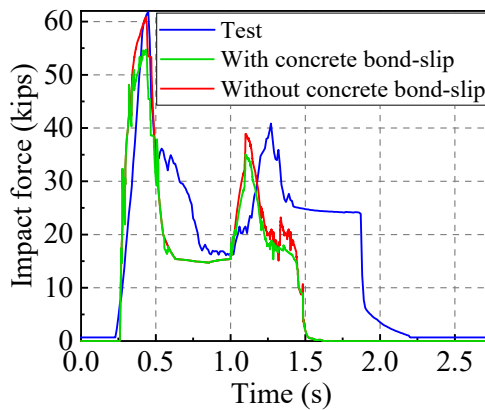
```

*CONSTRAINED_BEAM_IN_SOLID_ID
$#  coupid                                     title
    1rebar_concrete
$#  slave  master  sstyp  mstyp              ncoup  cdir
    7      6      0      0              0      0      2      0
$#  start  end      0      axfor          pssf      0      xint
    0.0    0.0      0      0              0.1      0      0

```

**Figure 3.7** Input cards for neglecting slip model between rebar and concrete

The analysis is done utilizing a supercomputer with 48 CPUs across two nodes, operating in 96 MPP parallel computation. The model incorporating both concrete and grout bonds required eight hours and 49 minutes to complete. In contrast, the model that only considers grout bond-slip completes in six hours and 32 minutes, saving 26% of computation time. Figure 3.8 compares the impact response of the structures with and without the bond-slip law of concrete-rebar. The model with and without the concrete bond-slip law showed differences of 11.42% and 1.58%, respectively, when compared to the first peak value of impact force. Additionally, there were differences of 14.25% and 4.73%, respectively, when compared to the second peak value. Reductions in the two impact forces experienced by the structure with concrete bond-slip were due to the relative movement between the rebar and concrete, which absorbed and dissipated some of the impact energy, resulting in lower recorded impact forces. Obviously, the model without the concrete bond-slip law provided more accurate predictions of the impact behavior of the precast concrete system and saved computation time. Therefore, only the bond-slip of grout-rebar was considered in the following studies.



**Figure 3.8** Comparison of the impact response with or without considering bond-slip of concrete-rebar

### 3.5 Material Properties

In LS-DYNA, concrete and reinforcement components were typically modeled separately, with several constitutive material models available to simulate the actual behavior of reinforced concrete structures under both static and dynamic loading conditions. Predicting the impact behavior of such structures was particularly challenging. Therefore, accurately determining the parameters for material models that are suitable for impact loads was crucial. It involved a rigorous comparison between experimental results and simulation data to ensure the models' calibration.

#### 3.5.1 Material Model for Concrete and Grout

\*MAT\_CSCM (Continuous Surface Cap Model) is designed to predict both elastic deformation and failure of concrete used in roadside safety applications under vehicle impact [51]. It is widely used in many recent impact simulations and can predict the concrete mechanical behavior under impact loading relatively well [52], [53]. Continuous Surface Cap Model is mainly referred to as a concrete model that combines the shear (failure) surface with the hardening compaction surface (cap) smoothly. This model provides isotropic constitutive models, failure and hardening surfaces, damage-based softening with erosion, and rate effects for high strain rate.

Rate effects are an important factor in dynamic behavior of concrete model under impacting. Rate effects are considered through increasing the fracture energy ( $G_f$ ), The dynamic fracture energy ( $G_f^{dyn}$ ) and the dynamic tensile/compression strength ( $f'^{dyn}$ ) are:

$$\begin{aligned} G_f^{dyn} &= G_f \left(1 + \frac{E \dot{\epsilon} \eta}{f'}\right)^{repow} \\ f'^{dyn} &= f' + E \dot{\epsilon} \eta \end{aligned} \quad \text{Eq. 3.1}$$

where,  $f'$  is the yield strengths before application of the rate effects.  $E$  is Young's modulus.  $\epsilon$  is the effective strain rate,  $\dot{\epsilon} = \sqrt{\frac{2}{3} \left\{ (\dot{\epsilon}_x - \dot{\epsilon}_v)^2 + (\dot{\epsilon}_y - \dot{\epsilon}_v)^2 + (\dot{\epsilon}_z - \dot{\epsilon}_v)^2 + \dot{\epsilon}_{yy}^2 + \dot{\epsilon}_{zz}^2 + \dot{\epsilon}_{yz}^2 \right\}}$ . Parameter 'repow' is a user-specified input parameter, defined as the power that increases fracture energy with rate effects, 'repow' is equal to 1 [52]. Additionally, effective fluidity coefficient  $\eta$  is internally calculated as the following:

$$\left\{ \begin{array}{l} \text{if the pressure is tensile } (J_1 < 0) \quad \eta = \eta_s + trans(\eta_t - \eta_s) \quad trans = \left( \frac{-J_1}{\sqrt{3J_2}} \right)^{pwrt} \\ \text{if the pressure is compressive } (J_1 \geq 0) \quad \eta = \eta_s + trans(\eta_c - \eta_s) \quad trans = \left( \frac{J_1}{\sqrt{3J_2}} \right)^{pwrc} \end{array} \right. \quad \text{Eq. 3.2}$$

where,  $\eta_t = \frac{\eta_{0t}}{\dot{\epsilon}^{N_t}}$ ,  $\eta_c = \frac{\eta_{0c}}{\dot{\epsilon}^{N_c}}$ ,  $\eta_s = S_{rate} \eta_t$ , here,  $\eta_{0t}$  and  $N_t$  are using for fitting uniaxial tensile stress data,  $\eta_{0c}$  and  $N_c$  for fitting the uniaxial compressive stress data, and  $S_{rate}$  for fitting shear stress data,  $S_{rate}$  is equal to 1. According to [52], 'pwrt' is equal to 1, and 'pwrc' is equal to 5.

Two types of input options are offered, (1) \*MAT\_CSCM\_CONCRETE: this material is user-friendly; it can automatically generate default parameters requiring only simple key values including density of concrete, uniaxial compressive strength, aggregate size, and the unit system [54], [55], [56]. (2) \*MAT\_CSCM: this material can be specially defined by the user, which is beneficial to adjust parameters in appropriate range. Default parameters for \*MAT\_CSCM can be generated from the "d3hsp" file after running the model with \*MAT\_CSCM\_CONCRETE. The details of input cards for concrete and grout are shown in Figure 3.9~3.10.



```

*MAT_CSCM_CONCRETE_TITLE
Mat_Concrete
$#   mid      ro      nplot   incre   irate   erode   recov   itretrc
      42.44000E-6      1      0.0      1      1.1     10.0      0
$#   pred
      0.0
$#   fpc      dagg   units
      0.042    19.0     0

```

(a) Concrete

```

*MAT_CSCM_CONCRETE_TITLE
Mat_Grout
$#   mid      ro      nplot   incre   irate   erode   recov   itretrc
      22.00000E-6      1      0.0      1      1.1     10.0      0
$#   pred
      0.0
$#   fpc      dagg   units
      0.082    0.1     0

```

(b) Grout

**Figure 3.9** Input cards for \*MAT\_CSCM\_CONCRETE (units: mm-kg-ms-GPa)

```

*MAT_CSCM_TITLE
Mat_Concrete
$# mid ro nplot incre irate erode recov itretrc
    42.44000E-6 1 0.0 1 1.1 10.0 0
$# pred
    0.0
$# g k alpha theta lamda beta nh ch
    1.28E+01 1.404E+01 1.570E-02 3.362E-01 1.051E-02 1.929E+01 1.0 0.0
$# alpha1 theta1 lamda1 beta1 alpha2 theta2 lamda2 beta2
    7.47E-01 7.827E-01 1.700E-01 5.603E+01 6.600E-01 9.439E-01 1.600E-01 5.603E+01
$# r xd w d1 d2
    5.0 9.724E-02 5.000E-02 2.500E-01 3.492E-01
$# b 0.8* gfc d 0.4* gft 0.4* gfs pwrc pwrt pmod
    1.00E+02 8.654E-03 1.000E-01 8.654E-05 8.654E-05 5.0 1.0 0.0
$# 4* eta0c nc 4* etaot nt overc overt srate rep0w
    6.75E-04 7.800E-01 2.713E-03 4.800E-01 2.805E-02 2.805E-02 1.0 1.0

```

(a) Concrete

```

*MAT_CSCM_TITLE
Mat_Grout
$# mid ro nplot incre irate erode recov itretrc
    22.00000E-06 1 0.0 1 1.1 10.0 0
$# pred
    0.0
$# g k alpha theta lamda beta nh ch
    1.60E+01 1.755E+01 1.344E-02 4.960E-01 1.051E-02 1.929E+01 1.0 0.0
$# alpha1 theta1 lamda1 beta1 alpha2 theta2 lamda2 beta2
    7.47E-01 -1.25E+00 1.700E-01 -3.39E+01 6.600E-01 -1.54E+00 1.600E-01 -3.39E+01
$# r xd w d1 d2
    5.0 1.378E-01 5.000E-02 2.500E-01 3.492E-01
$# b gfc d gft gfs pwrc pwrt pmod
    1.00E+02 8.462E-03 1.000E-01 8.462E-05 8.462E-05 5.0 1.0 0.0
$# eta0c nc etaot nt overc overt srate rep0w
    3.95E-03 7.800E-01 5.561E-03 4.800E-01 7.730E-02 7.730E-02 1.0 1.0

```

(b) Grout

**Figure 3.10** Default and update parameters for \*MAT\_CSCM (units: mm-kg-ms-GPa)

To ensure suitability of the default concrete material model for impact scenarios, specimen GSS-F was subjected to an impact velocity of 2 in./s, which was chosen as the study case. The force-time history curve obtained was compared with test observations and presented in Figure 3.11 (a), revealing a 22.7% discrepancy in the initial peak value. Following the calibrated methodology outlined in [51], several adjustments were made to the default model parameters, resulting in the following calibrated factors:  $G_{fc} = 0.8$ ,  $G_{fs} = 0.4$ , and  $G_{ft} = 0.4$ , with  $\eta_{0c}$  and  $\eta_{0t}$  both set to 4. These modifications not only reduced the discrepancy of the first peak to 1.1% but also extended the duration of the second peak impact, as shown in Figure 3.11 (b). Notably, major cracking was observed in the concrete, while the grout components did not require calibration.

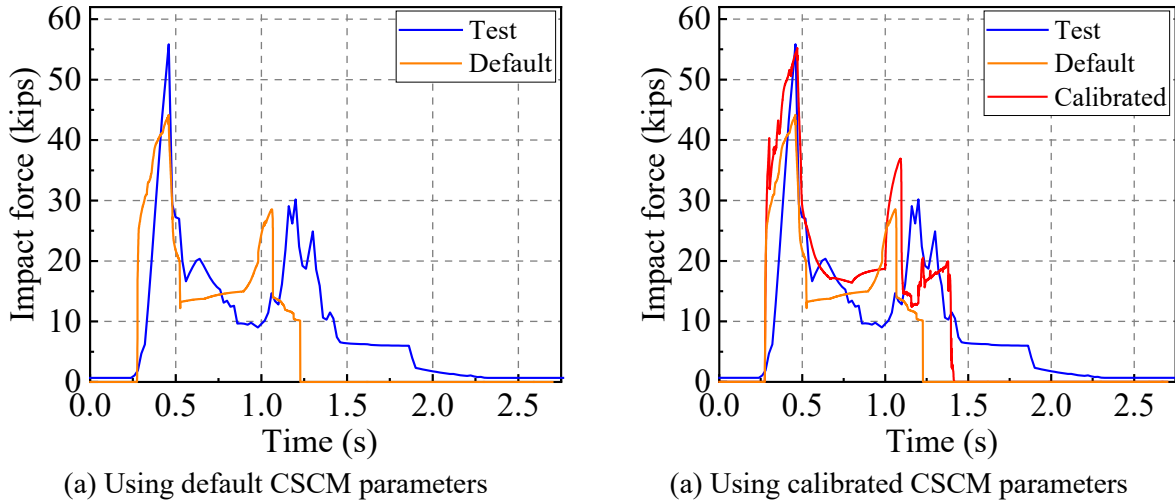


Figure 3.11 Calibration study of CSCM Material

### 3.5.2 Material Model Rebar

The constitutive relation of the longitudinal bars and GSS were described by the kinematic elastic–plastic material model \*MAT\_PLASTIC\_KINEMATIC, which can successfully model the dynamic behaviors of the steel material under impact. The Cowper-Symonds equation was used to describe the dynamic increase factor (DIF) of the structural steel [50], [51], [54], [57]:

$$DIF = \sigma_d / \sigma_s = (1 + \dot{\epsilon} / C)^{1/P} \quad \text{Eq. 3.3}$$

where,  $\sigma_d$  is the dynamic yield stress,  $\sigma_s$  is the static yield stress,  $\dot{\epsilon}$  is the effective strain rate;  $C$  and  $P$  are the parameters of the material’s strain rate, valuing 40.5 and 5.0 respectively.

*MAT_PLASTIC_KINEMATIC_TITLE							
Mat_Rebar							
\$#	mid	ro	e	pr	sigy	etan	beta
	17.85000E-6		206.0	0.3	0.415	2.1	0.0
\$#	src	srp	fs	vp			
	40.5	5.0	0.25	0.0			

(a) Rebar

*MAT_PLASTIC_KINEMATIC_TITLE							
Mat_Coupler							
\$#	mid	ro	e	pr	sigy	etan	beta
	27.85000E-6		173.0	0.3	0.415	1.73	0.0
\$#	src	srp	fs	vp			
	40.5	5.0	0.25	0.0			

(b) Coupler

Figure 3.12 Input cards for \*MAT\_PLASTIC\_KINEMATIC (units: mm-kg-ms-GPa)

### 3.5.3 Material Model for Accessory Steels

Additionally, the accessory steels in the model were assumed to be rigid, using the \*MAT\_RIGID material to save analysis time. Even though this material doesn't deform under loading, to make sure it has realistic mass, and inertial properties, density, Young's modulus, and Poisson ratio were taken from standard steel reinforcing material properties. The details of the input card for accessory steels are represented as Figure 3.13.

*MAT_RIGID_TITLE								
Mat_Accessory steels								
\$#	mid	ro	e	pr	n	couple	m	alias
	57.85000E-6		200.0	0.3	0.0	0.0	0.0	

Figure 3.13 Input cards for \*MAT\_RIGID (units: mm-kg-ms-GPa)

### 3.6 Mesh Sensitivity Study

To optimize the balance between computational efficiency and accuracy in FE models, the characteristics of the mesh were crucial to the numerical results. First, to ensure efficient force transfer, the mesh layers at the contact interfaces of two parts were made consistent, as depicted in the section view B-B in Figure 3.1 (a). Second, mesh size is particularly critical for nonlinear analysis, where a larger mesh may result in an unusual distribution of damage. Drawing on the recommendations from recent research articles [58], [59], [60], [61], [62], which examine the impact response of concrete structures modeled in LS-DYNA, mesh sizes of 10 mm, 25 mm, and 50 mm are highly recommended.

Mesh sensitivity has been analyzed using three sizes: 0.5 in. (12.7 mm), 1 in. (25.4 mm), and 2 in. (50.8 mm). To ensure the appropriateness of the mesh size for impact scenarios, specimen GSS-F was subjected to an impact velocity of 2 in./s. The corresponding impact force time history curves are illustrated in Figure 3.14.

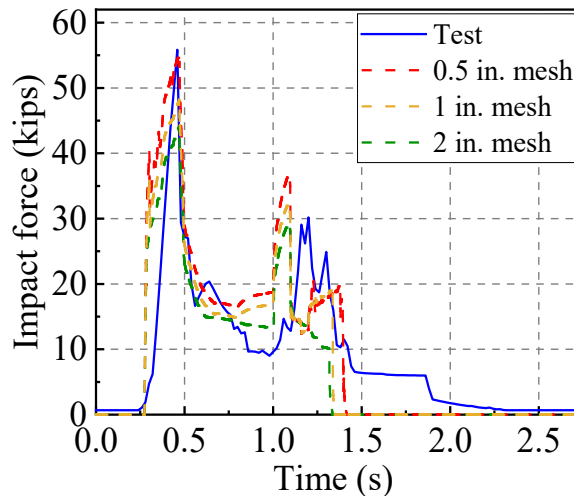


Figure 3.14 Mesh sensitivity analysis

In Figure 3.14, three models with various mesh sizes have two peak forces. Compared with first peak value with test result, 1.1% difference was found in the model with 0.5-inch mesh, 13.7% difference was found in the model with 1-inch mesh, while a 20.9% difference was found in the model with 2-inch mesh. Meanwhile, 1-inch mesh and 2-inch mesh do not present enough duration time of second peak stage. Based on this analysis, in this study's model, an average mesh size of 0.5 inches (12.7 mm) was chosen for the concrete, GSS and the grout in the GSS. The mesh size of steel reinforcement was also 0.5 inches. In addition, to make sure perfect contact between specimen and accessory steels, the meshes of constraint and loading steels maintain the same size of 0.5 inches with the concrete. In total, the model had 28,187 elements and 34,326 nodes.

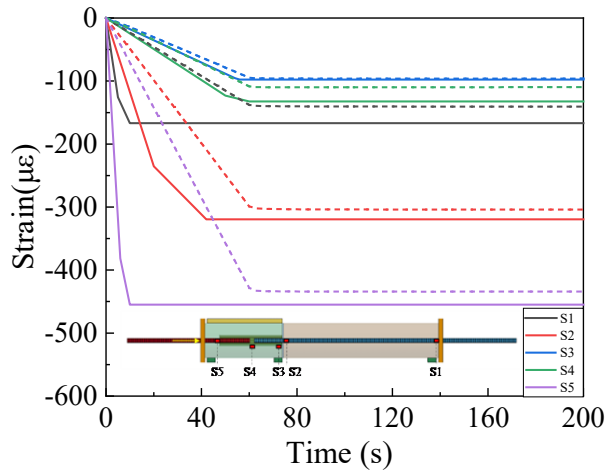
### **3.7 Verification of Simulated Results**

To ensure the adjusted FE modeling method is feasible for predicting structural behavior under both static and dynamic loading scenarios, this section compares predictions from the numerical models with experimental results. Strain-time history curves were compared to verify effective load transfer and stress distribution in the elastic phase during static tests. Additionally, impact force-time history and failure modes were analyzed to accurately simulate the dynamic behavior and failure mechanisms of precast concrete with GSSs under impact loading. Furthermore, the validated models were capable of revealing non-visible damage within the coupler, which could not be directly observed in experimental tests.

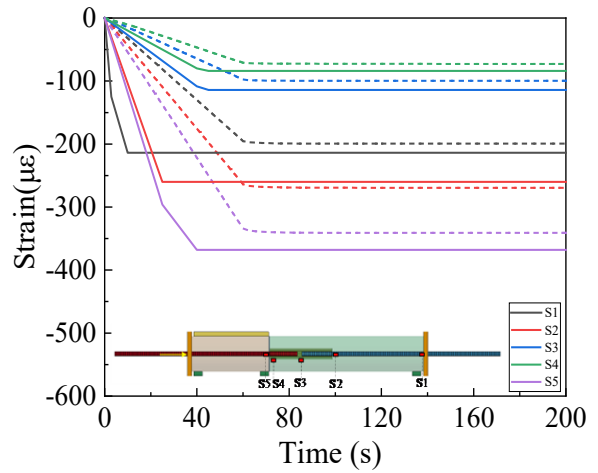
#### **3.7.1 Strain Response During the Static Test**

Figures 3.15-3.16 compared the strain-time history curves obtained from the experiment's results with curves predicted by the developed FE models. Good agreements are reached between the experimental results and the FE data. Figure 3.17 shows the ultimate compressive strains from FE simulations were mostly 2% to 17% lower than the experimental results. Additionally, an error of 1% to 20% was observed for the maximum loading, except the S5 data of GSS-F with a 62% difference. This is because it is difficult to provide perfect restraints for the specimens in the test, leading to more deformation than the numerical model with ideal boundary conditions.

In general, the FE model accurately captured the deformation behavior during both the compression and lateral loading stages, and it provided a well stress distribution in the elastic phase. The model also demonstrated the effectiveness of the bond-slip law within the coupler, facilitating efficient load transfer through the coupler. Consequently, the developed FE modeling approach is suitable for further dynamic validation studies.

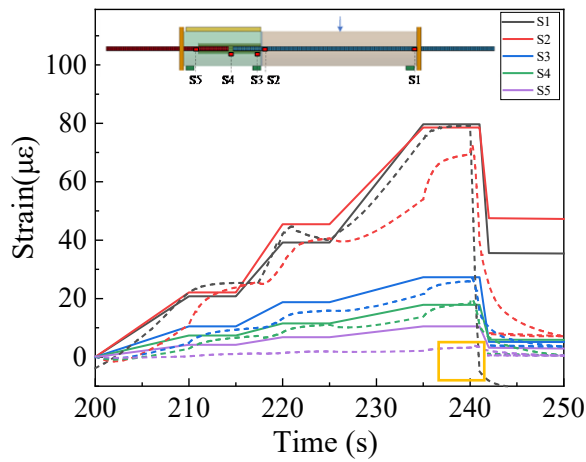


(a) GSS-F

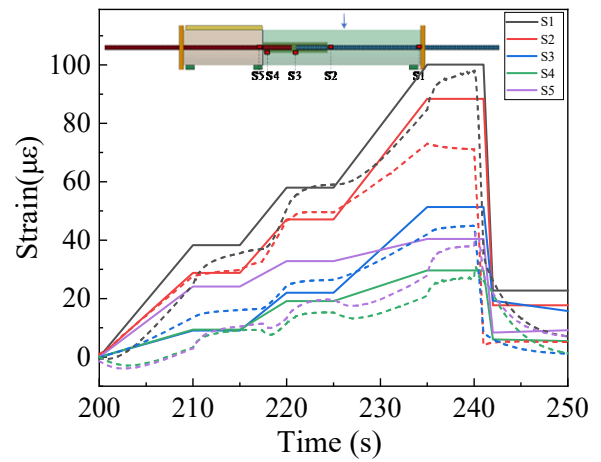


(b) GSS-C

**Figure 3.15** Compressive strain-time history (solid lines: test data; short dash lines: FE results)

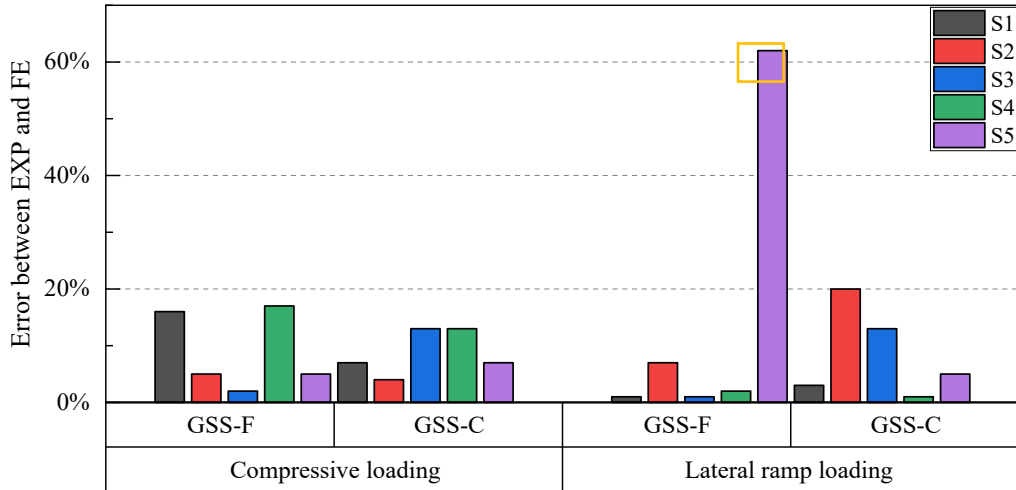


(a) GSS-F



(b) GSS-C

**Figure 3.16** Strain-time history (solid lines: test data; short dash lines: FE results)



**Figure 3.17** Error of maximum strain between the experiments and FE models

### 3.7.2 Dynamic Response During the Impact Test

Figure 3.18 compares the numerically predicted and experimentally measured impact force-time histories for four specimens. The numerical results also exhibit three distinct stages: the first peak impact stage, the second peak impact stage, and the unloading stage, mirroring observations from the tests. Differences between the FE models and the tests were calculated and marked as red percentages in Figure 3.18. It can be observed that the first peak impact events occurred at nearly the same time as in the tests, with the predicted values fitting well within the range of experimental results, showing errors from 0.7% to 1.65%. This demonstrates the models' ability to accurately capture the sudden impact load applied to the specimens.

During the second peak impact stage, the second peaks in the numerical models occurred earlier than in the tests, and the durations of the forces experienced were shorter than those in the tests. For most models (F1, F2, and C1), the second peak values are 8.13% to 32.25% higher than the test results, except for model C2, which had a second peak value 4.73% lower than the test result. This discrepancy may be attributed to overly rigid constraints in the models, which can increase contact loads and accelerate energy dissipation, resulting in a larger peak and a shorter impact duration. Specimen C2 differed from the others, as it exhibited limited concrete cracking and unique grout failure within the coupler. This indicated that more energy was dissipated by the GSS system rather than by the concrete, reducing the influence of concrete sides constraints in C2.

Overall, the FE models effectively predicted the dynamic behavior of precast concrete structures with GSSs under impact loading. The ability to capture key response characteristics, such as peak impact forces and duration, confirms the validity of the modeling approach.

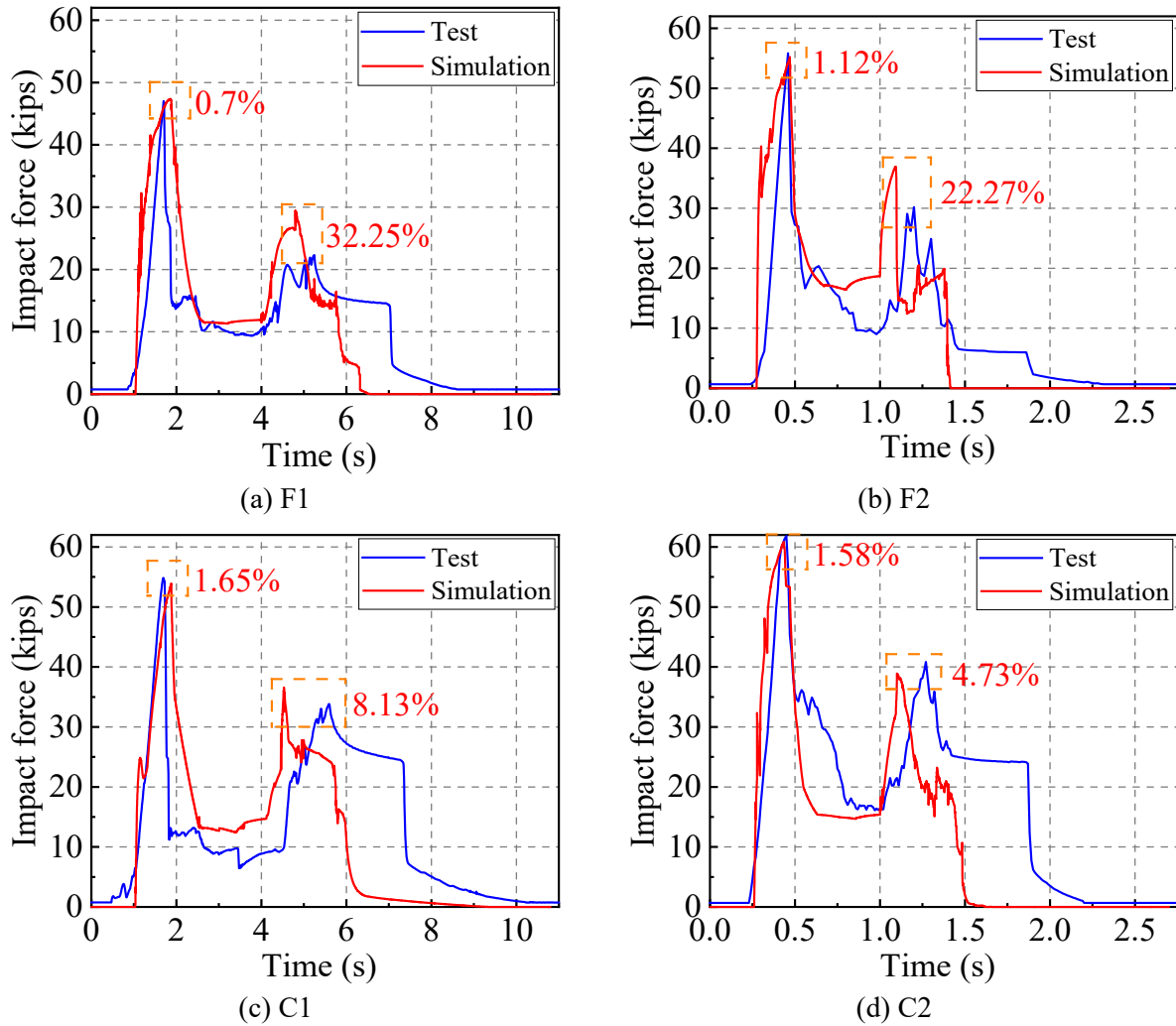


Figure 3.18 Comparison of impact force-time

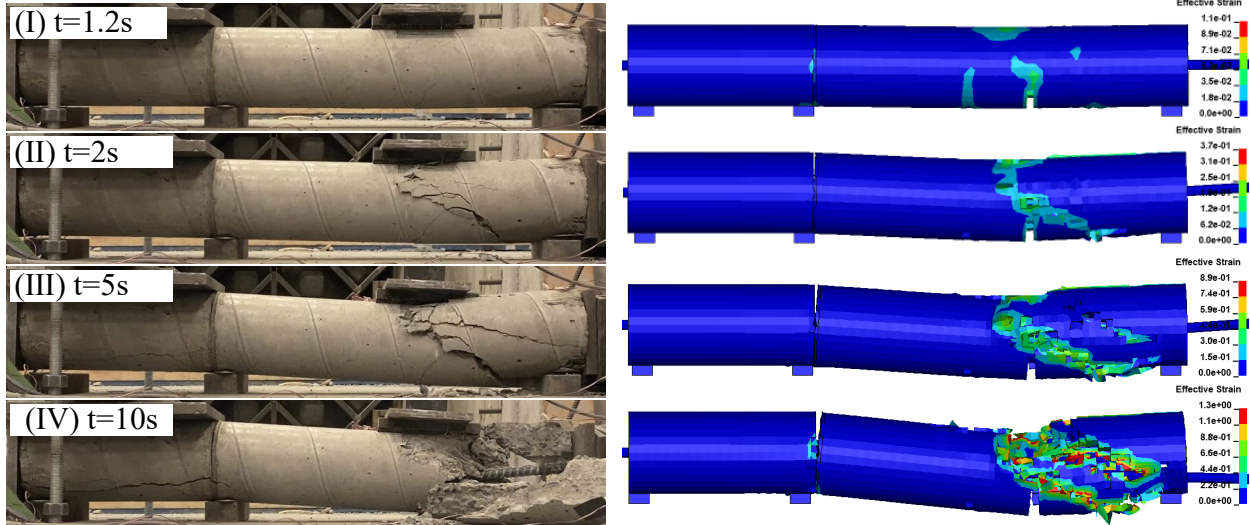
### 3.7.3 Failure Processes During the Impact Test

Figure 3.19 compares the numerical damage patterns and the failure processes recorded during impact tests. Generally, the crack development processes, and final failure modes of the FE models closely matched the experimental observations.

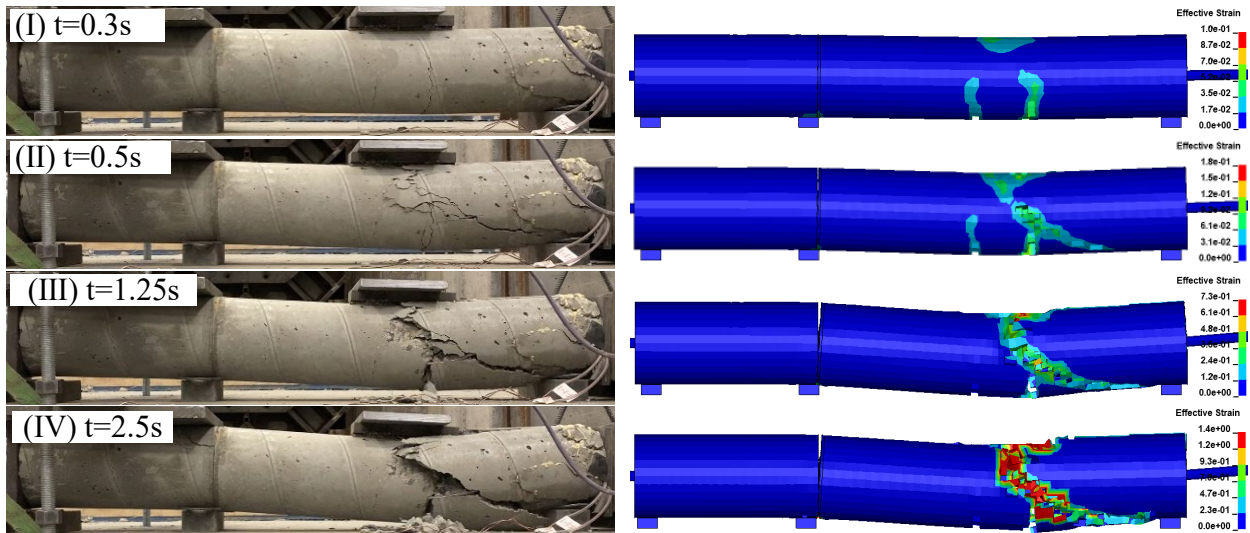
In model F1, flexural cracks initially generated on the bottom surface at mid-span. Then, one major shear crack propagated from the impact location to the edge of the right support under the column. Subsequently, another shear crack initiated from the same location as the first crack but terminated at the right surface of the concrete, 1.5 inches above the right support. Similarly, in model F2, initial flexural cracks occurred, but only one shear crack connecting the mid-span and right support was observed. This is because the faster impact did not allow sufficient time for cracks to propagate and develop extensively, leading to limited number but more severe condition of crack. Additionally, the strain rate effect in concrete was significantly higher with increased impact velocity.



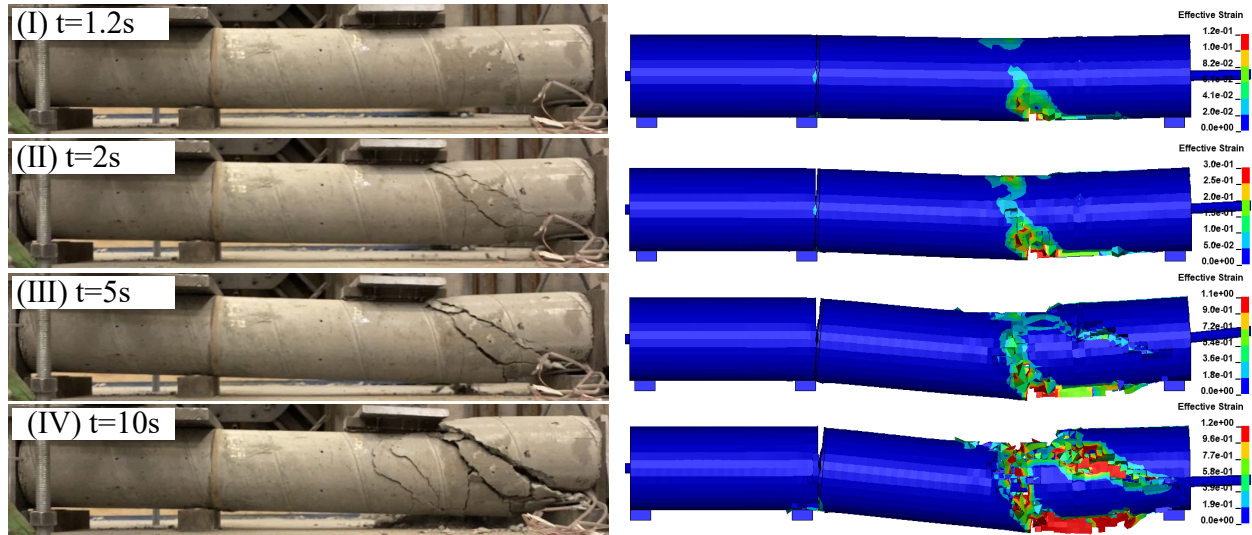
In model C1, it appears to have missed some small flexural cracks under the impact location; however, the model captured the initial flexural cracks, which then transitioned into shear behavior, combining flexural and shear effects into a single crack under the impact area. Another major shear crack was also observed. Model C2 exhibited a unique failure pattern, with a vertical crack at the column's mid-span. This pattern was attributed to non-visible failure in the grout within the coupler, which could not be observed during tests. The cause of this failure was a potential grouting defect.



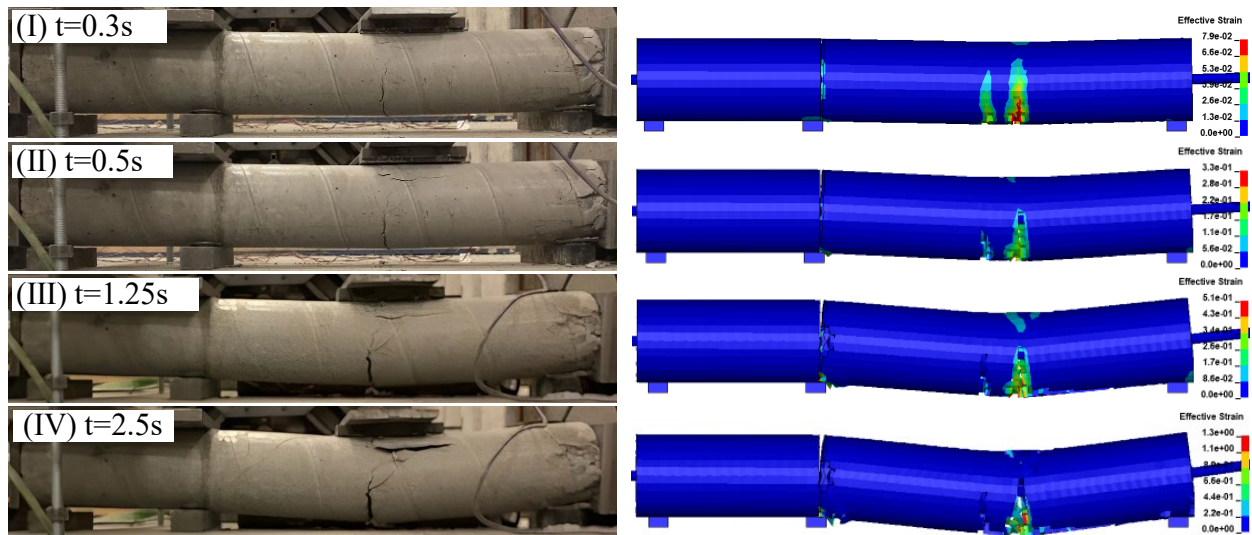
(a) F1



(b) F2



(c) C1



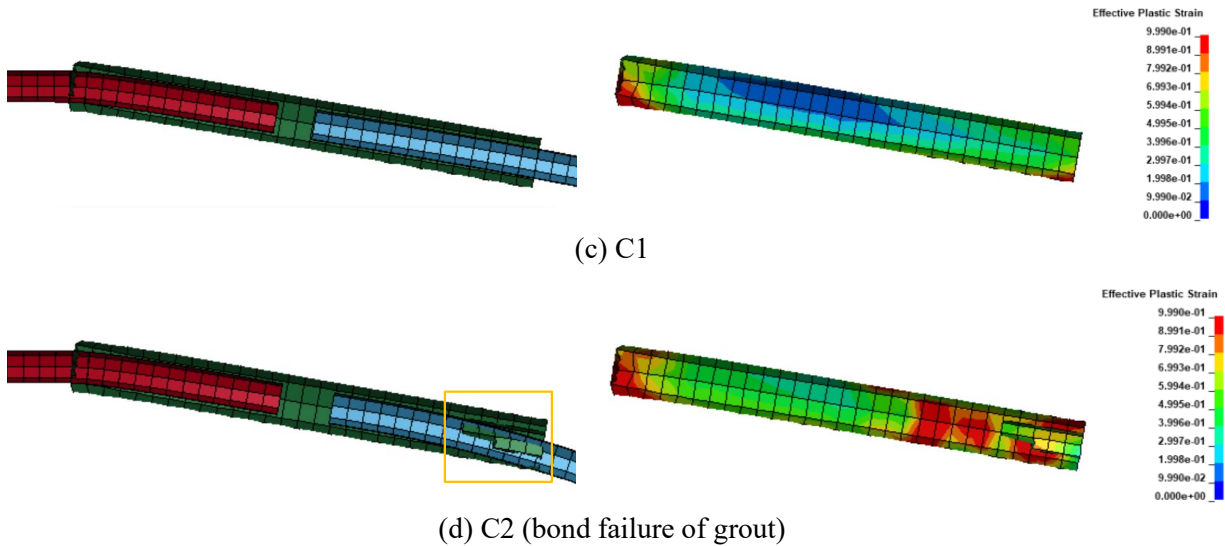
(d) C2

**Figure 3.19** Comparison of failure processes

To further understand the bond failure inside the coupler, Figure 3.20 presents section views of specimens GSS-C at the end of the impact. In model C1, no slip was observed, and the section views of the grout damage pattern also indicated healthy grout inside the coupler, suggesting good bond behavior of the grout during impact. However, higher plastic strains were present at both ends of the grout, where more stresses concentrate during high-velocity impacts.

In model C2, approximately one mesh size (0.5 inches or 12.7 mm) of the rebar was pulled out from the grout; a length of 2.5 inches (63.5 mm) of the rebar lost its bond with the grout. The section views of the damage pattern indicate a potential risk of bond failure in high plastic strain areas under more severe impacts.

Overall, the numerical model not only precisely predicted the development processes of cracks and final failure modes of the precast concrete structures but also effectively simulated the bond-slip mechanism between the grout and rebar, which was crucial for ensuring an accurate load transfer through GSS.



**Figure 3.20** Section views at the end of impacting (Left: Grout and rebars; Right: Grout damage)

### 3.8 Summary

This chapter introduces the calibration of parameters, including material properties, mesh size sensitivity, and the bond-slip law between rebar and surrounding materials. The FE models were validated against experimental results under both static and dynamic scenarios. Strain-time history curves were analyzed to verify effective load transfer and stress distribution during static tests. Additionally, impact force-time history and failure modes were examined to simulate the dynamic behavior and failure mechanisms of precast concrete with GSSs under impact loading.

The FE model effectively captured deformation behavior during both compression and lateral loading stages, providing accurate stress distribution in the elastic phase. It demonstrated the bond-slip law's effectiveness within the coupler, ensuring efficient load transfer. This validated the FE modeling approach for further dynamic studies.

The models accurately predicted the first peak impact events, aligning closely with experimental results and showing errors between 0.7% and 1.65%. This precision in capturing sudden impact loads confirmed the models' capability to simulate the dynamic behavior of precast concrete structures with GSSs. The ability to capture key response characteristics, such as peak impact forces and duration, further supported the modeling approach's validity.

Additionally, the numerical model accurately predicted crack development and final failure modes of precast concrete structures. It effectively simulated the bond-slip mechanism between grout and rebar, crucial for accurate load transfer through GSS. The validated models can also reveal non-visible damage within the coupler, which was not directly observable in experimental tests.

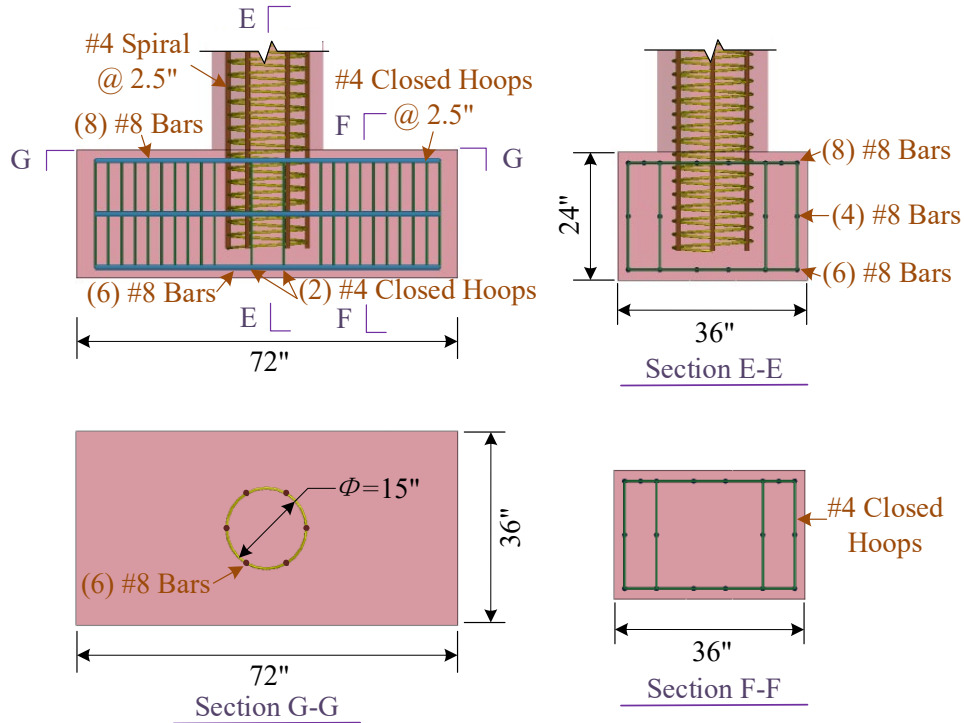
## **4. FE MODELS OF HALF-SCALE COLUMN UNDER SEISMIC LOAD**

To ensure suitability of the modeling techniques for simulating the seismic behavior of precast columns, a 3D finite element (FE) models of three half-scale columns in LS-DYNA were developed. This chapter provides a detailed description of the modeling techniques employed. The developed FE models were validated against experimental results from Pantelides et al. [2] through several key characteristics: strain-time history curves to verify load transfer, hysteresis curves, average skeleton curves, and the analysis of crack development and damage states at critical drift ratios for seismic response. The validation process showed good agreement between the FE analysis and experimental results in both the initial and pushover stages, confirming the accuracy and reliability of the FE models in capturing the seismic behavior of precast columns.

### **4.1 Geometry Information of Half-scale Columns**

In Pantelides et al., the column-footing joint specimens were designed following the typical prototype highway bridges found in Utah [2]. These test specimens were constructed as half-scale models to ensure the manageable testing. Each column stood 8 feet 6 inches tall, with a 21-inch square cross-section at the top head, which measured 1 foot 6 inches in height, and a 7-foot-tall body featuring a 21-inch octagonal cross-section. The steel reinforcement within each column comprised six No. 8 longitudinal bars arranged in a circular pattern with a 15-inch diameter, and a No. 4 spiral reinforcement with 2.5-inch spacing. The reinforcement design achieved longitudinal and volumetric transverse reinforcement ratios of 1.3% and 1.9%, respectively.

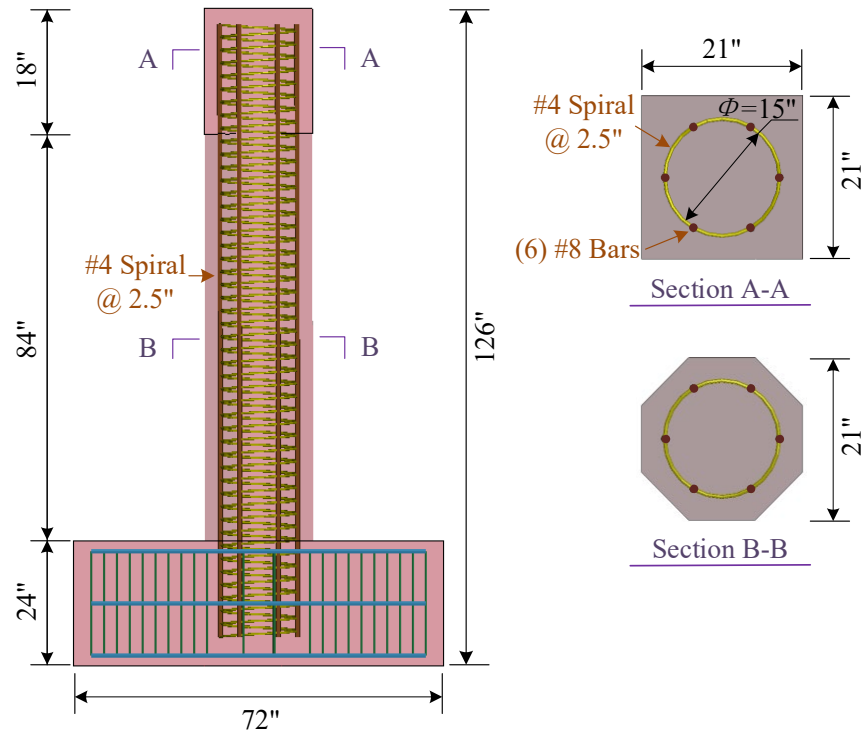
Figure 4.1 provides a summary of the design details for the joint regions of the column-footing specimens. The dimensions of the precast footing were six feet in length, three feet in width, and two feet in depth. It incorporated a total of 18 No. 8 longitudinal bars, which were enclosed by No. 4 double hoops with 2.5-inch spacing. Notably, there were two No. 4 double hoops positioned in the middle of the footing, right below the column, for additional reinforcement.



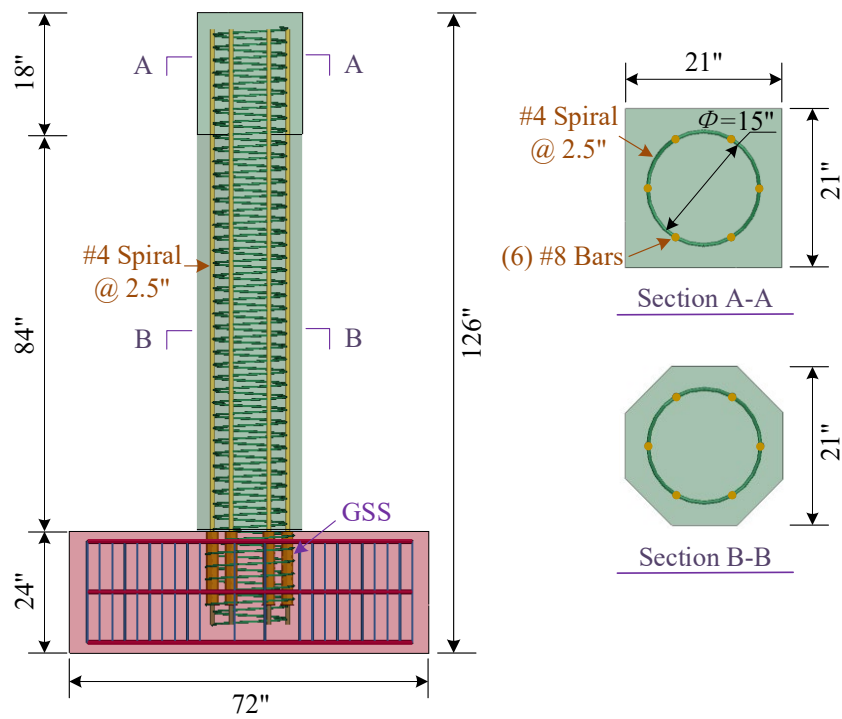
**Figure 4.1** General joint design details of column-footing (unit: inch)

Three categories of pier-to-footing joints were constructed: **(a) Cast-in-Place (CIP) Specimen:** This category involves monolithic casting construction without any GSS connectors to splice the reinforcement. The spiral reinforcement also did not have any splices. This specimen served as the control specimen. **(b) GSS-F Specimen:** In this category, the footing part and the 8 feet 6 inches tall column part inches were cast separately, each containing six No. 8 longitudinal rebars. The rebars extended seven inches from the bottom of the column, while six connectors are embedded at the top of the footing and bonded with the longitudinal rebars within the footing. The two parts were connected by inserting the protruding dowel bars into the couplers and filling them with grout. Additionally, a 0.25-inch grout layer was applied at the column-to-footing interface. **(c) GSS-C Specimen:** Similar to the GSS-F, this category involved separately casting the footing and column. However, in this case, the column had six connectors embedded at its bottom, and the footing had six No. 8 longitudinal rebars extending seven inches from its top. The connection was achieved by filling the connectors with grout. A 0.25-inch grout layer was also added at the column-to-footing interface. The general dimensions and details of these columns are illustrated in Figure 4.2.

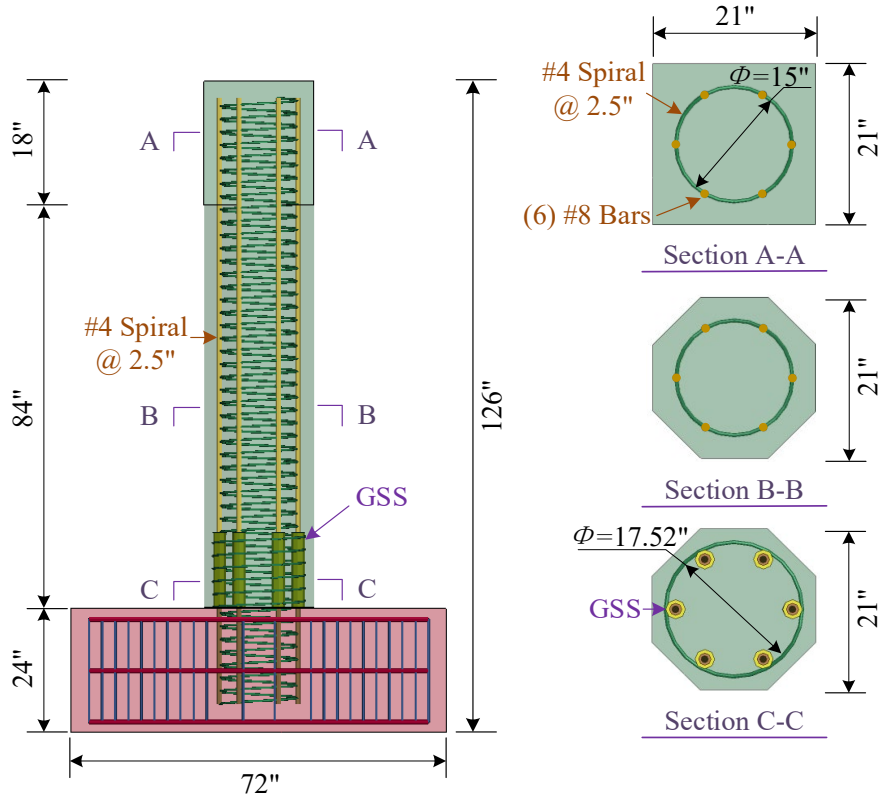




(a) Dimensions of CIP



(b) Dimensions of GSS-F



(c) Dimensions of GSS-C

Figure 4.2 Geometry information of columns (unit: inch)

## 4.2 Modeling Techniques of Half-scale Columns

### 4.2.1 General Description of FE Models

Using the software LS-DYNA, three 3D models were developed to validate the structural seismic behavior under cyclic loading scenarios, as depicted in Figure 4.3. In Figure 4.3 (a), CIP specimen includes a monolithic concrete construction with two separate rebar cages. The rebar cage within the column consists of six No. 8 longitudinal bars, each measuring 117.5 inches in length, and a No. 4 spiral reinforcement with 2.5-inch spacing. The rebar cage in the footing contains a total of 18 No. 8 longitudinal bars, enclosed by 22 No. 4 double hoops.

The loading system in the model was simplified, featuring a compressive loading plate located at the top of the column and two pushover loading plates positioned at the mid-height of the square cross-section part of the column. The constraint system included a ground below the bottom of the footing and two anchor blocks positioned on the upper surface of the footing. For simplicity, all steel components in the loading and constraint systems are referred to as "accessory steels" in the following sections.

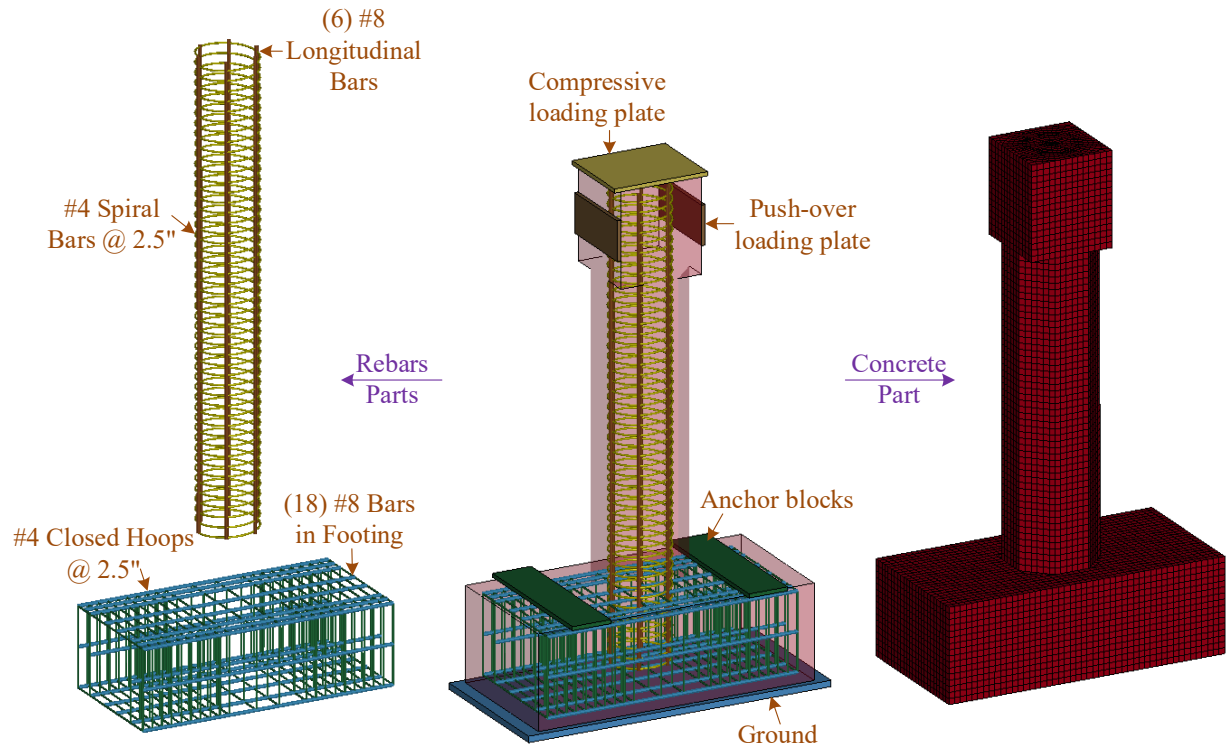
In the CIP specimen, the concrete and accessory steels were all modeled using SOLID\_164 elements, while the reinforcements were modeled with BEAM\_161 elements. Based on the mesh sensitivity study in Section 3.6 and considering computational efficiency, the average mesh sizes for the concrete and rebars were set to 1 inch (25.4 mm). No bond-slip was considered between the reinforcements and the concrete. The model consisted of a total of 54,120 elements and 65,888 nodes.

In Figure 4.3 (b) and (c), the GSS-F and GSS-C specimens had more complex components compared to the CIP specimen. Rather than a single monolithic concrete construction, these specimens consisted of three components: concrete of the pier, concrete of the footing, and a 0.25-inch grout bed at the column-to-footing interface. Both specimens utilized the same accessory steels, which were applied at the same locations as in the CIP specimen.

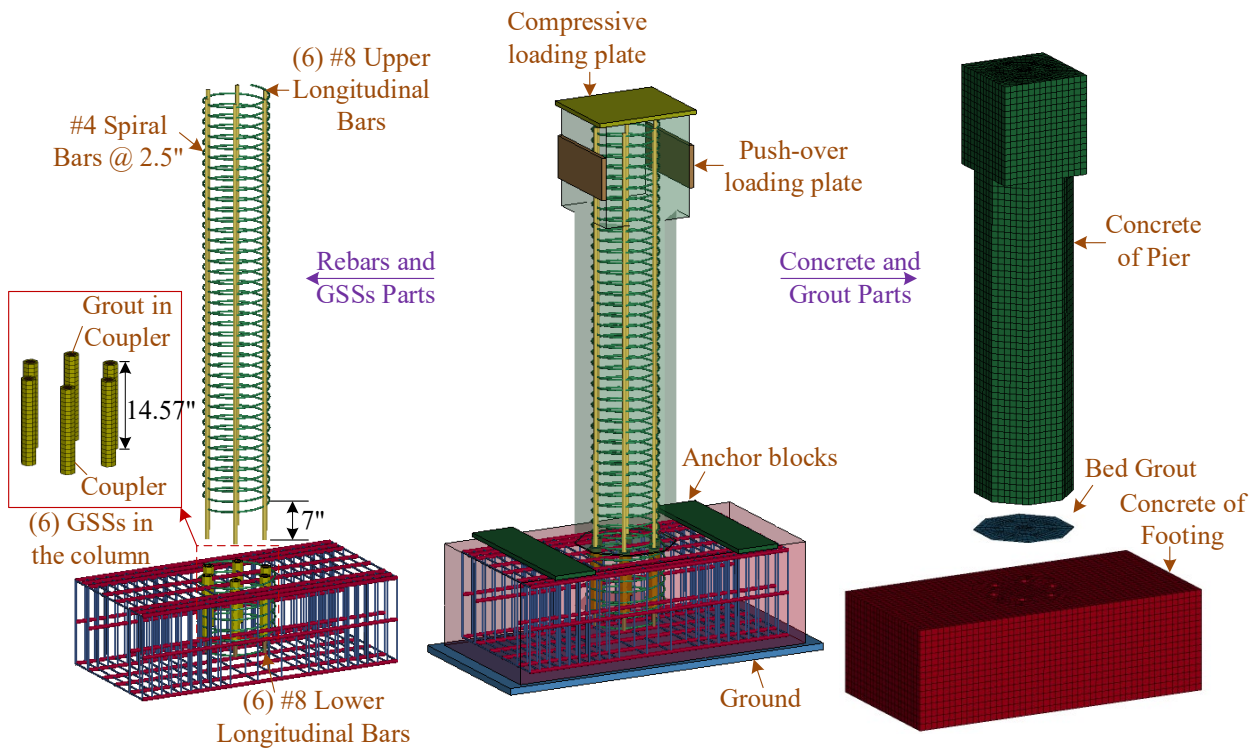
The GSS-F and GSS-C specimens had different arrangements for the rebar. For the GSS-F specimen, the six No. 8 longitudinal bars were spliced into two lengths: the upper part, which was 106 inches long, and the lower part, which was 10.43 inches long. These two sections of rebar were connected using six grouted couplers located at the top of the footing. For modeling simplicity, the diameter of the coupler was chosen based on the average diameter of its narrow and wide ends. The coupler had an outer diameter of 2.52 inches, an inner diameter of 1.6 inches, and a length of 14.57 inches. For the GSS-C specimen, the six No. 8 longitudinal bars were also spliced into two lengths: the upper section was 90.68 inches long, and the lower section was 25.75 inches long. These two sections of rebar were connected using six grouted couplers at the bottom of the column. Additionally, three pieces of No. 4 spiral reinforcement were used: two parts were bonded with the longitudinal bars and had a 15-inch diameter, while one part was bonded with the coupler and had a 17.52-inch diameter.

In the precast column models with GSSs, the concrete, grout, GSS, and accessory steel components were modeled using SOLID\_164 elements. The reinforcements were represented by BEAM\_161 elements. Consistent with the mesh sensitivity study in Section 3.6, the mesh sizes for the couplers and the grout within the couplers were maintained at 0.5 inches (12.7 mm). For computational efficiency, the average mesh sizes for the concrete and rebars were set to 1 inch (25.4 mm). To ensure effective contact, the contact surfaces utilized the same mesh size. No bond-slip was considered between the reinforcements and the concrete, except for the rebars in the couplers, which were allowed to slip using \*CONSTRAINED\_BEAM\_IN\_SOLID with the bond-slip law described in Section 3.4. This model comprised a total of 55,137 elements and 68,154 nodes.

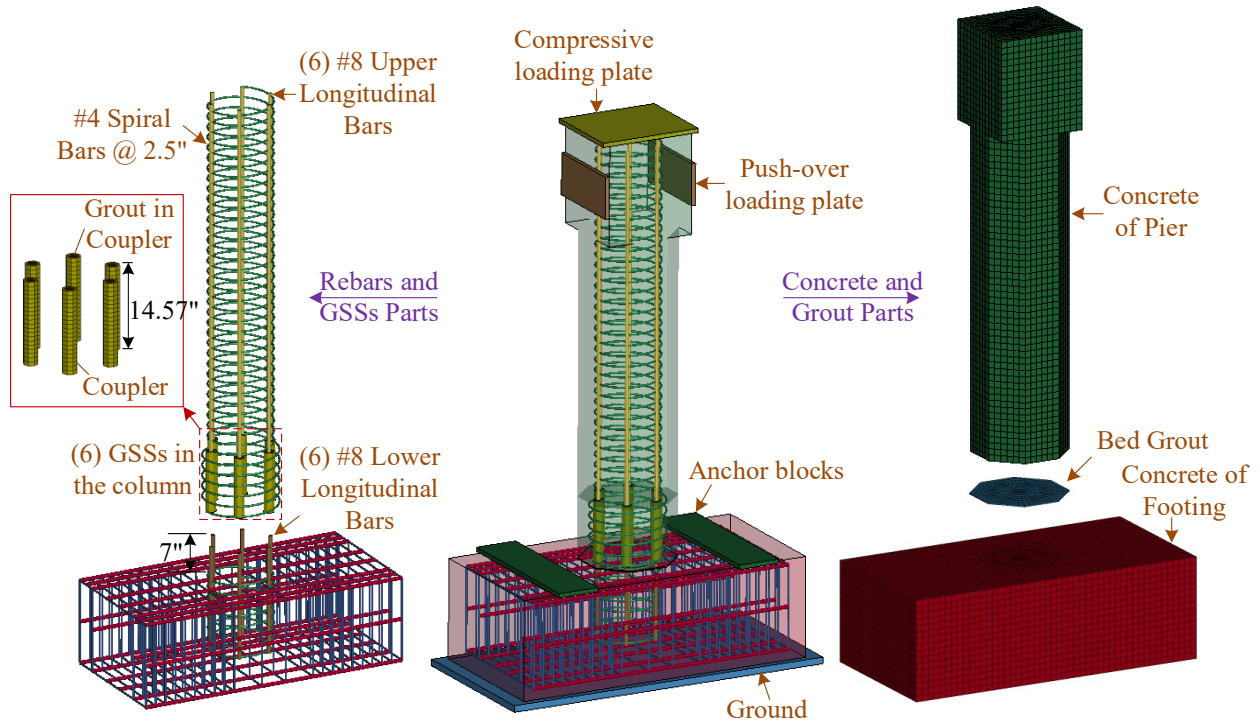




(a) Details of CIP



(b) Details of GSS-F



(c) Details of GSS-C

**Figure 4.3** Description of FE models (unit: inch)

In the preceding Section 3.5, the material models were introduced and calibrated for this study. Utilizing the insights from that Section, the concrete and grout materials were modeled using \*MAT\_CSCM (Continuous Surface Cap Model) to predict both elastic deformation and failure of the materials. Specifically, the average compressive strength values used were 6 ksi (0.041 GPa) for concrete and 14 ksi (0.096 GPa) for grout, as measured on the test day [2]. The remaining parameters were derived from the calibration results presented in Section 3.5.

All reinforcements and couplers were described by the kinematic elastic-plastic material model \*MAT\_PLASTIC\_KINEMATIC, which effectively modeled the dynamic behaviors of steel materials. To enhance computational efficiency, the accessory steels in the model were assumed to be rigid and employed the \*MAT\_RIGID material model. The specific material parameters utilized in the finite element models are detailed in Table 4.1.

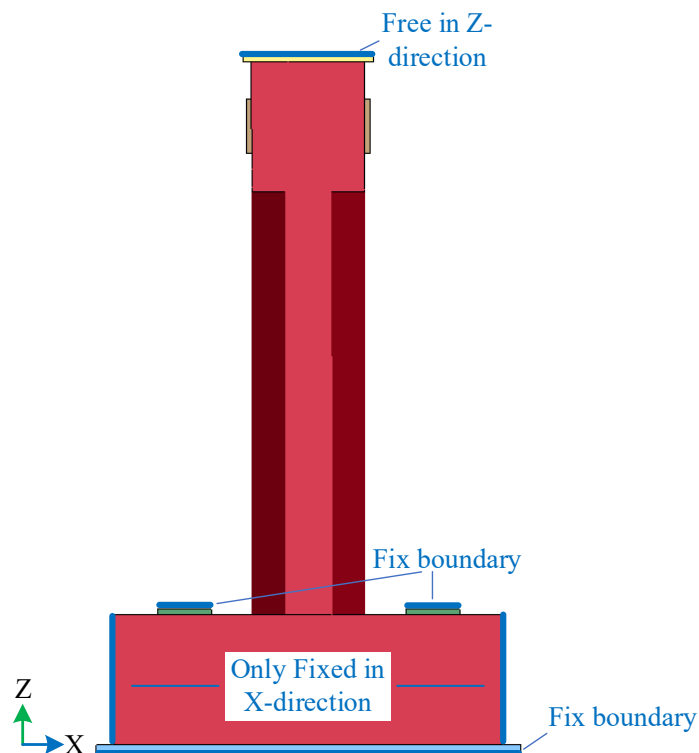
**Table 4.1** Material parameters in FE models

Parts	LS-DYNA models	Parameters	Magnitudes
Concrete	*MAT_CSCM	Mass density	2.44E-6 kg/mm <sup>3</sup>
		Unconfined compression strength	0.041 GPa
		Fracture energy in uniaxial stress, <i>GFC</i>	6.923E-3 GPa*mm
		Fracture energy in uniaxial tension, <i>GFT</i>	3.462E-5 GPa*mm
		Fracture energy in pure shear stress, <i>GFS</i>	3.462E-5 GPa*mm
		Rate effects parameter for uniaxial compressive stress, <i>ETA0C</i>	2.7E-3
		Rate effects parameter for uniaxial tensile stress, <i>ETAOT</i>	1.085E-2
		Grout	*MAT_CSCM
Unconfined compression strength	0.096 GPa		
Fracture energy in uniaxial stress, <i>GFC</i>	8.462E-3 GPa*mm		
Fracture energy in uniaxial tension, <i>GFT</i>	8.462E-5 GPa*mm		
Fracture energy in pure shear stress, <i>GFS</i>	8.462E-5 GPa*mm		
Rate effects parameter for uniaxial compressive stress, <i>ETA0C</i>	3.95E-3		
Rate effects parameter for uniaxial tensile stress, <i>ETAOT</i>	5.561E-3		
Rebars	*MAT_PLASTIC_KINEMATIC		
		Young's modulus	206 GPa
		Poisson's ratio	0.3
		Yield stress	0.415 GPa
		Tangent modulus	2.1 GPa
		Strain rate parameter, <i>C</i>	40.5
		Strain rate parameter, <i>P</i>	5.0
		Failure strain for eroding elements	0.25
Coupler	*MAT_PLASTIC_KINEMATIC	Mass density	7.85E-6 kg/mm <sup>3</sup>
		Young's modulus	173 GPa
		Poisson's ratio	0.3
		Yield stress	0.415 GPa
		Tangent modulus	1.73 GPa
		Strain rate parameter, <i>C</i>	40.5
		Strain rate parameter, <i>P</i>	5.0
		Failure strain for eroding elements	0.25
Accessory steels	*MAT_RIGID	Mass density	7.85E-6 kg/mm <sup>3</sup>
		Young's modulus	200 GPa
		Poisson's ratio	0.3

## 4.2.2 Contact and Boundary Conditions

To replicate the experimental boundary conditions of the specimen, several constraints were applied using the keyword `*BOUNDARY_SPC_SET`. All nodes at the bottom of the ground and the top of the anchor blocks were fully constrained in three translational degrees of freedom. To simulate constraints on the footing, nodes on both sides of the footing were restrained in the lateral cyclic loading direction (X direction). Additionally, the top-side nodes of the compressive loading plate were restrained in the X and Y directions while being allowed to move freely in the loading direction (Z direction), as illustrated in Figure 4.4.

To accurately capture interactions within the complex model, precise contact conditions were established in the software. The `*CONTACT_AUTOMATIC_SURFACE_TO_SURFACE` model was used to describe interactions between the specimens and the accessory steels, with a static friction coefficient of 0.2 and a dynamic friction coefficient of 0.15 [44]. For the bed grout and precast concrete interface, hard contact was used for normal behavior, while penalty friction was applied for tangential behavior. The joint contact utilized a Coulomb friction model `*CONTACT_AUTOMATIC_SURFACE_TO_SURFACE` with a friction coefficient of 0.75 [48]. The bond between the grouted sleeves and the surrounding concrete was modeled as frictionless due to the sleeves' smooth outer surface, using `*CONTACT_AUTOMATIC_SURFACE_TO_SURFACE` with default parameters. [46]. During testing, the GSS exhibited strong connection performance, with no observed slip between the coupler and the inner grout. Therefore, a tied bond was implemented between the coupler and the internal grouting material using `*CONTACT_TIED_SURFACE_TO_SURFACE` with default parameters.



**Figure 4.4** Boundary conditions

**Table 4.2** Contact setting key parameters in LS-DYNA

*CONTACT keywords	Slave	Master	FS	FD
AUTOMATIC_SURFACE _TO_SURFACE	Concrete	Compressive loading plate	0.2	0.15
	Concrete	Anchor blocks	0.2	0.15
	Concrete	Ground	0.2	0.15
	Coupler	Concrete	-	-
	Bed grout	Concrete	0.75	0.75
	Concrete	Pushover loading plate	0.2	0.15
TIED_SURFACE _TO_SURFACE	Grout in coupler	Coupler	-	-

Notes: In this table, FS is presented as static coefficient of friction, and FD is presented as dynamic coefficient of friction.

### 4.2.3 Loading Procedures

In LS-DYNA, the RESTART analysis mode was utilized to effectively manage the loading sequence following the initialization of gravity and precompression forces. This approach enabled the application of cyclic quasi-static loading to study the seismic behavior of the columns, as illustrated in Figure 4.5. The analysis consisted of two stages:

(1) Stress initialization stage: To establish the initial stress state, the self-weight of the structure was applied using \*LOAD\_BODY\_Y with an acceleration curve. An axial prestressing load equivalent to 6% of the column's axial capacity [2], amounting to 137.59 kips, was applied using \*LOAD\_RIGID\_BODY to simulate the typical gravity load in a bridge column. Once static equilibrium was achieved, the state of the structure was saved for subsequent analysis.

(2) Lateral cyclic loading stage: After the stress initialization stage, a pushover loading plate was employed to control displacement using \*BOUNDARY\_PRESCRIBED\_MOTION\_RIGID, positioned eight feet above the column base. The cyclic loading protocol applied displacement control, executing two cycles for each drift ratio ranging from 0.5% to 10%. Initially, the displacement rate was set at 1.2 in./min until the three-inch drift ratio was reached, after which the rate was increased to 4 in./min and maintained at this speed for the remainder of the test [2].

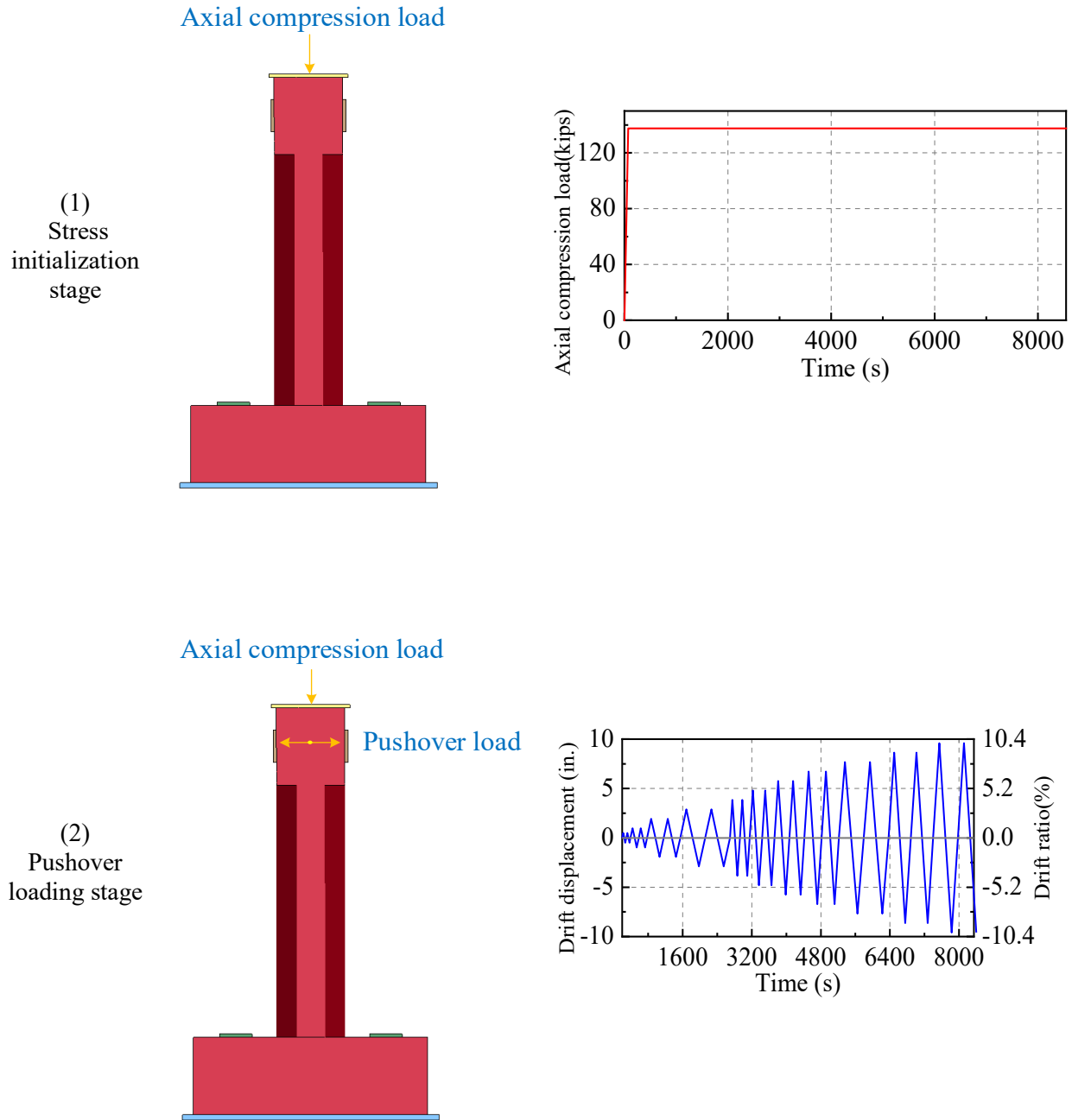


Figure 4.5 Loading stage description

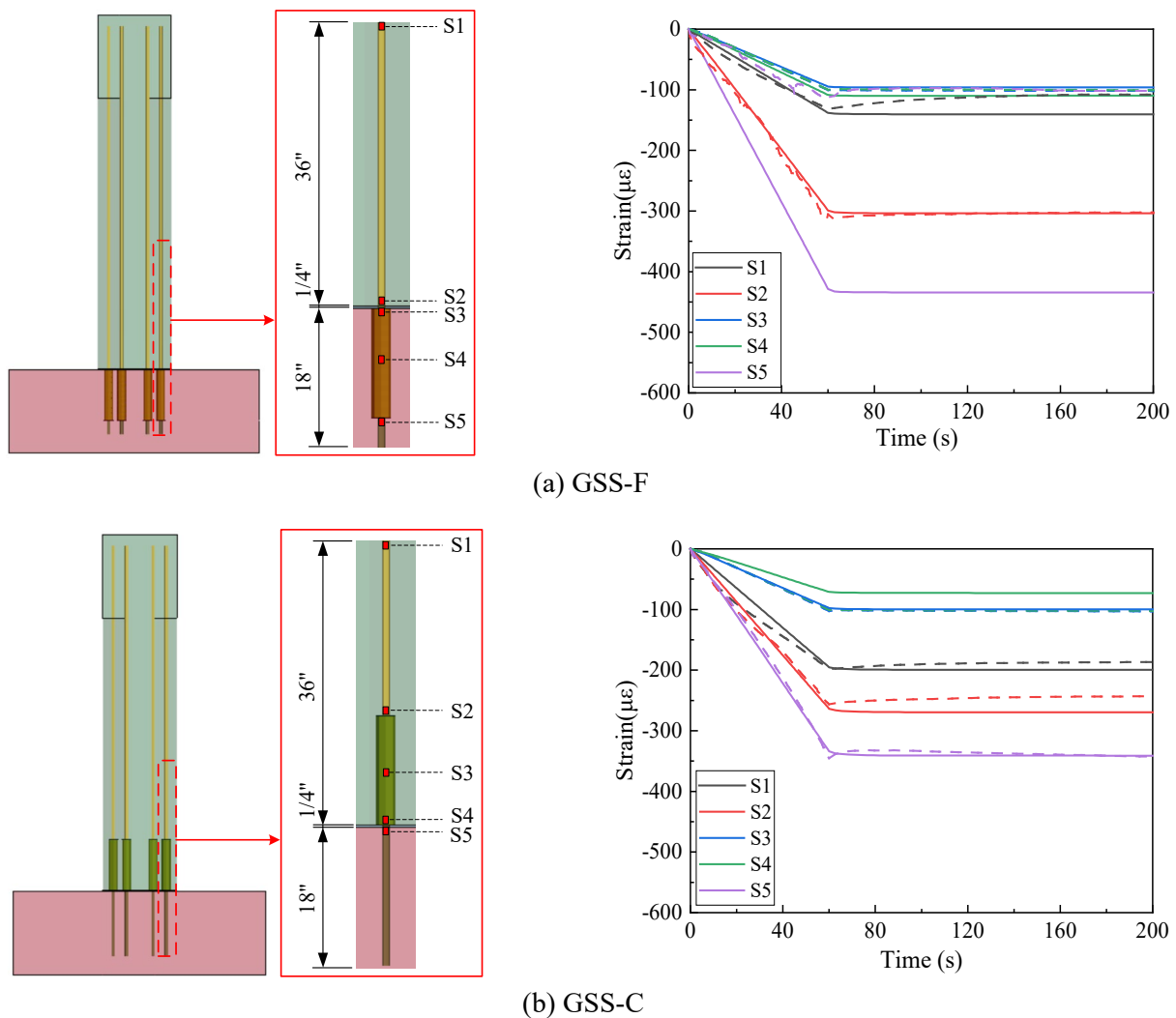
### 4.3 Verification of Simulated Results

This section verifies the accuracy of simulated results for predicting the seismic performance of precast columns. A static analysis ensured the structure started from an equilibrium state by checking boundary conditions, contacts, and bond relationships. The seismic response is evaluated by comparing hysteresis and skeleton curves from both experimental results and FE analysis, and analyzing crack development and damage states at critical drift ratios. These evaluations validated the FE analysis method as a reliable tool for simulating structural behavior under seismic loading.

### 4.3.1 Strain Response During Initial Stage

Before proceeding to a more complex pushover analysis, a static analysis was conducted to ensure the structure started from an equilibrium state. This step verified the initial conditions of the model were correctly set up, including all boundary conditions, contacts, and bond relationships.

Figure 4.6 compares the strain-time history curves from the FE results of the precast cylinder with a single coupler, as discussed in Section 3.7.1, with the curves predicted by the FE models of half-scale columns. The results show good agreement between the two models. Notably, the strain data at S5 from the column results are only 23% of those from the cylinder. This significant discrepancy is attributed to the different load application methods. In the cylinder, the load is applied from the bottom of the footing, which caused stress concentration at the S5 location. In contrast, for the column, the compressive load was applied from the top, allowing for a more uniform load distribution and significantly reducing the strain at S5.



**Figure 4.6** Strain-time history (solid lines: FE results in Section 3.7.1; dash lines: FE results from half-scale columns)

Overall, the FE model successfully captured the initial elastic behavior, indicating the column models are properly set up. The model effectively illustrated the bond-slip law's efficiency within the coupler, ensuring smooth load transfer through the coupler. As a result, the developed FE modeling approach proves to be appropriate for subsequent pushover validation studies.

### **4.3.2 Seismic Response During Pushover Stage**

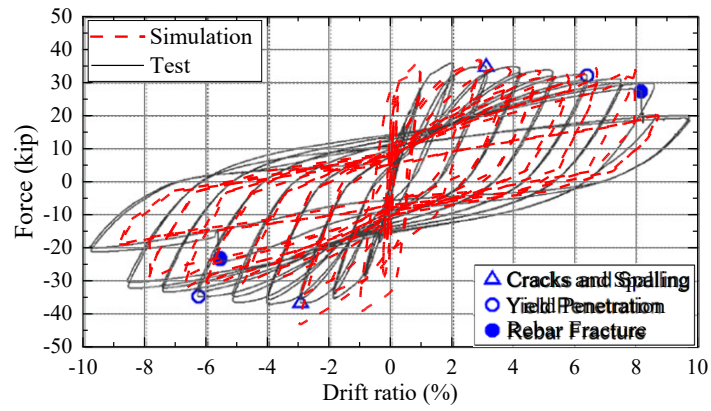
To evaluate the accuracy of seismic performance in FE columns, this section compares hysteresis curves and average skeleton curves derived from both experimental results by Pantelides et al. [2] and FE analysis. The comparison aims to assess consistency between numerical simulations and physical tests, focusing on key parameters, such as effective yield force, yield displacement, ultimate displacement, and displacement ductility capacity. Additionally, the crack development and damage states at critical drift ratios were analyzed to verify the model's ability to capture essential behaviors such as cracking, crushing, and the development of plastic hinges.

#### **4.3.2.1 Hysteresis and Skeleton Curves**

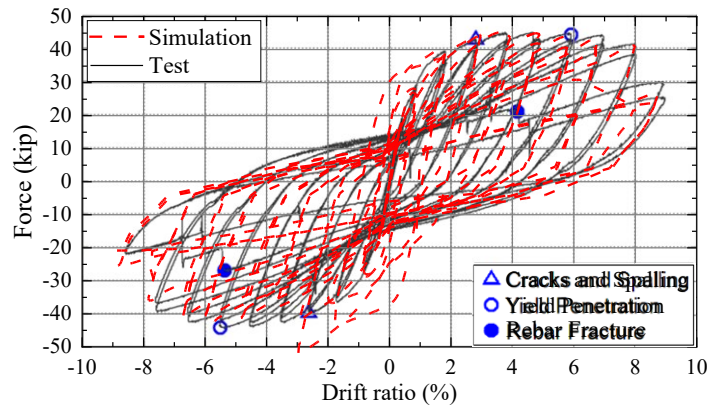
Figure 4.7 compares the hysteresis curves derived from experimental results with those obtained from FE analysis. Overall, hysteresis curves from both the experimental and numerical results demonstrated similar shapes and trends. Initially, before reaching a 2% drift ratio, the hysteresis looped from the numerical simulation appear fuller compared to the experimental observations. This discrepancy was primarily due to more rigid constraints in the FE model, which suggested a greater energy dissipation capability at the beginning of the pushover procedure. As the loading continued and the drift ratio increased, the hysteresis looped from both methods aligned more closely, indicating the FE model accurately captured the progressive stiffness degradation and energy dissipation characteristics observed in the experimental tests.

The good agreement between the experimental and simulated hysteresis curves indicated the FE model successfully captured the seismic performance of the precast column with GSSs. Additionally, the simulation method effectively represented the bond-slip law within the coupler, further validating its accuracy in modeling the dynamic behavior of the structure under seismic loading conditions.

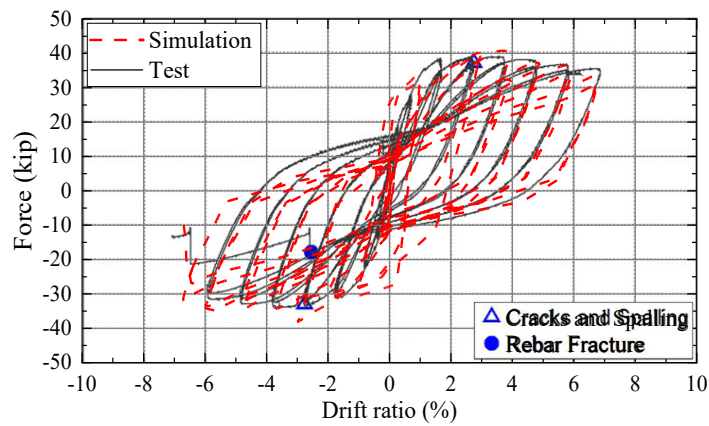




(a) CIP



(a) CIP



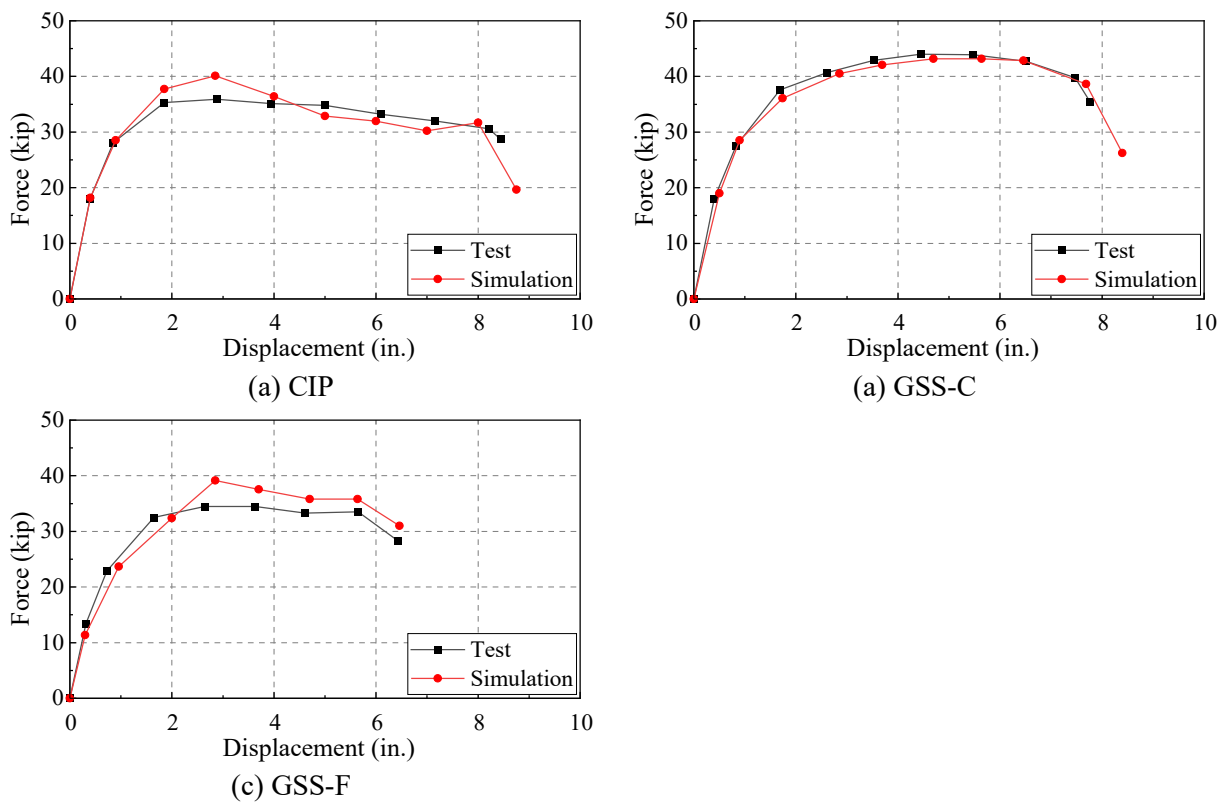
(c) GSS-F

**Figure 4.7** Hysteresis response

To quantitatively verify accuracy of the FE modeling compared to experimental results, the average skeleton curves were derived from the hysteresis curves for both the FE analysis and experimental data. These skeleton curves represented the backbone of the cyclic response, summarizing the overall load-displacement behavior and allowing for a direct comparison between the numerical simulations and physical tests.

By comparing these average skeleton curves, key characteristics were calculated and analyzed, including the effective yield force ( $F_y$ ), effective yield displacement ( $\Delta_y$ ), ultimate displacement ( $\Delta_u$ ), and displacement ductility capacity ( $\mu$ ). According to ACI 374, it was assumed the idealized elasto-plastic curve intersected the average backbone curve at a point where the force was 70% of the effective yield force to determine the effective yield displacement ( $\Delta_y$ ) [63]. The ultimate displacement ( $\Delta_u$ ) was defined as the displacement at which there is a 20% reduction in the lateral load capacity. The displacement ductility capacity ( $\mu$ ) is the ratio of the ultimate displacement to the yield displacement ( $\Delta_u / \Delta_y$ ). These values are summarized in Table 4.3.

In Table 4.3, errors in the displacement ductility capacity between the numerical and experimental results ranged from 3.7% to 9.8%, while the errors in effective yield force ranged from 2.1% to 7.6%. Overall, the FE method demonstrated a high level of accuracy in capturing the lateral bearing capacity and seismic structural resilience, making it a dependable tool for simulating structural behavior under cyclic loading conditions.



**Figure 4.8** Average skeleton curves

**Table 4.3** Comparisons of key characteristics from skeleton curves

Specimens		$F_y$ (kip)	$\Delta_y$ (in.)	$\Delta_u$ (in.)	$\mu$
CIP	Test	33.62	0.946	8.452	8.9
	Simulation	34.73	1.002	8.197	8.2
	<b>Error</b>	<b>3.3%</b>	<b>5.9%</b>	<b>3.0%</b>	<b>7.9%</b>
GSS-C	Test	41.91	1.446	7.788	5.4
	Simulation	41.03	1.404	7.927	5.6
	<b>Error</b>	<b>2.1%</b>	<b>2.9%</b>	<b>1.8%</b>	<b>3.7%</b>
GSS-F	Test	32.63	1.052	6.42	6.1
	Simulation	35.12	1.163	6.391	5.5
	<b>Error</b>	<b>7.6%</b>	<b>10.6%</b>	<b>0.5%</b>	<b>9.8%</b>

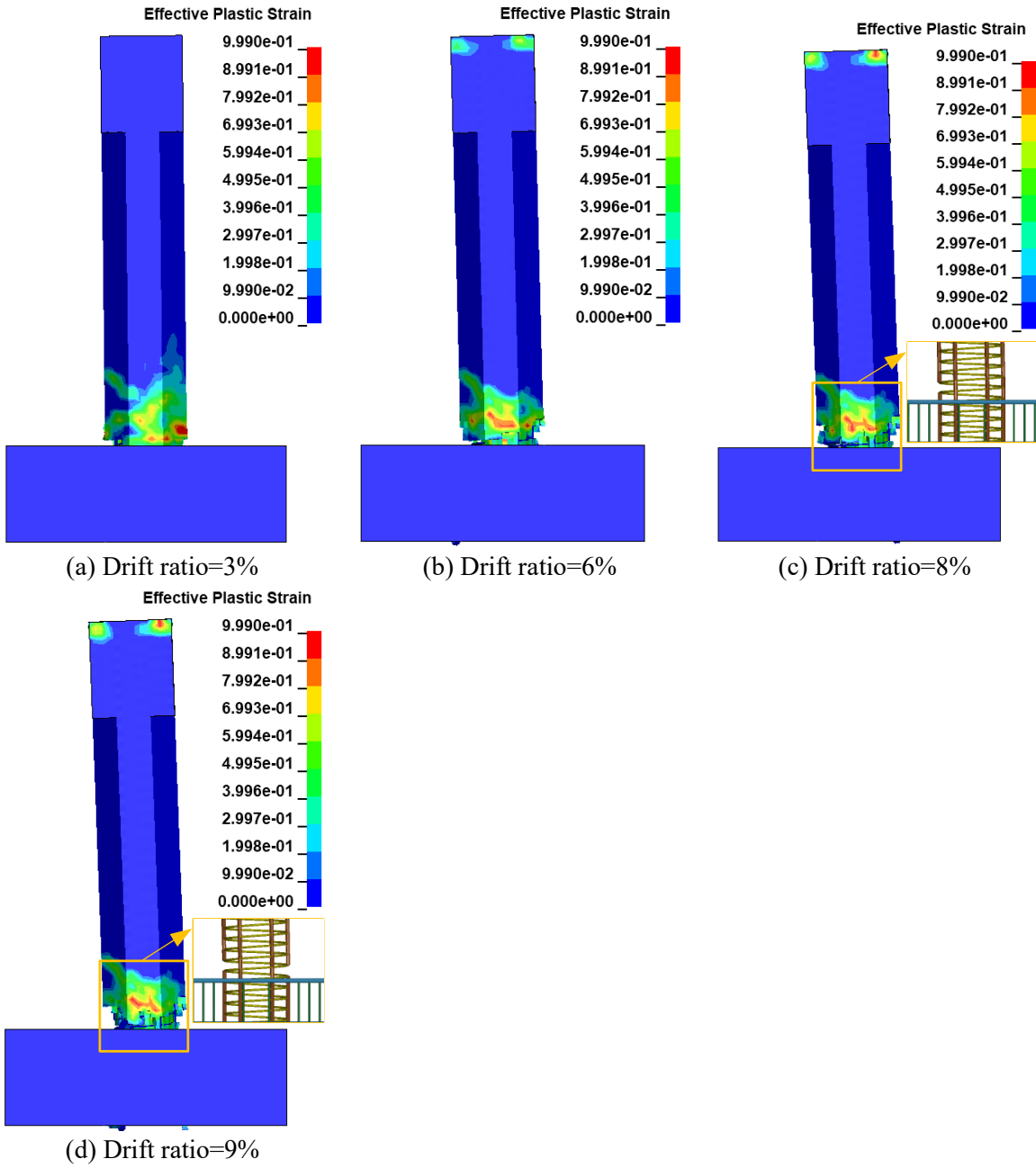
#### 4.3.2.2 Crack Development Progression and Damage Modes

To further understand the crack development process of the three specimens in the FE models, effective plastic strain patterns at critical drift ratios are presented in Figure 4.9.

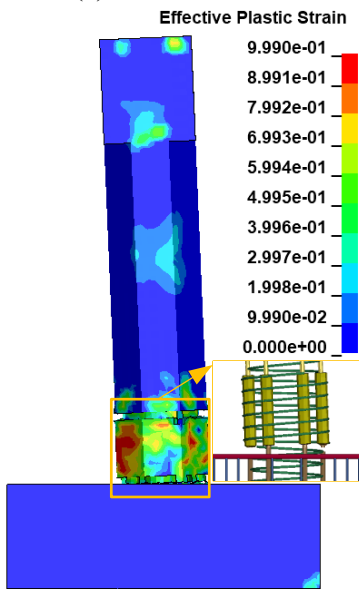
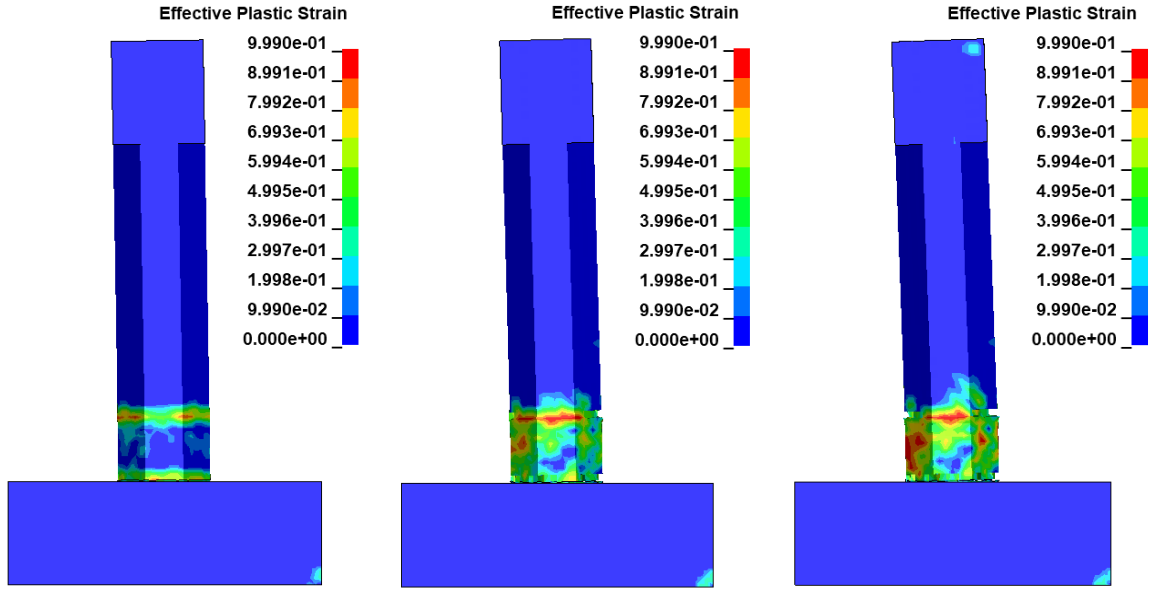
In Figure 4.9 (a), for the CIP specimen, horizontal cracks initially appeared at the column base. As the drift ratio increased to 3%, spalling began at the column corners, indicating significant stress concentration and material degradation in these areas. By a 6% drift ratio, the concrete spalling on both corners of the column in the loading direction propagated upwards. At the 8% drift ratio, the extreme left rebar fractured, followed by the extreme east rebar fracturing above the column-to-footing interface at the 9% drift ratio. This progression is consistent with the experimental results.

In Figure 4.9 (b), unlike the CIP specimen, the GSS-C specimens exhibited different crack development patterns due to the inclusion of GSSs at the column base. At the 3% drift ratio, two major horizontal cracks primarily formed just above the column-to-footing interface and at the top edge of the GSSs. This configuration restricted crack development at the bottom of the column, significantly altering the stress distribution and damage progression. The presence of the GSSs effectively limited the extent of cracking at the column base, thereby enhancing the structural integrity in this critical region. As the drift ratio increased to 6%, these cracks widened, and concrete spalling initiated at both corners of the column. By the 8% drift ratio, the cracks continued to widen, and spalling progressed further. At the 9% drift ratio, the two extreme bars fractured above the column-to-footing interface in the pushover direction due to low cycle fatigue. This behavior closely aligned with the experimental findings.

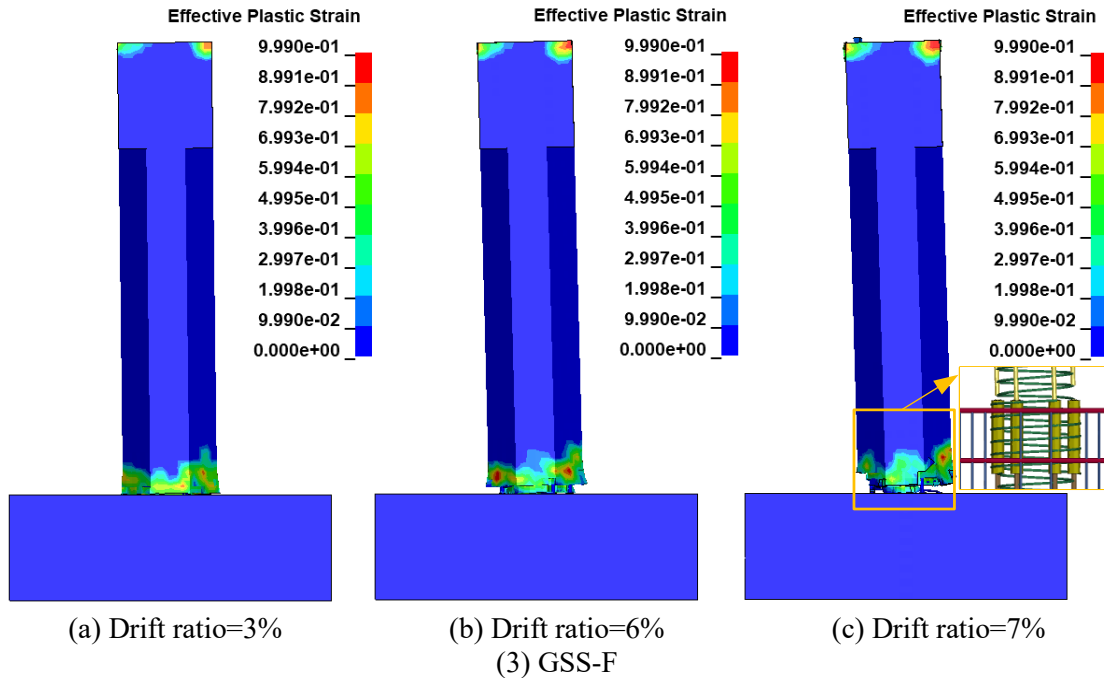
In Figure 4.9 (c), the GSS-F specimen showed horizontal cracks primarily at the column base at the 3% drift ratio. As the drift ratio increased to 6%, these cracks widened, and concrete spalling began at both corners of the column. Notably, unlike the CIP specimen, the damage in the GSS-F column base was more concentrated and did not extend upward. This localized damage was likely due to the configuration of GSSs at the top of the footing, which caused stress concentration and local energy dissipation above the column-to-footing interface. By the 7% drift ratio, the two extreme column reinforcing bars fractured at the top of the coupler. The FE models closely matched the experimental observations.



(1) CIP



(2) GSS-C



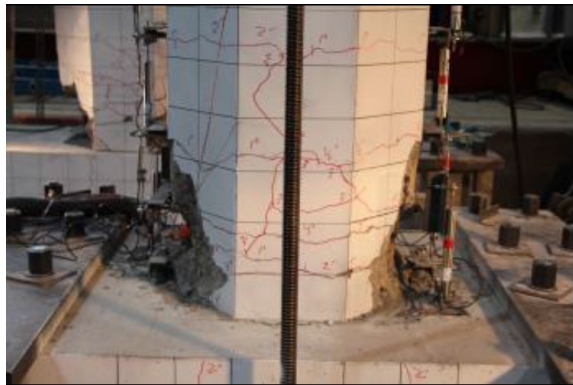
**Figure 4.9** Damage developments

Major damage occurred above the column-to-footing interface. The local damage states at critical drift ratios for both the FE modeling and experimental results are compared in Figures 4.10 - 4.12. In Figure 4.10, for the CIP specimen, initial concrete spalling was observed at the column corners by the end of the 3% drift ratio. By the 6% drift ratio, the spalling continued to propagate, exposing a six-inch height of the rebar cage. At the end of the simulation, the two extreme rebars fractured, leading to an 11-inch height of concrete spalling and further exposing the rebar cage. In Figure 4.11, in the GSS-C specimen, a large crack developed at the bed grout and another at the top section of the GSS connectors by the end of the 3% drift ratio. By the end of the simulation, the damage distribution observed in the experiment was more severe than in the numerical model. This discrepancy arose because, in the FE models, the cover concrete retained some load-carrying capacity even when damaged. In contrast, in actual tests, severely cracked or peeled-off cover concrete fails to transfer loads. This difference explains variations in damage distribution between the simulation and experimental results. In Figure 4.12, for the GSS-F specimen, an initial crack at the bed grout was observed at the 3% drift ratio. By the end of the simulation, the extreme column reinforcing bar fractured above the interface, accompanied by eight inches of concrete spalling and exposing the rebar cage.

In summary, the FE models accurately reflected the crack distribution and damage progression observed in the experimental specimens. They effectively captured key processes, such as cracking, crushing, and the development of plastic hinges. These results validate the suitability of the FE analysis method for further study of seismic performance in precast concrete columns after impact accidents.



(a) Drift ratio=3% (cracks and spalling)

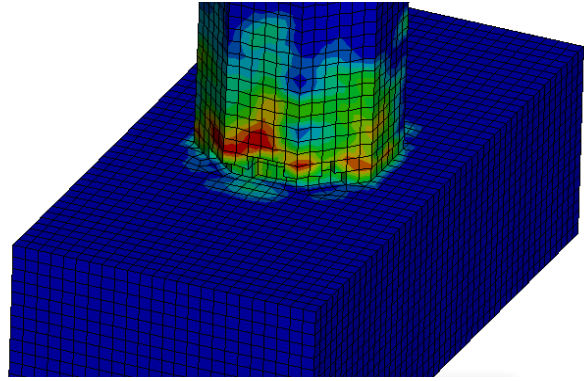


(b) Drift ratio=6% (spalling and inclined cracks)

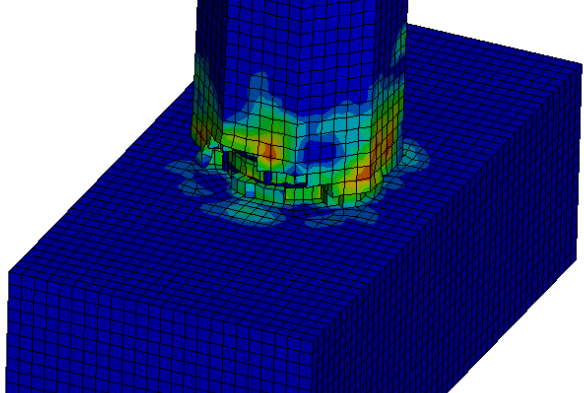


(c) At the end of test (cracks, spalling, concrete delamination, and fractured rebar)

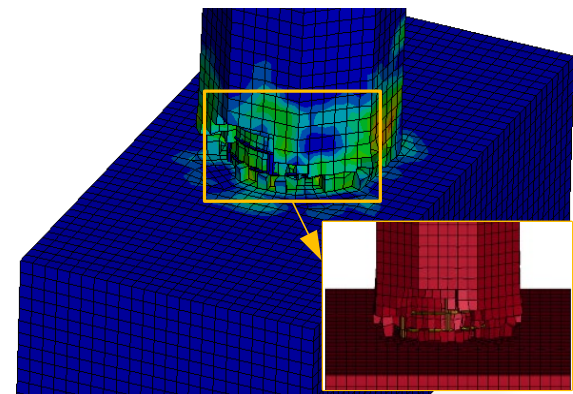
(i) Experimental observations



(a) Drift ratio=3%



(b) Drift ratio=6%



(c) At the end of simulation

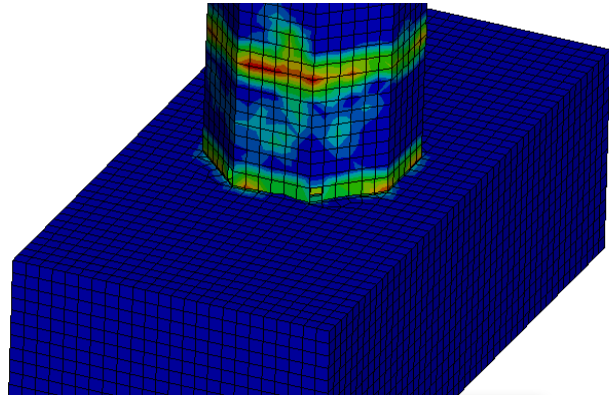
(ii) Numerical results

**Figure 4.10** Comparison of CIP's damage states





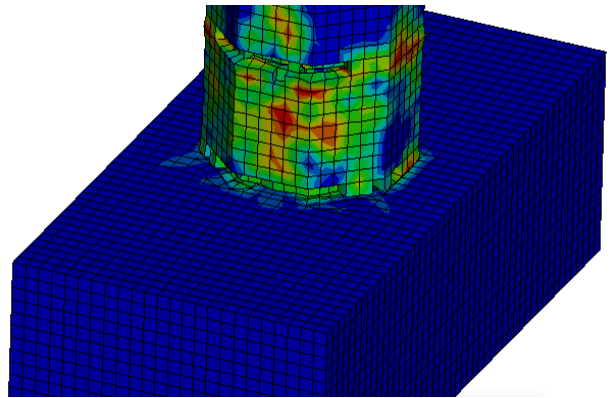
(a) Drift ratio=3% (cracks and spalling)



(a) Drift ratio=3%



(b) Drift ratio=6% (cracks, spalling, and yield penetration)

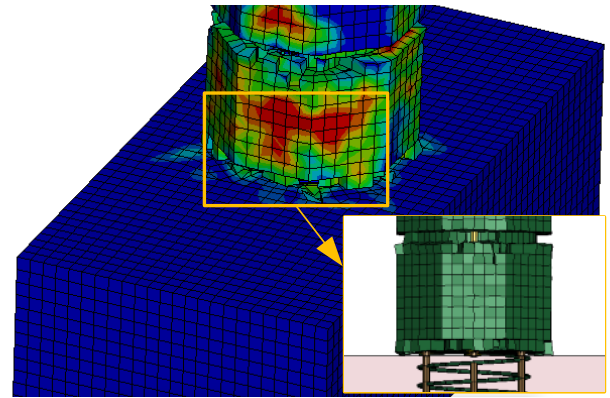


(b) Drift ratio=6%



(c) At the end of test (spalling, exposed rebar cage, and fractured bar)

(i) Experimental observations



(c) At the end of simulation

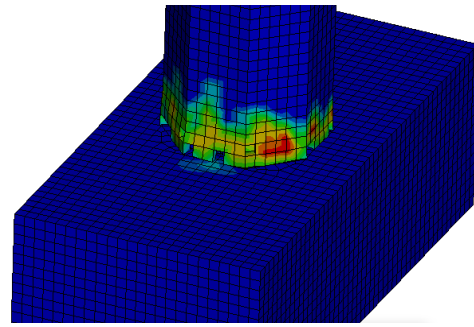
(ii) Numerical results

**Figure 4.11** Comparison of GSS-C's damage states





(a) Drift ratio=3% (cracks and spalling)

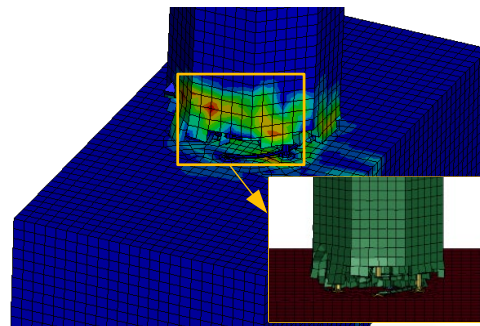


(a) Drift ratio=3%



(c) At the end of test (cracks, spalling, fractured rebar, and exposed rebar cage.)

(i) Experimental observations



(c) At the end of simulation

(ii) Numerical results

**Figure 4.12** Comparison of GSS-F's damage states

## 4.4 Summary

This chapter outlines the modeling techniques used to simulate the seismic behavior of precast columns and validates the FE models against experimental results. The validation encompassed strain-time history curves for load transfer, hysteresis curves, average skeleton curves, and analysis of crack development and damage states at critical drift ratios. The FE models showed good agreement with experimental results in both initial and pushover stages, confirming their accuracy and reliability.

The comparison of strain-time history curves between the FE results of a precast cylinder with a single coupler and half-scale columns showed consistency, successfully capturing the initial elastic behavior and illustrating the bond-slip law within the coupler. This supports the FE modeling approach for subsequent pushover validation studies.

The alignment between experimental and simulated hysteresis curves indicated the FE models effectively captured the seismic performance of precast columns with GSSs. Errors in displacement ductility capacity ranged from 3.7% to 9.8%, while errors in effective yield force ranged from 2.1% to 7.6%, demonstrating the high accuracy of the FE method in capturing lateral bearing capacity and seismic resilience.

Further analysis of crack development and damage states at critical drift ratios for the three specimens accurately reflected the experimental observations. The FE models effectively captured key processes, such as cracking, crushing, and the development of plastic hinges, validating the FE analysis method for further studies of seismic performance in precast concrete columns, especially after impact accidents.

## 5. FINITE ELEMENT ANALYSIS OF HALF-SCALE COLUMN UNDER SEQUENTIAL IMPACT AND SEISMIC LOADS

A 3D finite element (FE) model of a half-scale column was developed using LS-DYNA in Chapter 4. This model was calibrated with material properties, mesh size sensitivity, and bond-slip relationships within coupler to ensure accuracy for both impact and seismic scenarios. To explore the residual seismic capacity of precast columns following an impact accident, the column model was subjected to a sequential loading protocol. First, an impact load was applied to simulate damage from a sudden impact accident. Following this, a quasi-static cyclic loading protocol was implemented to simulate seismic activity and evaluate the column's residual capacity.

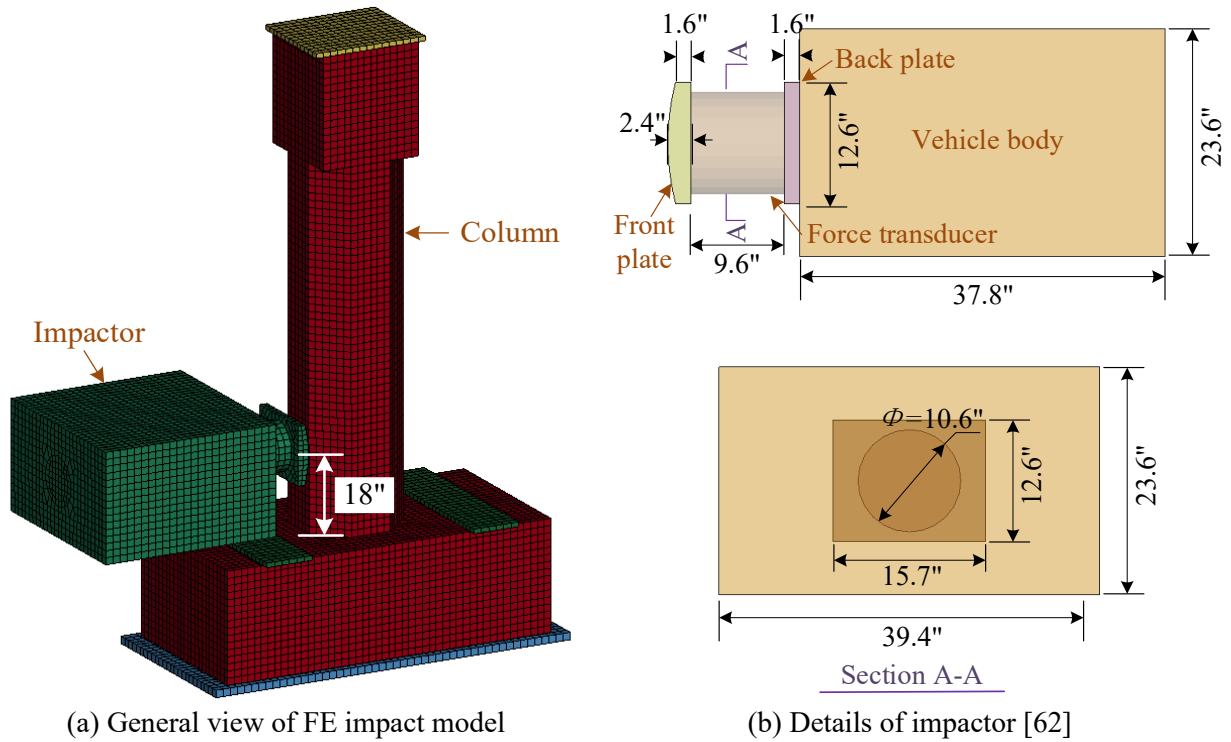
After the impact loading phase, the damage distributions at the end of the impact were compared among three categories of columns. Displacement curves of the columns at various height levels were generated and compared to quantitatively investigate the structural impact response under different impact velocities. Following this, a quasi-static cyclic loading phase was conducted to observe and compare the damage patterns in these columns at various drift ratios: 1%, 2%, and at the point of failure, gaining insights into the damage progression under cyclic loading. Skeleton curves were derived from the FE results to explore the effect of impact on reducing the seismic capacity of columns. The displacement ductility capacity ( $\mu$ ) was calculated and analyzed. The relationship between impact velocity and vehicle mass with respect to code requirements was plotted to determine the residual seismic capacity of the columns after an impact accident. These figures guided the assessment and necessary reinforcement measures to ensure structural integrity and safety in future seismic events. It should be noted that the damage described in this chapter does not necessarily reflect real-world vulnerabilities as the validated column was only a half-scale model. However, the parametric nature of this study allows for general results to be indicative of real-world applications and, as such, can be scaled to full size piers.

### 5.1 General Description of FE Models

The three half-scale columns developed in Chapter 4 were utilized, maintaining the calibrated material properties, mesh size sensitivity, and bond-slip relationships within the coupler. To simulate an impact scenario, an impactor was added at a height of 1 ft 6 in above the bottom of the column part. In Chen et al., a rigid model vehicle was specifically designed for impact testing and modeling [62]. The model vehicle comprised a front plate, force transducer, back plate, and vehicle body. The dimensions of the vehicle body were 37.8 inches  $\times$  39.4 inches  $\times$  23.6 inches, while the front and back plates were each 1.6 inches thick. The front plate had an arched surface, and the force transducer was a cylinder with a diameter of 10.6 inches and a height of 9.6 inches. The general view of the FE model and dimensions of impactor are illustrated in Figure 5.1.



According to the preliminary literature review of vehicle impact, two masses of lightweight vehicles were used for impact studies: a Toyota Yaris (0.9 tons), a Dodge Ram (2 tons). The study examined five different velocity ranges, from 22 mph to 60 mph. The specific collision scenarios examined are summarized in Table 5.1. For instance, the case titled "0.9 t - 22 mph" indicates an impact scenario where the total mass of the impactor was 0.9 tons, and the impact velocity was 22 mph.

The impactor was modeled using SOLID\_164 elements, with an average mesh size of 1 inch (25.4 mm). It was assumed to be rigid and utilized the \*MAT\_RIGID material model, with two varying densities to represent the specific masses of the impact scenarios. All boundary conditions were consistent with those described in Chapter 4. Additionally, the \*CONTACT\_AUTOMATIC\_SURFACE\_TO\_SURFACE model was used to describe the interactions between the specimens and the impactor, employing both static and dynamic friction coefficients of 0.3 [64].



**Figure 5.1** Description of FE models (unit: inch)

**Table 5.1** List of collision cases

Types of vehicles	FE models	Total mass (ton)	Velocity level	Velocity of vehicles	Collision case
Toyota Yaris		0.9	Low ( $\leq 35$ mph)	22 mph	0.9 t - 22 mph
				31 mph	0.9 t - 31 mph
			Mediate ( $> 35$ mph and $< 60$ mph)	40 mph	0.9 t - 40 mph
				49 mph	0.9 t - 49 mph
			High ( $\geq 60$ mph)	60 mph	0.9 t - 60 mph
Dodge Ram		2	Low ( $\leq 35$ mph)	22 mph	2 t - 22 mph
				31 mph	2 t - 31 mph
			Mediate ( $> 35$ mph and $< 60$ mph)	40 mph	2 t - 40 mph
				49 mph	2 t - 49 mph
			High ( $\geq 60$ mph)	60 mph	2 t - 60 mph

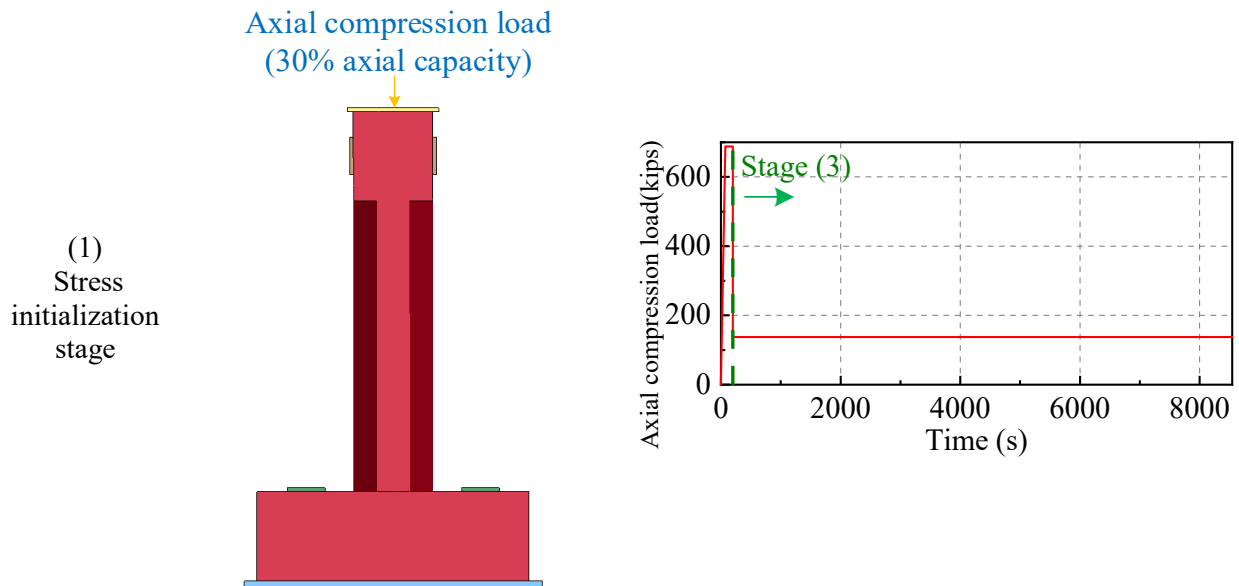
## 5.2 Loading Procedures

The RESTART function enables the effective execution of loading sequence analysis. To explore the residual seismic capacity of precast columns following an impact accident, as illustrated in Figure 5.2, the analysis consisted of three stages:

(1) Stress initialization stage: To establish the initial stress state, the self-weight of the structure was applied using \*LOAD\_BODY\_Y with an acceleration curve. Additionally, an axial prestressing load equivalent to 30% of the column's axial capacity (687.95 kips) was applied using \*LOAD\_RIGID\_BODY to simulate the typical gravity load in a bridge column [65]. Once static equilibrium was achieved, the state of the structure was saved for subsequent analysis.

(2) Impact stage: Following stress initialization, an impactor was added at a height of 1 ft 6 in above the bottom of the column, with impact velocities set at 22 mph, 31 mph, 40 mph, 49 mph, and 60 mph, respectively. The initial velocity of the impactor was set using \*INITIAL\_VELOCITY\_GENERATION. During this stage, the axial prestressing load remained at 30% of the column's axial capacity (687.95 kips) [65].

(3) Lateral cyclic loading stage: After the impact stage, a pushover loading plate was employed to control displacement using \*BOUNDARY\_PRESCRIBED\_MOTION\_RIGID, positioned eight feet above the column base. The cyclic loading protocol applied displacement control, executing two cycles for each drift ratio ranging from 0.5% to 10%. Initially, the displacement rate was set at 1.2 in./min until the 3-inch drift ratio was reached, after which the rate was increased to 4 in./min and maintained at this speed for the remainder of the test. The axial prestressing load was reduced to 6% of the column's axial capacity (137.59 kips) to remain consistent with Pantelides et al. (2017) [2].



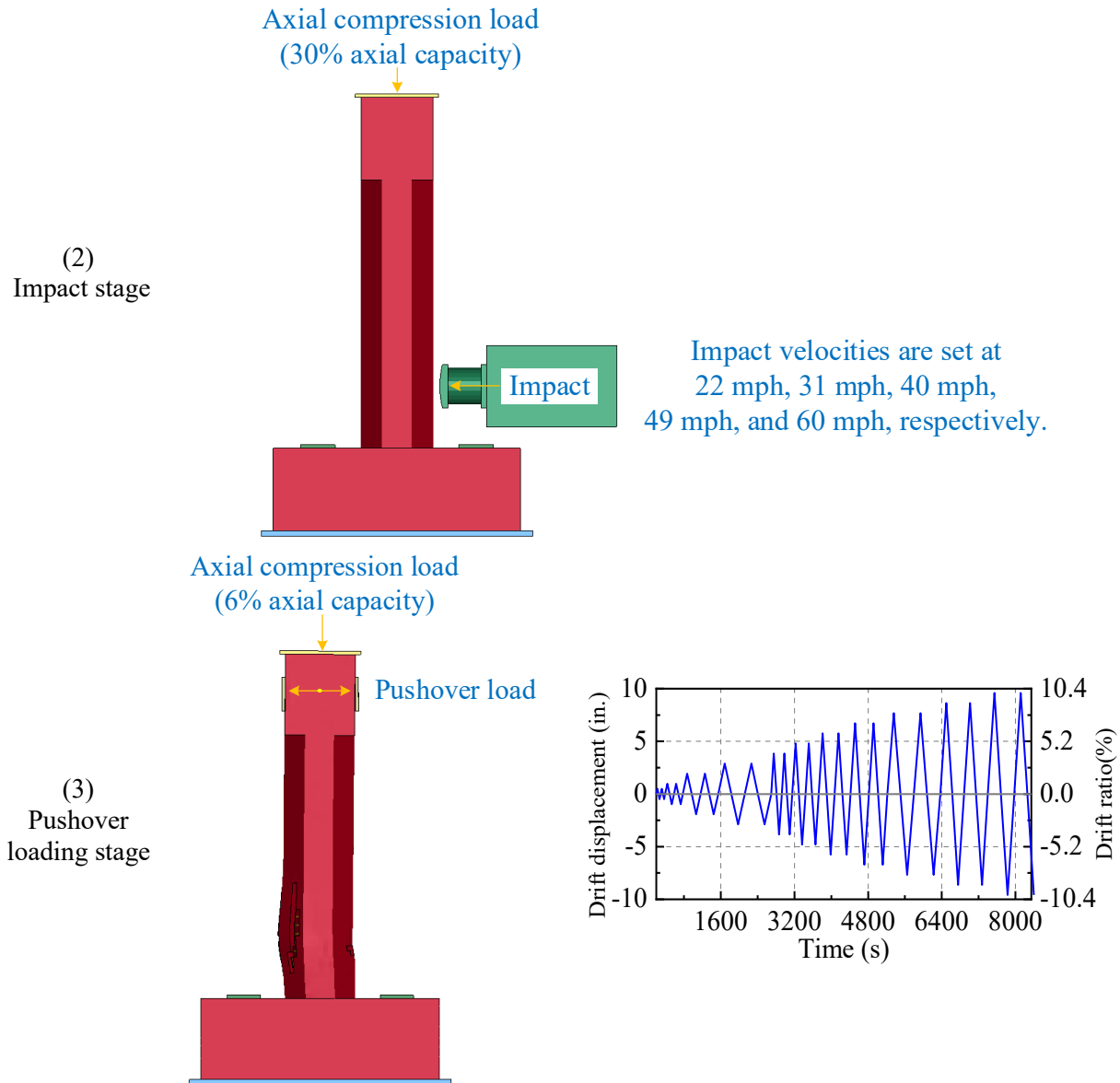


Figure 5.2 Loading stage description

### 5.3 Dynamic Response During Impact

After the impact loading phase, the damage distributions of three types of columns at the end of the impact were summarized by the mass of the impactor and velocity, as shown in Figure 5.3~5.5. Generally, the comparison of each set of damage patterns revealed that an increase in vehicle velocity resulted in progressively more severe damage to the piers.

In Figure 5.3, the first set of results shows the impact of the Toyota Yaris (0.9 tons) at various velocities. At 22 mph, the damage to the CIP pier was relatively minor. At a velocity of 31 mph, a single shear crack at a 45-degree angle was observed at the bottom of the pier on the impact surface. Meanwhile, a small area of concrete spalling was noted on the opposite side of the pier, indicating the localized effect of the impact. As the impact velocity increased to 40 mph and 49 mph, these local damages spread throughout the column section. At 60 mph, a significant diagonal crack at a 30-degree angle was observed, extending

from the impact location to the top of the pier and accompanied by bending flexural cracks. This was attributed to the combined effects of the bending moment and the large shear force, resulting in a typical punching failure of the CIP pier.

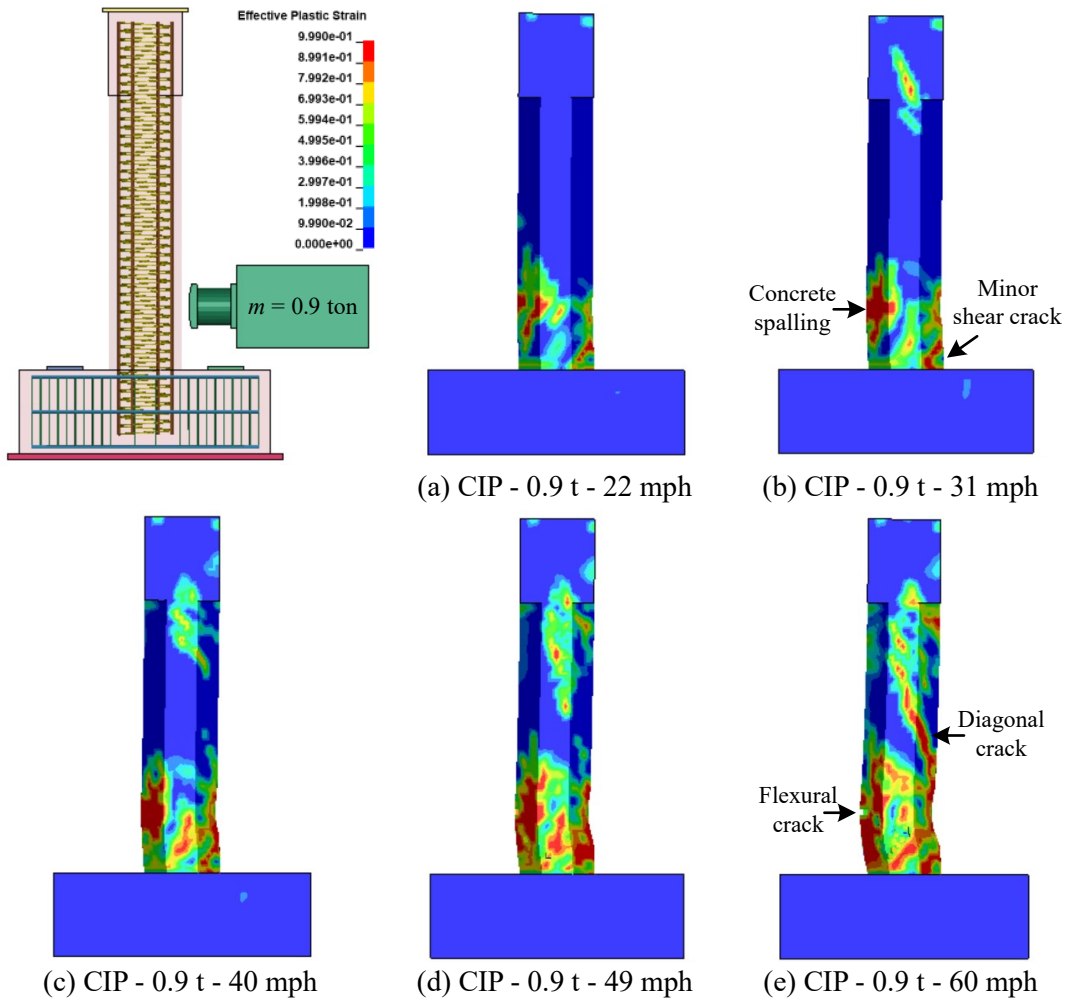
In the second set of results, examining the impact of the Dodge Ram (2 tons) at various velocities, a minor shear crack at a 45-degree angle on the impact surface and an area of concrete spalling on the opposite side were observed at a velocity of 22 mph. At 49 mph, a significant crack at a 30-degree angle extended from the impact location to the top of the pier. Additionally, more shear cracks were found at the top of the pier on the impact face. Based on these observations, the failure mode of the column was punching shear failure.

In Figure 5.4, the crack distributions and failure modes of the precast concrete specimens with Grouted Sleeve Splices (GSSs) at the column base were notably different from those of the CIP specimens. In the first set of results, examining the impact of the Toyota Yaris (0.9 tons) at various velocities, the damage to the GSS-C pier at 22 mph was relatively minor. At a velocity of 31 mph, there was less concrete spalling on the opposite impact surface. A horizontal shear crack initiated at the grout bed interface between the footing and the column. Additionally, erosion of the grout element in the coupler was observed due to stress concentration in that area. At a velocity of 49 mph, a significant horizontal shear crack was observed through the top section of the GSSs. Compared to the case "CIP - 0.9 t - 60 mph" the GSS-C specimen under the same conditions exhibited fewer shear cracks on both the top and bottom of the column, and a smaller area of concrete spalling on the opposite impact surface. This indicates the addition of GSSs enhanced the impact resistance under lightweight vehicle impacts. The improved performance may be attributed to the impact location being close to the GSSs, which helped to increase the rigidity of this part of the column.

In the second set of damage patterns, involving the impact of the Dodge Ram (2 tons) at various velocities, several distinct failures are observed. At 22 mph, a grout bed failure occurred on the corner of the impact side. At a velocity of 31 mph, grout failure in the coupler is noted, leading to bond failure with the rebar. At 40 mph, a significant horizontal shear crack appeared at the top of the GSSs. At 60 mph, a diagonal shear crack at a 10-degree angle extended from the impact location to the top of the pier. Compared to the 30-degree-angle diagonal shear crack observed in the case "CIP - 2 t - 60 mph," the addition of GSSs helped to reduce the angle of the shear crack. This reduction in shear crack angle indicates that the GSSs effectively delayed the onset of significant cracking, thereby helping to maintain the column's bearing capacity and preventing collapse.

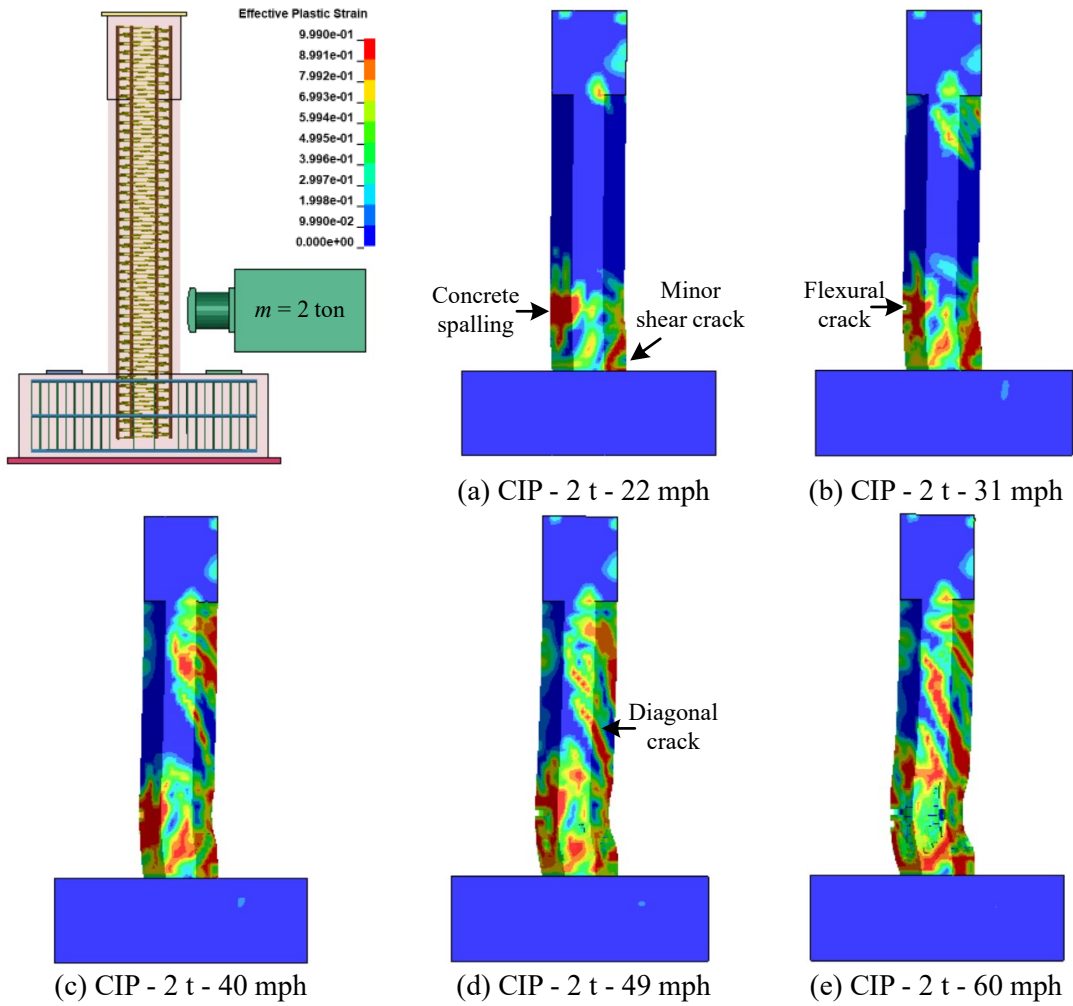
In Figure 5.5, the crack distributions and failure modes of the precast concrete specimens with Grouted Sleeve Splices (GSSs) at the footing top (GSS-F) were notably different from those of the CIP and GSS-C specimens. In the first set of results, examining the impact of the Toyota Yaris (0.9 tons) at various velocities, a grout bed failure occurred at the corner of the impact side at 22 mph. At a velocity of 49 mph, there was less concrete spalling on the opposite impact surface, and no evident damage was observed to the grouted sleeve connection, which remained intact throughout the collision process. At 60 mph, a 0.5-inch rebar slip was found on the extreme rebar on the impact side. Additionally, a shear crack initiated from the impact location and extended to the bottom corner of the opposite impact side, indicating a shear failure. This failure mode was different from the punching shear failure observed in the CIP and GSS-C specimens. Additionally, compared to the case "CIP - 0.9 t - 60 mph," the GSS-F specimen under the same conditions exhibited fewer shear cracks on the top of the column. This may be attributed to the grout bed at the footing-column interface, which tended to crack first, causing the column to lose its rigid connection with the footing. As a result, the column became more flexible in the lateral direction, allowing more energy to be dissipated by the rebar rather than the concrete. This redistribution of energy reduced the stress on the concrete, leading to fewer shear cracks.

In the second set of damage patterns, involving the impact of the Dodge Ram (2 tons) at various velocities, several distinct failures were observed. At 22 mph, a grout bed failure occurred at the corner of the impact side. At a velocity of 49 mph, a shear crack initiated from the impact location and extended to the bottom corner of the opposite impact side, accompanied by concrete spalling on this side. Additionally, a 0.4-inch rebar slip was found on the extreme rebar on the impact side. When the velocity increased to 60 mph, the rebar slip increased to 0.8 inches.



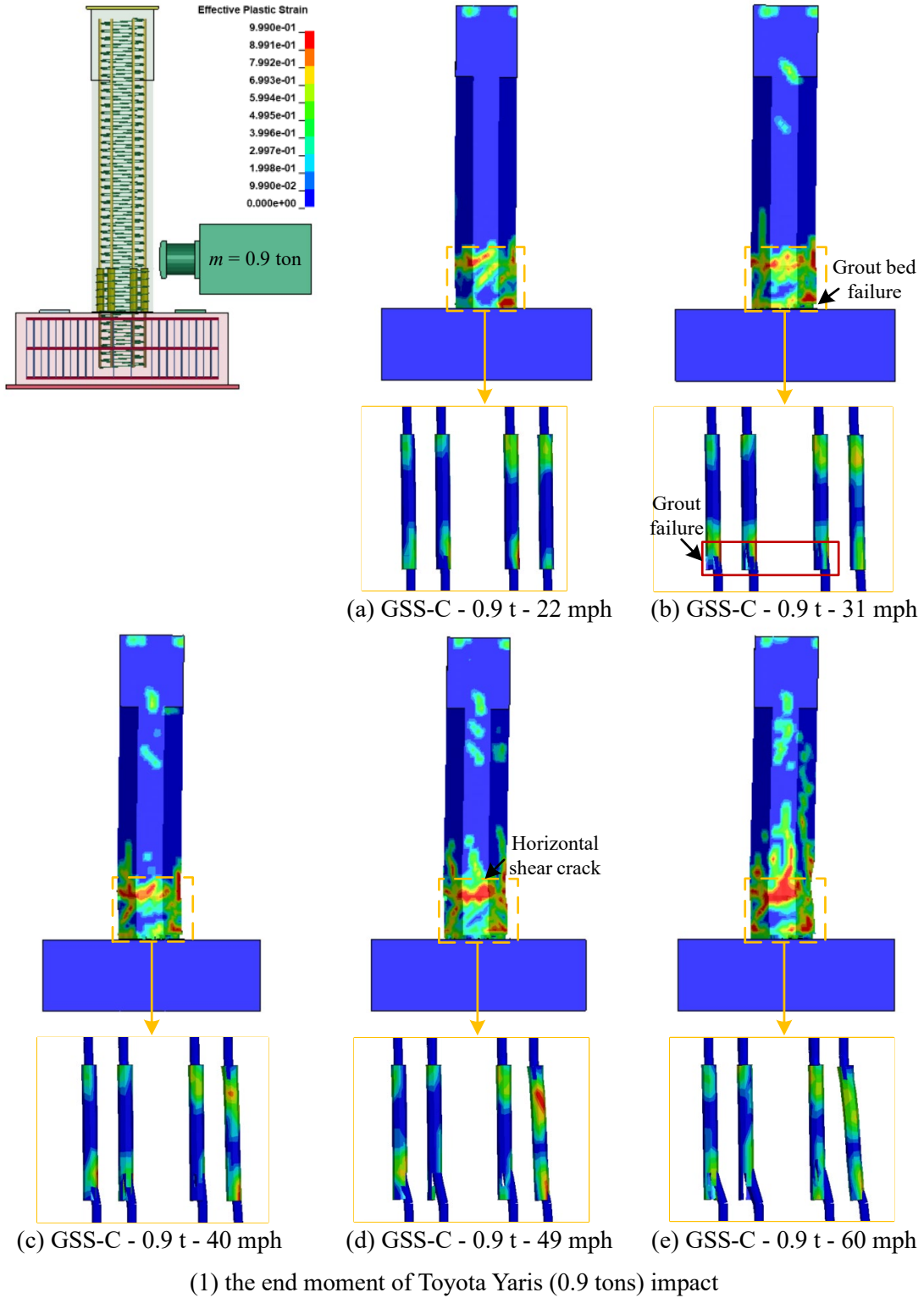
(1) the end moment of Toyota Yaris (0.9 tons) impact

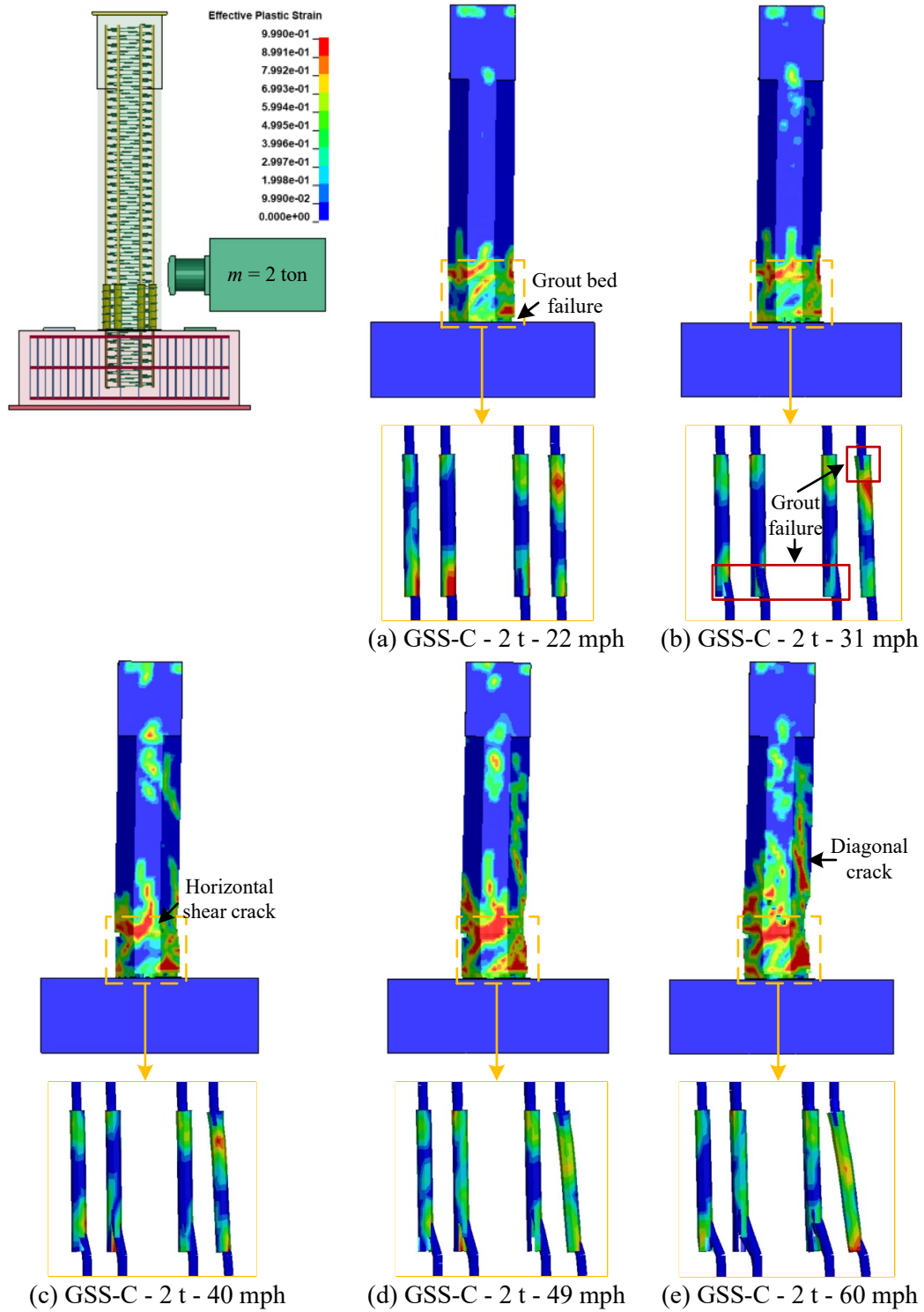




(2) the end moment of Dodge Ram (2 tons) impact

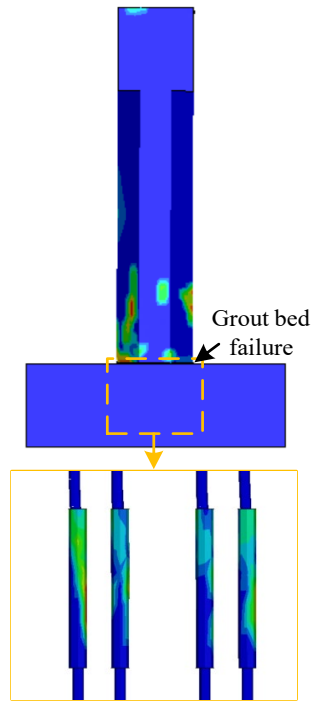
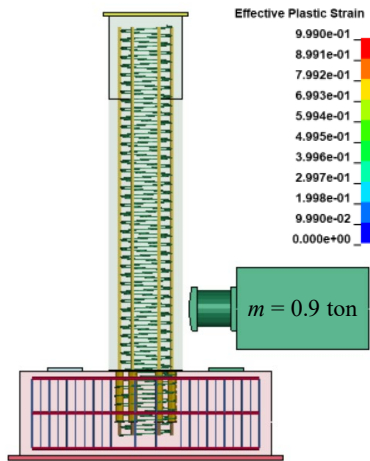
**Figure 5.3** Failure modes of CIP



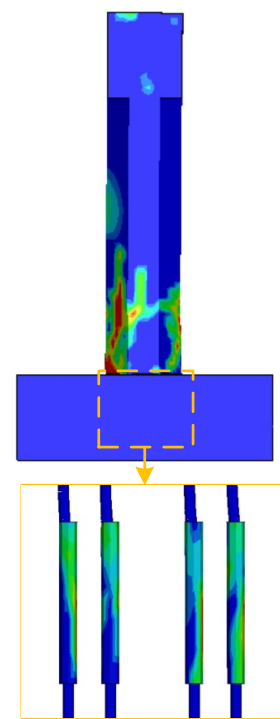


(2) the end moment of Dodge Ram (2 tons) impact

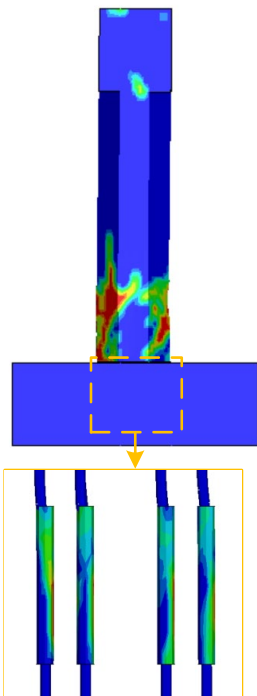
**Figure 5.4** Failure modes of GSS-C



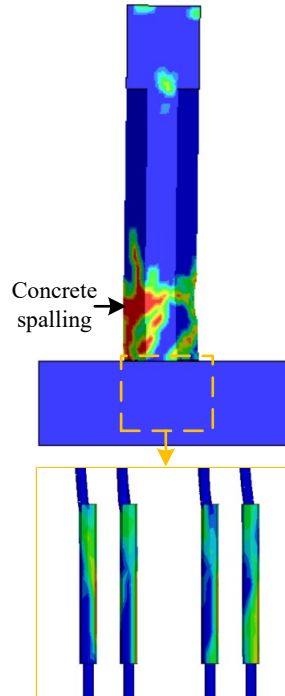
(a) GSS-F - 0.9 t - 22 mph



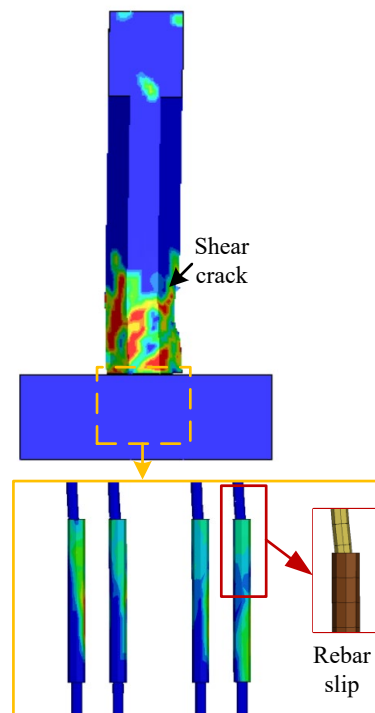
(b) GSS-F - 0.9 t - 31 mph



(c) GSS-F - 0.9 t - 40 mph

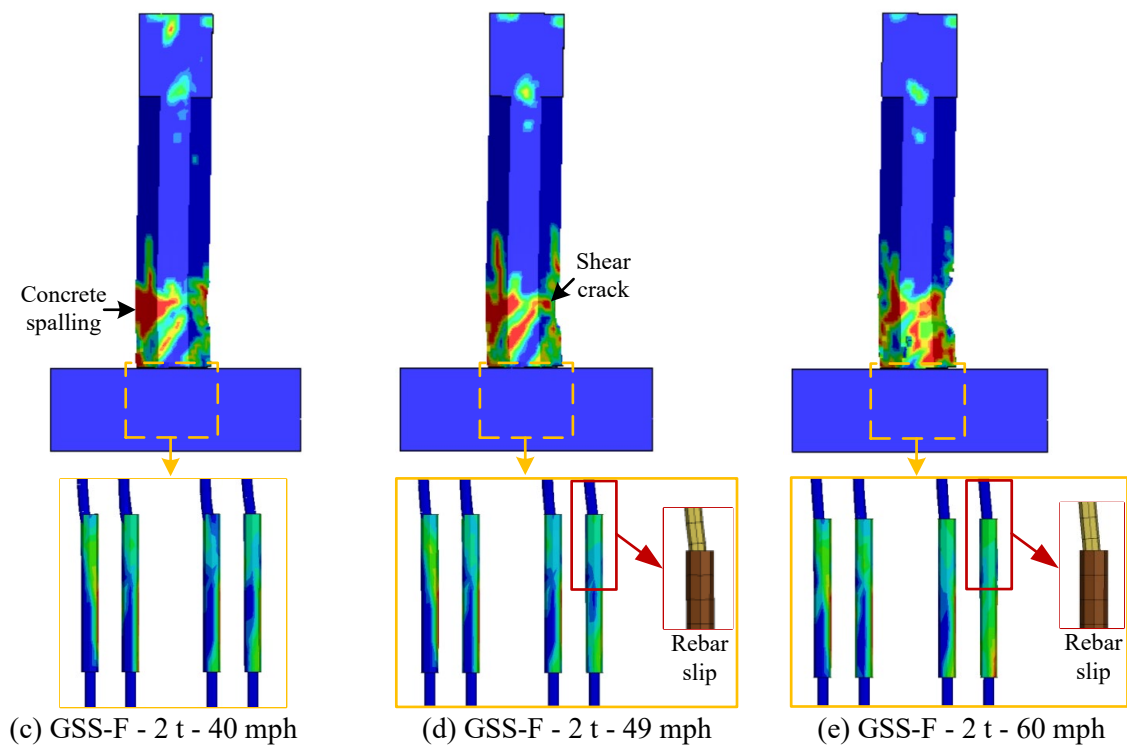
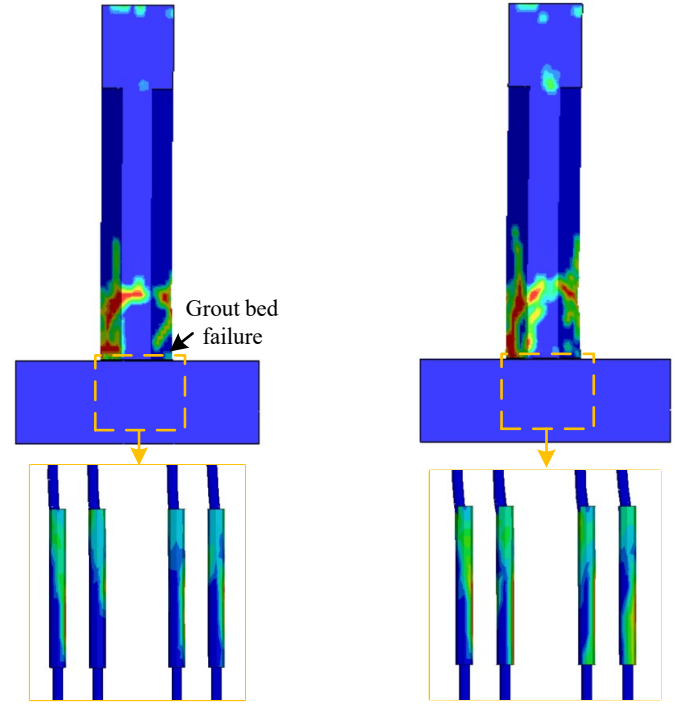
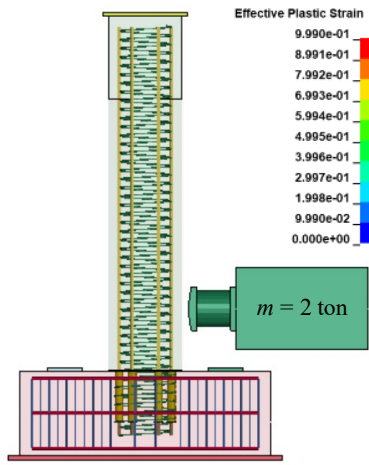


(d) GSS-F - 0.9 t - 49 mph



(e) GSS-F - 0.9 t - 60 mph

(1) the end moment of Toyota Yaris (0.9 tons) impact



(2) the end moment of Dodge Ram (2 tons) impact

**Figure 5.5** Failure modes of GSS-F

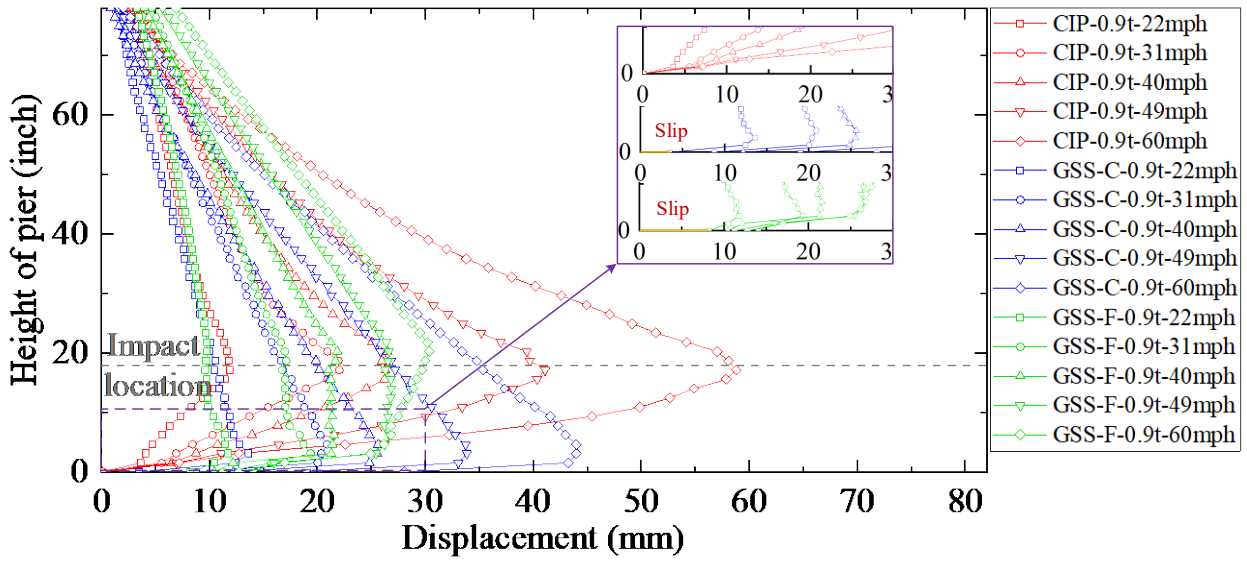
To quantitatively investigate the structural impact response of various categories of columns under different impact velocities, displacement curves of the columns at various height levels at the end moment of the impact were generated and compared, as shown in Figure 5.6.

In Figure 5.6 (1), under the impact of the Toyota Yaris (0.9 tons), the maximum displacement for the CIP columns occurred at the impact location, which was 18 inches above the column base. No slip was observed at the footing-column interface, indicating a strong connection between the footing and column. This strong connection means the impact energy was absorbed by the concrete, resulting in severe concrete cracks in CIP specimens.

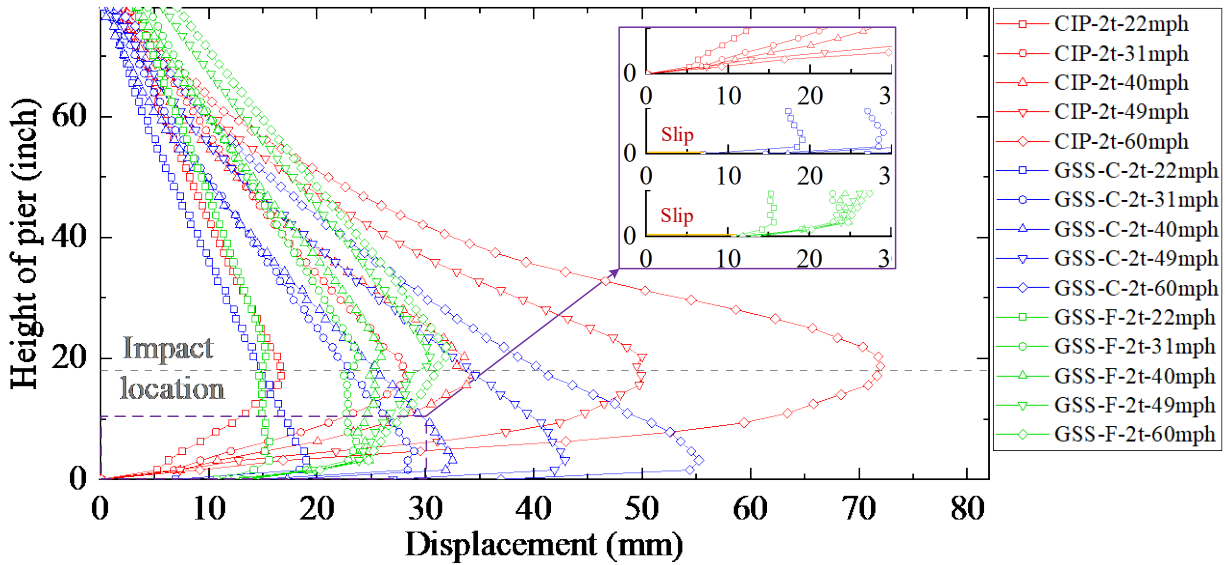
For the GSS-C columns, the maximum displacements were observed around three inches above the column base, with smaller extreme lateral displacements compared to those in the CIP columns. At the bed grout location, significant increasing slips were noted at the column base, ranging from 4 mm to 28 mm with higher impact velocities. This suggests that the GSS-C columns experienced more base slip due to the presence of GSSs in the column base, which contributed a more rigid section under impact location. The impact caused these sections to move forward, with more impact energy absorbed by the GSSs, resulting in fewer concrete cracks observed on the surface of the column.

For the GSS-F columns, the response varied with increasing velocities. When the velocity was less than 40 mph, the maximum displacement was found around three inches above the column base. As the impact velocity increases, the location of the maximum displacement shifted up to the impact point. At the column base, there was a slip of around 10 mm, which did not change significantly with velocity, unlike in the GSS-C columns. GSS-F columns exhibited smaller average displacement below the impact locations compared to GSS-C and CIP columns. This was because a grout bed failure occurred at the corner of the impact side at the beginning of the impact, causing the column to lose its rigid connection with the footing. More impact energy was dissipated by the initial column base slip, resulting in fewer concrete cracks and less displacement response in GSS-F columns.

In Figure 5.6 (2), similar findings were observed under the impact of the Dodge Ram (2 tons). The results confirmed that precast columns with GSSs at the footing-column joint demonstrated better impact resistance compared to cast-in-place (CIP) columns. The GSSs reduced the severity of cracks and displacements under high-velocity impacts.



(1) the end moment of Toyota Yaris (0.9 tons) impact



(2) the end moment of Dodge Ram (2 tons) impact

Figure 5.6 Displacement responses of columns

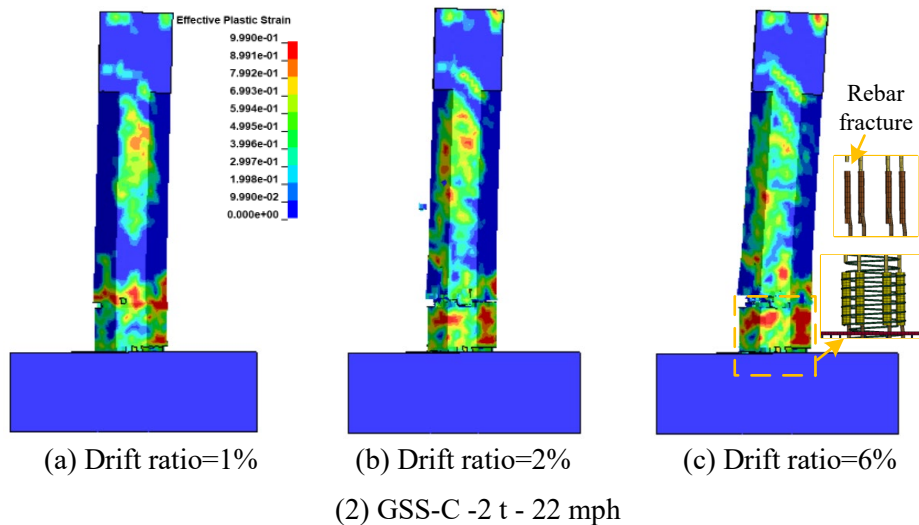
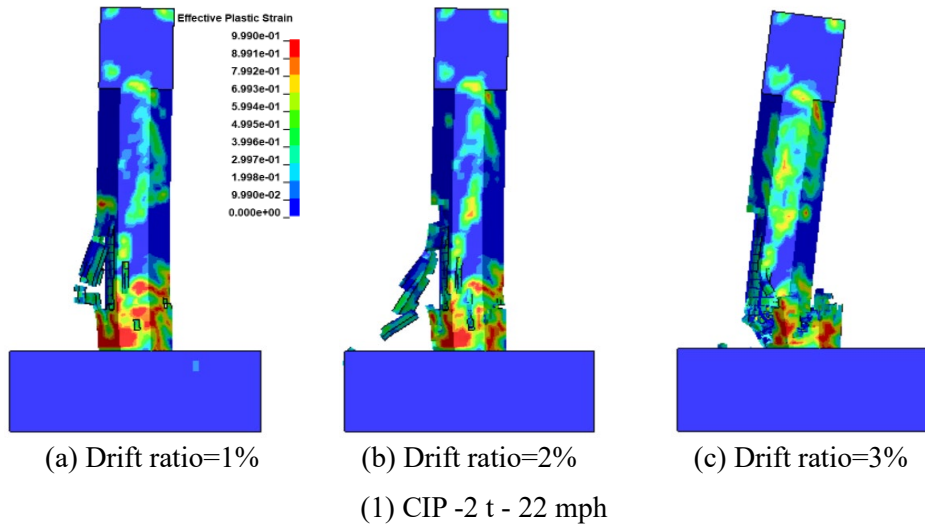
## 5.4 Residual Seismic Capacity Assessment of Post-impact Stage

To gain insights into the damage progression of post-impact columns under cyclic loading, three categories of columns, each impacted by a Dodge Ram (2 tons) at a velocity of 22 mph, were selected for detailed analysis and comparison. Figure 5.7 provides a comprehensive summary of the damage distribution observed in these columns at various drift ratios: 1%, 2%, and at the point of failure.

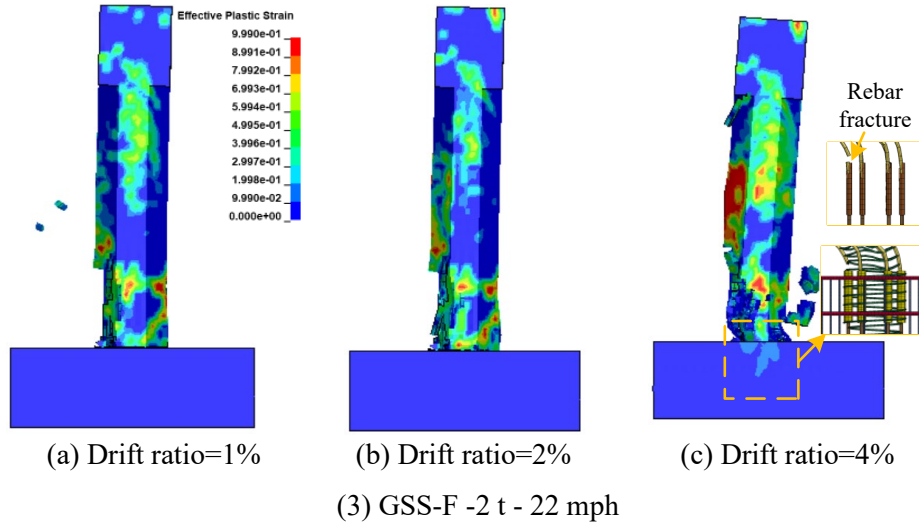
For the CIP columns, a significant amount of concrete spalling was observed at the impact level on the side opposite the impact at a 1% drift ratio. At a 2% drift ratio, the concrete continued to spall upward, and a shear crack developed at the column base. This damage pattern was notably different from that of healthy CIP columns, which typically exhibited concrete failure only at the column base corners in the pushover direction. In the post-impact columns, the shear cracks and concrete spalling persisted, indicating these weakened areas were prone to early failure under cyclic loading. Once the cyclic load was applied, these pre-damaged regions were the first to exhibit failure. At a drift ratio of 3%, the column collapsed, primarily due to the shear crack at the base.

For GSS-C columns, the horizontal crack at the top of the coupler began to widen at a drift ratio of 1%. As the drift ratio increases to 2%, this horizontal crack spread and widened. At the failure ratio of 6%, significant erosion occurred in the grout on the bottom side of the coupler and one extreme rebar close to the opposite impact surface fractures.

For GSS-F columns, most of the concrete below the height of 28 inches spalled on the side opposite the impact. A 45-degree shear crack developed from the impact location to the column base at a drift ratio of 2%. At the failure ratio of 4%, the column collapsed, primarily due to the shear crack at the base. Simultaneously, one extreme rebar close to the opposite impact surface fractured.





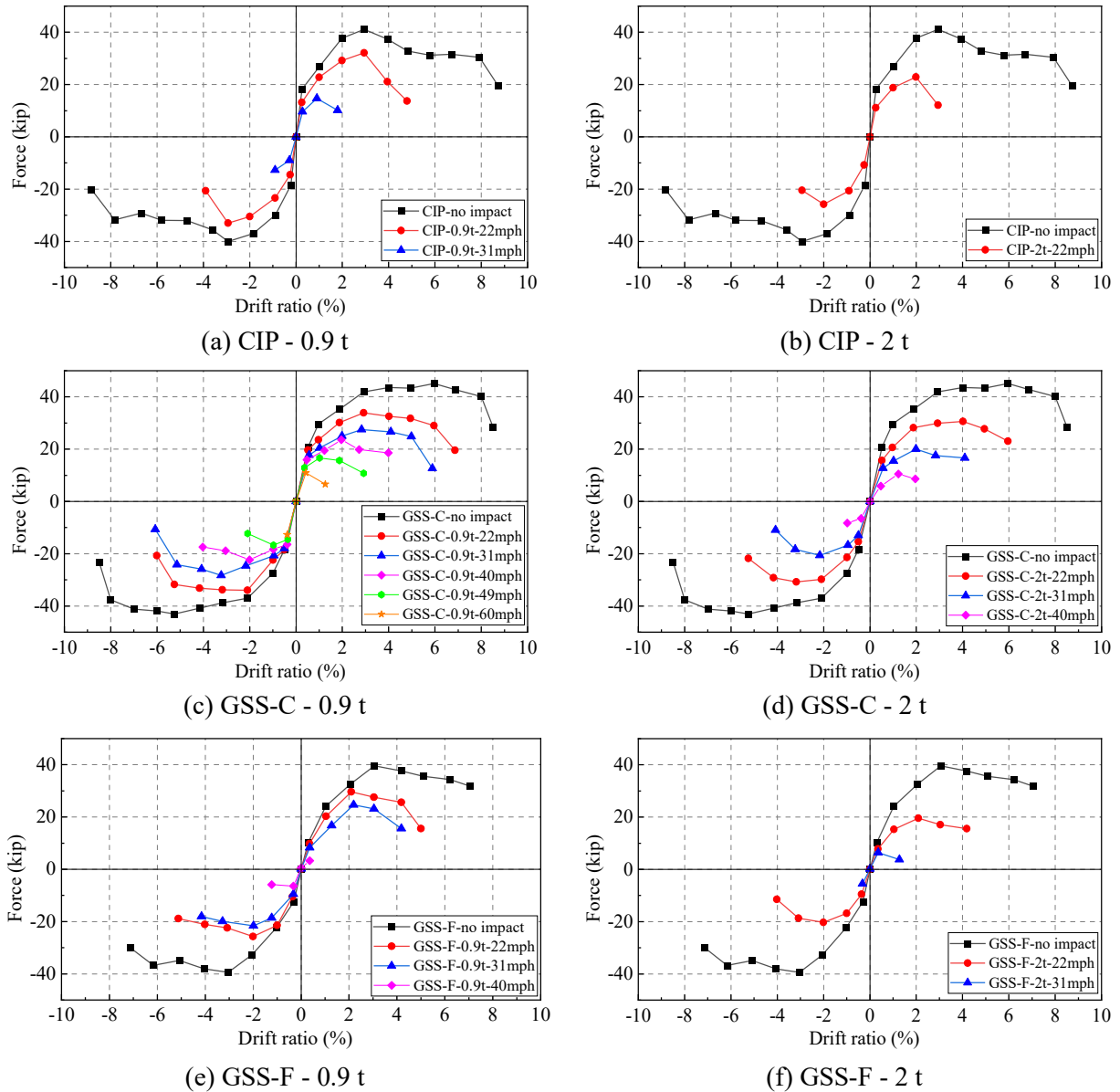


**Figure 5.7** Damage development progressions of columns

To explore the effect of impact on reducing the seismic capacity of columns, skeleton curves were derived from the FE results. Figure 5.8 lists and compares these curves, providing a detailed analysis of how the impact influences the structural performance and residual seismic capacity of the columns.

A comparison between Figure 5.8 (a) and (b) demonstrates that higher impact velocities and heavier impact masses significantly reduced the drift ratio at failure. This reduction in failure drift ratio indicates that columns subjected to more severe impacts have a diminished ability to exhibit ductile performance during seismic events, resulting in lower seismic capacity.

Furthermore, a comparison between Figure 5.8 (a), (c), and (e) reveals the residual seismic capacities of the three types of columns. The findings are based on the analysis of three categories of columns, each impacted by a Toyota Yaris (0.9 tons) at a velocity of 31 mph. The results show that the GSS-C columns failed at a 6% drift ratio, the GSS-F columns failed at a 4% drift ratio, and the CIP columns failed at a 2% drift ratio. This indicates GSS-C columns have the highest residual seismic capacity, followed by GSS-F columns, and then CIP columns. The CIP columns exhibited more extensive concrete spalling and cracking at the end of the impact, which significantly reduced their bearing capacity and seismic resilience. In contrast, the GSS-C columns demonstrated better performance in maintaining structural integrity and seismic capacity after impact, due to the added reinforcement provided by the GSSs at the base. GSS-F columns also performed better than CIP columns but are less effective than GSS-C columns, suggesting the placement of GSSs plays a crucial role in enhancing the column's resistance to both impact and seismic loads.



**Figure 5.8** Skeleton curves

Additionally, the displacement ductility capacity ( $\mu$ ) was calculated and analyzed. The calculation method for displacement ductility capacity was introduced in Section 4.3.2.1. According to the Caltrans Seismic Design Criteria (SDC), the minimum displacement ductility capacity for ductile components is 3.0 [66]. Furthermore, the AASHTO-Seismic provisions specify the local ductility demand for ductile members in high-seismic zones is limited to 5.0 for single-column bents and 6.0 for multiple-column bents [32]. All simulation cases were evaluated to determine if they met these requirements for displacement ductility capacity, shown as Table 5.2.

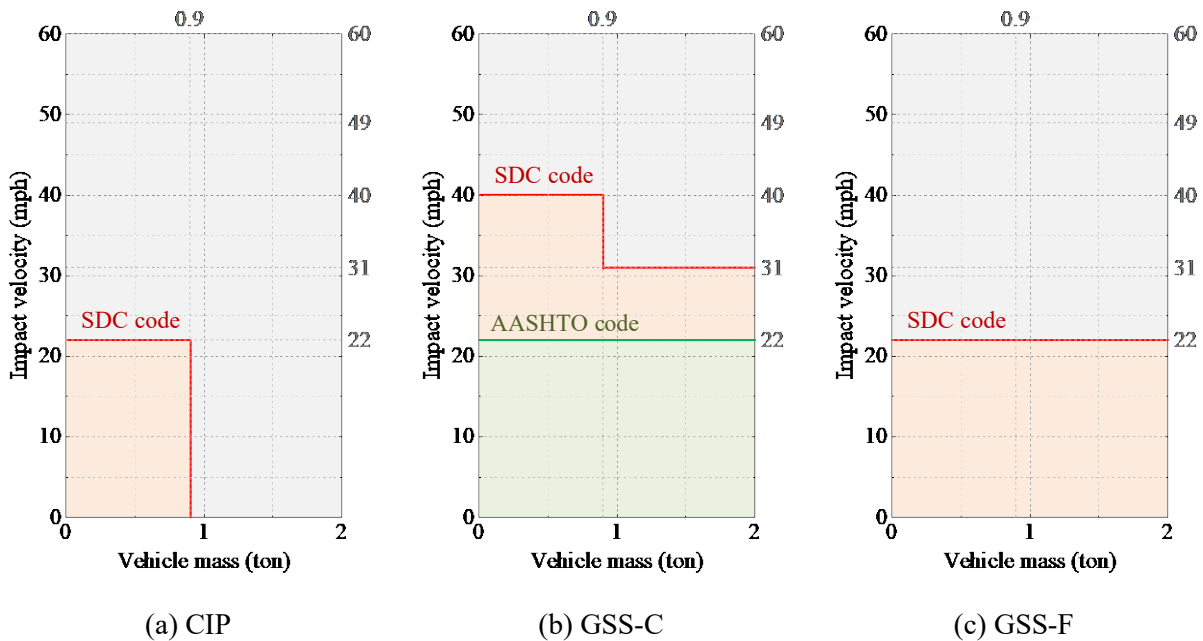
According to the simulated results in Table 5.2, the relatively conservative relationship between impact velocity and vehicle mass with respect to code requirements is illustrated in Figure 5.9. This figure provides a visual representation of how different impact scenarios align with the standards set by various seismic codes. For CIP columns, a vehicle weighing less than 0.9 tons and colliding with a pier at a velocity less than 22 mph poses no threat to the bridge pier in the subsequent earthquake, based on the

SDC. Compared to CIP, the precast columns with GSSs demonstrate greater tolerance for future seismic loads. Specifically, for GSS-C columns, impacts from vehicles with a mass less than 2 tons and velocities less than 22 mph will allow the column to perform well under the AASHTO code requirements. However, a 0.9-ton vehicle colliding at 40 mph and a two-ton vehicle colliding at 31 mph for GSS-C, and a two-ton vehicle colliding at 22 mph for GSS-F are the threshold conditions set by the SDC. Exceeding these impact conditions may compromise structural integrity of the columns and their ability to withstand subsequent seismic events. This figure can help to determine the residual seismic capacity of the columns after an impact accident, guiding the assessment and necessary reinforcement measures to ensure structural integrity and safety in future seismic events.

**Table 5.2** Comparisons of displacement ductility capacity from skeleton curves

Specimens	No impact	Vehicle mass	v=22 mph	v=31mph	v=40mph	v=49mph	v=60mph
CIP	8.2	0.9 ton	3.3	1.7	-	-	-
		2 ton	2.8	-	-	-	-
GSS-C	5.6	0.9 ton	5.4	4.6	3.2	2.5	1.2
		2 ton	5.0	3.1	1.9	-	-
GSS-F	5.5	0.9 ton	3.6	2.7	1.1	-	-
		2 ton	3.1	1.1	-	-	-

Notes: Blank filled with green indicates the structure meets the AASHTO code requirements; blanks filled with orange signifies the structure meets the SDC code requirements; and blanks filled with purple and gray mean the structure, after this impact condition, cannot survive the subsequent seismic event.



**Figure 5.9** Relationship of impact velocity and mass with code requirements

## 5.5 Summary

In this chapter, a calibrated 3D FE model of a half-scale column in LS-DYNA was employed to evaluate the residual seismic capacity following an impact, using sequential impact and quasi-static cyclic loading protocols. After the impact loading, damage distributions and displacement curves were compared among three types of columns. The subsequent cyclic loading phase analyzed damage progression, skeleton curves, and displacement ductility capacity. The chapter concludes with a table illustrating the relationship between impact velocity and vehicle mass with respect to code requirements, aiding in determining the residual seismic capacity of columns after an impact accident.

After the impact loading, the three categories of columns exhibited distinct crack distributions and failure modes. The CIP pier experienced a typical punching shear failure, with a significant crack at a 30-degree angle extending from the impact location to the top of the pier. The GSS-C specimen showed grout bed failure and grout failure at the bottom of the coupler, with a significant horizontal shear crack at the top of the GSSs and a diagonal shear crack at a 10-degree angle extending from the impact location to the top of the pier. The base coupler in the column resulted in fewer shear cracks on both the top and bottom of the column and a smaller area of concrete spalling on the opposite impact surface. This configuration also helped reduce the shear crack angle, delaying the onset of significant cracking, maintaining the column's bearing capacity, and preventing collapse. In the GSS-F specimen, grout bed failure occurred, and a shear crack initiated from the impact location and extended to the bottom corner of the opposite impact side, indicating shear failure. However, there was no evident grout damage in the sleeve connection, though there was slight rebar slip at the top of the coupler under the larger impact. The GSS-F specimen also exhibited fewer shear cracks and less concrete spalling compared to the CIP columns.

By assessing displacement curves at various heights, similar findings were observed under the impacts of both the Toyota Yaris (0.9 tons) and the Dodge Ram (2 tons). For the 0.9-ton impact, CIP columns showed maximum displacement at 18 inches above the base, with no footing-column slip, indicating a strong connection and severe concrete cracks. GSS-C columns had maximum displacement around three inches above the base and significant base slips (4-28 mm). GSS-F columns showed varying responses with velocities; at higher velocities, the maximum displacement moved to the impact point with consistent around 10 mm base slip. Comparing the average displacements around the impact location, precast columns with GSSs at the footing-column joint have smaller average displacements than CIP columns, exhibiting better impact resistance under high-velocity impacts.

In the subsequent cyclic-loading phase, damage patterns in the post-impact columns were notably different from those of the healthy columns. In the post-impact columns, the shear cracks and concrete spalling areas due to the impact damage were prone to early failure under cyclic loading. For GSS-C columns, significant erosion occurred in the grout on the bottom side of the coupler, and one extreme rebar close to the opposite impact surface fractured at the failure drift ratio. Similarly, for GSS-F columns, one extreme rebar close to the opposite impact surface was also found to have fractured.

In comparing skeleton curves of the three categories of columns, it was found GSS-C columns have the highest residual seismic capacity, followed by GSS-F columns, and then CIP columns. The CIP columns exhibited more extensive concrete spalling and cracking at the end of the impact, which significantly reduced their bearing capacity and seismic resilience. In contrast, the GSS-C columns demonstrated better performance in maintaining structural integrity and seismic capacity after impact, due to the added reinforcement provided by the GSSs at the base. GSS-F columns also performed better than CIP columns but were less effective than GSS-C columns, suggesting the placement of GSSs played a crucial role in enhancing the column's resistance to both impact and seismic loads.

By calculating displacement ductility capacity for all study cases, their compliances were evaluated with the requirements set by SDC and AASHTO. The analysis revealed that CIP columns can withstand impacts from vehicles weighing less than 0.9 tons at velocities up to 22 mph. In contrast, GSS-C columns can tolerate impacts from a 0.9-ton vehicle colliding at 40 mph and a two-ton vehicle colliding at 31 mph, demonstrating superior performance. GSS-F columns met the SDC limits under impacts of two tons at 22 mph. However, exceeding these impact conditions may compromise the structural integrity of the columns and their ability to withstand subsequent seismic events. This study provides critical insights and references for assessing the residual seismic capacity of columns after impact accidents, guiding necessary reinforcement measures to ensure structural integrity and safety in future seismic events.

## 6. CONCLUSIONS

The literature reviewed highlights challenges in existing numerical studies, such as computational demands, inaccuracies in bond-slip behavior representation, and the need for a dynamic increase factor (DIF) in simulations. To address these issues and improve both accuracy and efficiency, this research proposed an advanced FE model that incorporates both static and dynamic bond stress-slip laws and solid elements for detailed stress distribution. This approach aims to fill significant gaps in current research and contribute to safer bridge structures.

Two 3D FE models were developed in this study:

- (1) FE models of test specimens with single couplers matching the dimensions of experimental specimens were created to predict strain responses and simulate dynamic behavior in columns with grouted sleeve splices (GSSs). Key parameters, including material properties, mesh size sensitivity, and bond-slip laws, were calibrated to ensure validation. These models were compared with experimental results under static and dynamic conditions.
- (2) FE models of three half-scale columns were established to simulate the experiment by Pantelides et al. [2]. Validation against experimental results was achieved using key characteristics, such as strain-time history curves for load transfer, hysteresis curves, average skeleton curves, and analysis of crack development and damage states at critical drift ratios.

Two main conclusions of this validation study were:

- (1) The FE models of test specimens with single couplers effectively captured deformation behaviors, stress distribution, and bond-slip mechanisms, ensuring efficient load transfer. The models demonstrated accuracy by precisely predicting peak impact events with minimal error margins (0.7% to 1.65%), confirming their capability to simulate dynamic behaviors. They also accurately predicted crack development and failure modes, representing bond-slip interactions between grout and rebar, and revealing non-visible damage within couplers, which is not easily observed in experimental tests. This comprehensive approach validates the FE modeling method for further dynamic studies and contributes to the development of more resilient precast concrete structures.
- (2) The FE models of half-scale columns connected with six couplers showed good agreement with experimental results in both initial and pushover stages, confirming their accuracy and reliability. The models successfully captured the initial elastic behavior and bond-slip law within the coupler, supporting their use for subsequent pushover validation studies. Errors in displacement ductility capacity ranged from 3.7% to 9.8%, and errors in effective yield force ranged from 2.1% to 7.6%, demonstrating the high accuracy of the FE method. The models effectively captured cracking, crushing, and plastic hinge development, validating their use for further studies on seismic performance in precast concrete columns.

After validation, the calibrated 3D FE model of a half-scale column was used to assess residual seismic capacity following an impact through sequential impact and quasi-static cyclic loading protocols. Post-impact, damage distributions and displacement curves were compared across three column types. The subsequent cyclic-loading phase analyzed damage progression, skeleton curves, and displacement ductility capacity. The study concluded with a figure showing the relationship between impact velocity and vehicle mass in relation to code requirements, helping determine the residual seismic capacity of columns after an impact accident.

The main conclusions of this study were:

- (1) After impact loading, the three types of columns displayed distinct crack patterns and failure modes. The CIP pier suffered a punching shear failure with a significant 30-degree crack from the impact location to the pier's top. The GSS-C specimen had grout bed and bottom coupler failures, with a notable horizontal shear crack at the GSS top and a 10-degree diagonal crack, resulting in fewer overall shear cracks and reduced concrete spalling. This configuration delayed significant cracking and maintained the column's bearing capacity. In the GSS-F specimen, grout bed failure and a shear crack extended to the opposite bottom corner, with slight rebar slip at the top coupler, exhibiting fewer shear cracks and less spalling compared to CIP columns.
- (2) Assessing displacement curves revealed similar findings for Toyota Yaris (0.9 tons) and Dodge Ram (2 tons) impacts. CIP columns had maximum displacement at 18 inches with severe concrete cracks. GSS-C columns had maximum displacement around three inches above the base and significant base slips (4-28 mm). GSS-F columns showed varying responses with velocities, with maximum displacement moving to the impact point at higher velocities and consistent around 10 mm base slip. Precast columns with GSSs at the footing-column joint have smaller average displacements than CIP columns, demonstrating better impact resistance under high-velocity impacts.
- (3) During the cyclic loading phase, post-impact columns exhibited distinct damage patterns compared to undamaged columns. Shear cracks and concrete spalling from the impact led to early failure under cyclic loading. In GSS-C columns, significant erosion was noted in the grout at the bottom of the coupler, with a fracture in one extreme rebar opposite the impact surface at the failure drift ratio. Similarly, in GSS-F columns, a fracture was observed in one extreme rebar near the opposite impact surface.
- (4) Comparing the skeleton curves of the three column types, GSS-C columns exhibited the highest residual seismic capacity, followed by GSS-F, and then CIP columns. CIP columns showed extensive spalling and cracking, reducing their bearing capacity and seismic resilience. GSS-C columns maintained structural integrity and seismic capacity better due to added reinforcement at the base. GSS-F columns performed better than CIP but were less effective than GSS-C, highlighting the importance of GSS placement in enhancing impact and seismic load resistance.
- (5) The displacement ductility capacity for all study cases was evaluated with SDC and AASHTO requirements. CIP columns can withstand impacts from vehicles under 0.9 tons at up to 22 mph. In contrast, GSS-C columns can tolerate impacts from a 0.9-ton vehicle at 40 mph and a two-ton vehicle at 31 mph, demonstrating superior performance. GSS-F columns meet SDC limits under impacts of 2 tons at 22 mph. Exceeding these impacts may compromise structural integrity for subsequent seismic events. This study provides critical insights and references for assessing the residual seismic capacity of columns after impact accidents, guiding necessary reinforcement measures to ensure structural integrity and safety in future seismic events.

## REFERENCES

- [1] Florida International University, “ABC Project and Research Databases <http://utcdb.fiu.edu/>,” Aug. 2019.
- [2] C. P. Pantelides, M. J. Ameli, and L. D. Reaveley, “Evaluation of Grouted Splice Sleeve Connections for Precast Reinforced Concrete Bridge Piers (MPC-17-320),” 2017.
- [3] A. Ebrahimpour, B. E. Earles, M. Tangarife, and A. D. Sorensen, “Seismic Performance of Columns with Grouted Couplers in Idaho Accelerated Bridge Construction Applications,” 2016. [Online]. Available: <http://itd.idaho.gov/alt-programs/?target=research-program>
- [4] Z. B. Haber, “Precast Column-Footing Connections for Accelerated Bridge Construction in Seismic Zones,” 2013.
- [5] C. Zhao, Z. Zhang, J. Wang, and B. Wang, “Numerical and theoretical analysis on the mechanical properties of improved CP-GFRP splice sleeve,” *Thin-Walled Structures*, vol. 137, pp. 487–501, Apr. 2019, doi: 10.1016/j.tws.2019.01.018.
- [6] E. W. KJ William, “Constitutive model for the triaxial behavior of concrete,” 1975.
- [7] C. Liu, L. Pan, H. Liu, H. Tong, Y. Yang, and W. Chen, “Experimental and numerical investigation on mechanical properties of grouted-sleeve splices,” *Constr Build Mater*, vol. 260, Nov. 2020, doi: 10.1016/j.conbuildmat.2020.120441.
- [8] E. Henin and G. Morcou, “Non-proprietary bar splice sleeve for precast concrete construction,” *Eng Struct*, vol. 83, pp. 154–162, Jan. 2015, doi: 10.1016/j.engstruct.2014.10.045.
- [9] “Abaqus user’s manual, in: D.S.S. Corp (Ed.) Providence, R.I., USA, 2014.”.
- [10] Z. Kuang and G. Zheng, “Computational and experimental mechanical modelling of a composite grouted splice sleeve connector system,” *Materials*, vol. 11, no. 2, Feb. 2018, doi: 10.3390/ma11020306.
- [11] Y. Zheng, M. Xie, Z. Liu, Y. Zhang, and X. Ding, “Performance of high strength steel bar splice with novel grouted deformed sleeve under tensile load,” *Constr Build Mater*, vol. 403, Nov. 2023, doi: 10.1016/j.conbuildmat.2023.133092.
- [12] E. K. Kahama, X. Fuzhe, and D. L. M. Anglaere, “Numerical study on the influence of defects in grouting on the mechanical properties of a full grouted sleeve connector,” *Journal of Adhesion*, vol. 98, no. 16, pp. 2550–2581, 2022, doi: 10.1080/00218464.2021.1982389.
- [13] J. Murcia-Delso and P. Benson Shing, “Bond-Slip Model for Detailed Finite-Element Analysis of Reinforced Concrete Structures,” *Journal of Structural Engineering*, vol. 141, no. 4, Apr. 2015, doi: 10.1061/(asce)st.1943-541x.0001070.
- [14] Juan, “UC San Diego UC San Diego Electronic Theses and Dissertations Title Bond-Slip Behavior and Development of Bridge Column Longitudinal Reinforcing Bars in Enlarged Pile Shafts.” [Online]. Available: <https://escholarship.org/uc/item/5th92044>
- [15] J. Murcia-Delso, A. Stavridis, and B. Shing, “MODELING THE BOND-SLIP BEHAVIOR OF CONFINED LARGE-DIAMETER REINFORCING BARS.”



- [16] Y. Liu, H. Hao, and Y. Hao, “Prediction of blast response of RC columns considering dynamic bond-slip between reinforcement and concrete,” *Eng Struct*, vol. 283, May 2023, doi: 10.1016/j.engstruct.2023.115921.
- [17] E. Jacques and M. Saatcioglu, “High strain rate bond characteristics of reinforced concrete beam-ends,” *Int J Impact Eng*, vol. 130, pp. 192–202, Aug. 2019, doi: 10.1016/j.ijimpeng.2019.04.012.
- [18] E. Jacques and M. Saatcioglu, “Bond-slip modelling of reinforced concrete lap splices subjected to low and high strain rates,” *Eng Struct*, vol. 195, pp. 568–578, Sep. 2019, doi: 10.1016/j.engstruct.2019.05.104.
- [19] S. B. Kang, S. Wang, X. Long, D. D. Wang, and C. Y. Wang, “Investigation of dynamic bond-slip behaviour of reinforcing bars in concrete,” *Constr Build Mater*, vol. 262, Nov. 2020, doi: 10.1016/j.conbuildmat.2020.120824.
- [20] W. Yao, H. Wu, and F. Huang, “Experimental investigation about dynamic bond-slip between reinforcing steel bar and concrete,” in *Applied Mechanics and Materials*, 2013, pp. 1073–1081. doi: 10.4028/www.scientific.net/AMM.249-250.1073.
- [21] P. Máca, E. Panteki, and M. Curbach, “Bond stress-slip behaviour of concrete and steel under high-loading rates,” *International Journal of Computational Methods and Experimental Measurements*, vol. 4, no. 3, pp. 221–230, 2016, doi: 10.2495/CMEM-V4-N3-221-230.
- [22] Y. Liu, H. Hao, and Y. Hao, “Investigation on the dynamic bond-slip behaviour between steel bar and concrete,” *Eng Fract Mech*, vol. 291, Oct. 2023, doi: 10.1016/j.engfracmech.2023.109540.
- [23] M. Tazarv, T. Sjurseth, E. Greeneway, K. Hart, M. LaVoy, and N. Wehbe, “Experimental Studies on Seismic Performance of Mechanically Spliced Precast Bridge Columns,” *Journal of Bridge Engineering*, vol. 27, no. 11, Nov. 2022, doi: 10.1061/(asce)be.1943-5592.0001948.
- [24] P. K. Dahal and M. Tazarv, “Mechanical bar splices for incorporation in plastic hinge regions of RC members,” *Constr Build Mater*, vol. 258, Oct. 2020, doi: 10.1016/j.conbuildmat.2020.120308.
- [25] M. Tazarv and M. S. Saiidi, “Seismic design of bridge columns incorporating mechanical bar splices in plastic hinge regions,” *Eng Struct*, vol. 124, pp. 507–520, Oct. 2016, doi: 10.1016/j.engstruct.2016.06.041.
- [26] D. H. Qiao, Y. Q. Xu, X. Zhang, J. B. Pang, K. Liu, and S. J. Wang, “Seismic behaviour and size effect of column base joints with inverted exposed grouted sleeves,” *Journal of Building Engineering*, vol. 51, Jul. 2022, doi: 10.1016/j.job.2022.104333.
- [27] M. Ding, W. Xu, J. Wang, Y. Chen, X. Du, and R. Fang, “Seismic performance of prefabricated concrete columns with grouted sleeve connections, and a deformation-capacity estimation method,” *Journal of Building Engineering*, vol. 55, Sep. 2022, doi: 10.1016/j.job.2022.104722.
- [28] M. Wu, X. Liu, H. Liu, and X. Du, “Seismic performance of precast short-leg shear wall using a grouting sleeve connection,” *Eng Struct*, vol. 208, Apr. 2020, doi: 10.1016/j.engstruct.2020.110338.
- [29] J. Xia, J. jing Chen, K. Shan, and Y. fan Wu, “Seismic performance of corroded prefabricated column-footing joint with grouted splice sleeve connection: Experiment and simulation,” *Journal of Building Engineering*, vol. 80, Dec. 2023, doi: 10.1016/j.job.2023.108112.

- [30] Z. Lu, B. Wu, H. Sakata, J. Huang, and M. Zhang, “Mechanical performance of prefabricated concrete beam-column joints with double-grouted sleeve connectors: A numerical and theoretical study,” *Structures*, vol. 56, Oct. 2023, doi: 10.1016/j.istruc.2023.07.060.
- [31] L. Xu, J. Pan, and L. Guo, “Mechanical performance of precast RC columns with grouted sleeve connections,” *Eng Struct*, vol. 252, Feb. 2022, doi: 10.1016/j.engstruct.2021.113654.
- [32] American Association of State Highway and Transportation Officials (AASHTO), *AASHTO Guide Specifications for LRFD Seismic Bridge Design*. Washington D.C.: AASHTO, 2011.
- [33] 7 Author *et al.*, “ANALYSIS OF LARGE TRUCK COLLISIONS WITH BRIDGE PIERS: PHASE 1. REPORT OF GUIDELINES FOR DESIGNING BRIDGE PIERS AND ABUTMENTS FOR VEHICLE COLLISIONS 5. Report Date 6. Performing Organization Code 13. Type of Report and Period Covered Project performed in cooperation with the Texas Department of Transportation and the Federal Highway Administration. Project Title: Guidelines for Designing Bridge Piers and Abutments for Vehicle Collisions Unclassified,” 2009.
- [34] “0630\_02-dot\_Collision loads on bridge piers phase 2, report of guidelines for designing”.
- [35] Q. A. Alomari and A. Dissertation, “STRUCTURAL PERFORMANCE AND RESILIENCY OF REINFORCED CONCRETE BRIDGE PIER COLUMNS, MULTI-COLUMN PIERS, AND BRIDGE SYSTEMS SUBJECTED TO MULTIPLE HAZARDS-FIRE, COLLISION, AND AIR BLAST,” 2023.
- [36] W. Zhao, J. Ye, and J. Qian, “Dynamic behavior and damage mechanisms of reinforced concrete piers subjected to truck impact,” *Eng Fail Anal*, vol. 121, Mar. 2021, doi: 10.1016/j.engfailanal.2020.105158.
- [37] K. Opping, B. Phares, A. Alipour, R. Sturgill, and M.-C. Hsu, “Vulnerability assessment and performance improvement strategies for bridges subjected to vehicular collision.”
- [38] Hrishikesh, “PERFORMANCE-BASED RELIABILITY ANALYSIS AND CODE CALIBRATION FOR RC COLUMN SUBJECT TO VEHICLE COLLISION,” 2012.
- [39] H. Sharma, S. Hurlbaas, and P. Gardoni, “Performance-based response evaluation of reinforced concrete columns subject to vehicle impact,” *Int J Impact Eng*, vol. 43, pp. 52–62, May 2012, doi: 10.1016/j.ijimpeng.2011.11.007.
- [40] H. Li, W. Chen, and H. Hao, “Dynamic response of precast concrete beam with wet connection subjected to impact loads,” *Eng Struct*, vol. 191, pp. 247–263, Jul. 2019, doi: 10.1016/j.engstruct.2019.04.051.
- [41] L. Zhou, X. Li, and Q. Yan, “Performance of Grouting Sleeve-Connected Prefabricated Beams Subjected to Impact Loading,” *Buildings*, vol. 12, no. 12, Dec. 2022, doi: 10.3390/buildings12122146.
- [42] H. Su, W. Fan, H. Wang, B. Liu, W. Sun, and X. Shao, “Direct shear strength of UHPC-based gravity-type grouted sleeve connection members,” *Journal of Building Engineering*, vol. 69, Jun. 2023, doi: 10.1016/j.jobbe.2023.106266.

- [43] W. Sun, C. Yang, W. Fan, H. Wang, and H. Su, “Vehicular impacts on precast concrete bridge piers with grouted sleeve connections,” *Eng Struct*, vol. 267, Sep. 2022, doi: 10.1016/j.engstruct.2022.114600.
- [44] Z. G. Wang, H. Wu, Q. Fang, and J. Wu, “Numerical study on the residual axial capacity of ultra high performance cementitious composite filled steel tube (UHPC-FST) column under contact explosion,” *Thin-Walled Structures*, vol. 153, Aug. 2020, doi: 10.1016/j.tws.2020.106832.
- [45] L. Xu, J. Pan, and L. Guo, “Mechanical performance of precast RC columns with grouted sleeve connections,” *Eng Struct*, vol. 252, Feb. 2022, doi: 10.1016/j.engstruct.2021.113654.
- [46] F. Lin and P. Zhao, “Behavior of grouted sleeve splice for steel profile under tensile loadings,” *Materials*, vol. 13, no. 9, May 2020, doi: 10.3390/MA13092037.
- [47] M. Wu, X. Liu, H. Liu, and X. Du, “Seismic performance of precast short-leg shear wall using a grouting sleeve connection,” *Eng Struct*, vol. 208, Apr. 2020, doi: 10.1016/j.engstruct.2020.110338.
- [48] D. H. Qiao, Y. Q. Xu, X. Zhang, J. B. Pang, K. Liu, and S. J. Wang, “Seismic behaviour and size effect of column base joints with inverted exposed grouted sleeves,” *Journal of Building Engineering*, vol. 51, Jul. 2022, doi: 10.1016/j.job.2022.104333.
- [49] J. Murcia-Delso and P. Benson Shing, “Bond-Slip Model for Detailed Finite-Element Analysis of Reinforced Concrete Structures,” *Journal of Structural Engineering*, vol. 141, no. 4, Apr. 2015, doi: 10.1061/(asce)st.1943-541x.0001070.
- [50] “LS-DYNA ®,” 1992. [Online]. Available: [www.lstc.com](http://www.lstc.com)
- [51] M. Trentacoste, “Users Manual for LS-DYNA Concrete.”
- [52] X. Xu, “Performance Based Approach for Loading and Design of Bridge Piers Impacted by Medium Weight Trucks,” 2017.
- [53] by H. Fahed S Salahat B, “Performance of sub-standard reinforced concrete barriers in protecting bridge piers against vehicular collision force,” AN ABSTRACT OF A DISSERTATION, 2012.
- [54] W. Sun, C. Yang, W. Fan, H. Wang, and H. Su, “Vehicular impacts on precast concrete bridge piers with grouted sleeve connections,” *Eng Struct*, vol. 267, Sep. 2022, doi: 10.1016/j.engstruct.2022.114600.
- [55] Y. V. Novozhilov, A. N. Dmitriev, and D. S. Mikhaluk, “Precise Calibration of the Continuous Surface Cap Model for Concrete Simulation,” *Buildings*, vol. 12, no. 5, May 2022, doi: 10.3390/buildings12050636.
- [56] A. T. Pham, K. H. Tan, and J. Yu, “Numerical investigations on static and dynamic responses of reinforced concrete sub-assemblages under progressive collapse,” *Eng Struct*, vol. 149, pp. 2–20, Oct. 2017, doi: 10.1016/j.engstruct.2016.07.042.
- [57] J. Jiang, C. Xia, J. Yao, Q. Sun, and H. Xia, “Vulnerability analysis of HSR bridge under near-field blast based on response surface method,” *Structures*, vol. 55, pp. 983–994, Sep. 2023, doi: 10.1016/j.istruc.2023.06.053.

- [58] S. Karunarathna, S. Linforth, A. Kashani, X. Liu, and T. Ngo, “Numerical investigation on the behaviour of concrete barriers subjected to vehicle impacts using modified K&C material model,” *Eng Struct*, vol. 308, Jun. 2024, doi: 10.1016/j.engstruct.2024.117943.
- [59] R. W. Li, H. Wu, Q. T. Yang, and D. F. Wang, “Vehicular impact resistance of seismic designed RC bridge piers,” *Eng Struct*, vol. 220, Oct. 2020, doi: 10.1016/j.engstruct.2020.111015.
- [60] W. Zhao, J. Ye, and J. Qian, “Dynamic behavior and damage mechanisms of reinforced concrete piers subjected to truck impact,” *Eng Fail Anal*, vol. 121, Mar. 2021, doi: 10.1016/j.engfailanal.2020.105158.
- [61] W. Fan, X. Xu, Z. Zhang, and X. Shao, “Performance and sensitivity analysis of UHPFRC-strengthened bridge columns subjected to vehicle collisions,” *Eng Struct*, vol. 173, pp. 251–268, Oct. 2018, doi: 10.1016/j.engstruct.2018.06.113.
- [62] L. Chen, L. Fang, W. Fan, T. Liu, and H. Wu, “Field test and numerical simulation of a full-scale RC pier under multiple lateral impacts,” *Eng Struct*, vol. 268, Oct. 2022, doi: 10.1016/j.engstruct.2022.114747.
- [63] ACI Committee 374, “Guide for Testing Reinforced Concrete Structural Elements Under Slowly Applied Simulated Seismic Loads, Farmington Hills, MI: American Concrete Institute,” 2013.
- [64] R. W. Li, D. Y. Zhou, and H. Wu, “Experimental and numerical study on impact resistance of RC bridge piers under lateral impact loading,” *Eng Fail Anal*, vol. 109, Jan. 2020, doi: 10.1016/j.engfailanal.2019.104319.
- [65] W. Zhao and J. Ye, “Dynamic behavior and damage assessment of RC columns subjected to lateral soft impact,” *Eng Struct*, vol. 251, Jan. 2022, doi: 10.1016/j.engstruct.2021.113476.
- [66] California Department of Transportation, “Seismic Design Criteria, CA: Division of Engineering Services,” 2010.